Final Technical Report

Project Title: Production of Hydrogen for Clean and Renewable Source of Energy for Fuel Cell Vehicles

Project Period: May 1, 2005 to January 31, 2008
Reporting Period: May 1, 2005 to January 31, 2008
Date of Report: October 31, 2008

Recipient: University of Toledo
Award Number: DE-FG36-05GO85025

Working Partners: Bowling Green State University
Midwest Optoelectronics, LLC

Cost-Sharing Partners: Bowling Green State University
Ohio Department of Development
Midwest Optoelectronics, LLC

Contact: Dr. Xunming Deng, Principal Investigator
(419) 530-4782; xunming.deng@utoledo.edu
William B. Ingler Jr., Project Coordinator
(419) 530-2651, william.ingler@utoledo.edu

DOE Managers: Roxanne Garland, DOE HQ Technology Manager
Dave Peterson, DOE Field Project Officer

This project is carried out and participated by research groups led by:
Prof. Martin Abraham, Chemical Engineering, UT
Prof. Felix Castellano, Chemistry, BGSU
Prof. Maria Coleman, Chemical Engineering, UT
Prof. Robert Collins, Physics, UT
Prof. Alvin Compaan, Physics, UT
Prof. Xunming Deng, Physics, UT
Prof. Dean Giolando, Chemistry, UT
Prof. A. H. Jayatissa, Mechanical Engineering, UT
Prof. Thomas Stuart, Electrical Engineering, UT
Prof. Mark Vonderembse, Management, UT

Project Objective:

- To expand research directed to the development and analysis of DC voltage regulation system for direct PV-to-electrolyzer power feed. This program develops and evaluates methods of producing hydrogen in an environmentally sound manner to support the use of fuel cells in vehicles and at stationary locations.

- To address DOE program objectives in the general area of renewable hydrogen production. It addresses specifically high-efficiency and low-cost production of hydrogen using photoelectrochemical methods.

Background:

This was a two-year project that had two major components: 1) the demonstration of a PV-electrolysis system that has separate PV system and electrolysis unit and the hydrogen generated is to be used to power a fuel cell based vehicle; 2) the development of technologies for generation of hydrogen through photoelectrochemical process and bio-mass derived resources. Development under this project could lead to the achievement of DOE technical target related to PEC hydrogen production at low cost.

The PEC part of the project is focused on the development of photoelectrochemical hydrogen generation devices and systems using thin-film silicon based solar cells. Two approaches are taken for the development of efficient and durable photoelectrochemical cells; 1) An immersion-type photoelectrochemical cells (Task 3) where the photoelectrode is immersed in electrolyte, and 2) A substrate-type photoelectrochemical cell (Task 2) where the photoelectrode is not in direct contact with electrolyte.

Four tasks are being carried out:

Task 1: Design and analysis of DC voltage regulation system for direct PV-to-electrolyzer power feed
Task 2: Development of advanced materials for substrate-type PEC cells
Task 3: Development of advanced materials for immersion-type PEC cells
Task 4: Hydrogen production through conversion of biomass-derived wastes

Summary

Task 1 of this project was driven towards the development of fuel cell and electrolyzer that could be integrated into a GEM vehicle. Through the additional support of other state and federal grants this project was taken to fruition and a fuel cell was developed and attached to a GEM vehicle. A second GEM vehicle is being set up with a second variation of the fuel cell set-up. This task was changed from its original project description; however, this part of the task was completed as outlined in the statement of project objectives and the project description.

Task 2 of this project is for the development of materials that will be used as anode and cathode materials for a substrate module being developed under a separate grant (DE-FG36-05GO15028) at Midwest Optoelectronics. The material development at UT has produced several nickel-based materials that can successfully be integrated into a substrate-type PEC system. These materials will continue to be developed further on a sub-contract from MWOE during phase 2 of grant DE-FG36-05GO15028. The material development on this project has met and exceeded the initial goals set for in the statement of project objectives.

Task 3 of the project is for the development of materials for an immersion-type PEC system. There were two paths that were outlined in the project description. The development of materials under this task has some limited successes as the physical barriers that are needed to be attained have thus proven the major technology barrier

laid out in the original plan. The main barriers have been in reaching specified performance in conductivity, transmission, chemical and electrochemical stability simultaneously, and it must be done at 250 °C. The additional requirement of low-process temperature made it more challenging to find chemically stable oxides using titanium and iron as the base materials. There have been a few successes in indium iron oxide but the performance needs to be further improved. With polymer nanocomposite (ATO-Flexbond), long-term stability is still being studied. On the basis of numerous discussions with the hydrogen working group, material development will proceed down new paths to look into alternative solutions. The material research done thus far will move over to a sub-contract during Phase 2 of the Midwest Optoelectronic grant DE-FG36-05GO15028.

Task 4 of this project looked at the development of hydrogen production through conversion of bio-mass wastes. As outlined on the statement of project objectives and the project description this project was able to be completed successfully. Efforts were made to develop catalyst materials using less expensive materials. Nanofiltration was added to the system in order to remove sulfur contamination from the biomass source that was contaminating the catalyst. The addition of nanofiltration was able to stabilize the system and hydrogen was able to be produced at a constant rate.

Final Technical Report

Task 1: Design and analysis of DC voltage regulation system for direct PV-to-electrolyzer power feed.

1.1 INTRODUCTION

Most alternative electric energy sources such as solar arrays and wind turbines need some type of control that will force them to always produce the maximum possible power under a wide variety of operating conditions. Obviously, the source must be connected to a load that can absorb the variable power from these sources, and this requirement is readily met for sources that are connected to the AC electric power grid.

Although a grid connection insures that all available power will be absorbed, it also means that all solar and most wind systems will require the use of an inverter to convert DC to AC. However, inverters are relatively complex and expensive in comparison to simple DC-DC converters. This implies that for alternative energy installations where a large DC load is also present, a significant cost advantage can be achieved by avoiding the DC-AC conversion process. The most prevalent example of this is fluorescent lights with electronic ballasts in large buildings, but there also are numerous other types of industrial DC loads as well, such as an electrolyzer for producing hydrogen from water.

These DC installations can take on several different configurations, some of which would still have a connection to the AC grid. However, since they forgo the ability to supply power back to the grid, they are restricted to applications where large amounts of DC power are consumed on site. Batteries also can be used for energy storage, but

this adds a very significant expense and may result in a cost that is actually more than a conventional DC-AC system.

This study describes one variation of how peak power tracking can be achieved for these DC systems. It is intended for systems with a DC single source, and is described specifically for a solar array, although conceivably it also could be used with a small wind turbine. Experimental results are included for a system intended to provide DC power for an electrolyzer from a 6 kW solar array [1].

1.2 PREVIOUS RESEARCH

To obtain the maximum available power from a set of solar panels, the power output must be monitored and a control scheme is used to find the maximum power point (MPP) as shown in **Figure 1.1**. A wide variety of control schemes have been presented [2-13], some of which are open loop and some are closed loop [14].

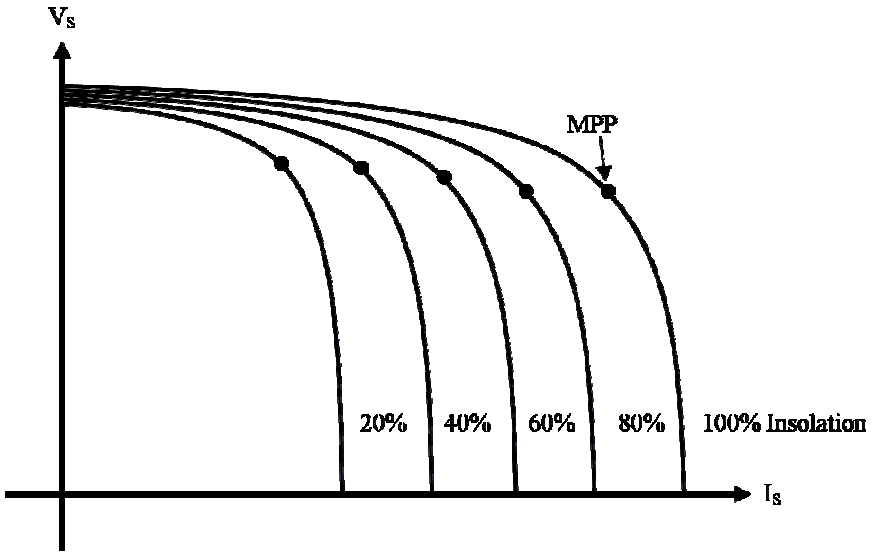

Figure 1.1: Solar array output voltage vs. current curves under varying insolation intensities.

Open loop control uses measurements such as the open circuit voltage of the selected solar panels under varying light intensities and then uses an equation or lookup table to find the MPP. The accuracy of this approach is only as good as the model created, and there are many factors that can affect the performance, such as the temperature and age of the panels.

One form of closed loop control discussed in [5] varies the operating point of the solar panels in small steps, constantly searching for the MPP. After each change the difference in output power, ΔP, is measured. When ΔP is positive the power level has increased, indicating the operating point is moving closer to the MPP. Therefore, the next change in the operating point will be in the same direction. When ΔP is negative, the power level has decreased, indicating the operating point is moving away from the MPP, and the next step in the operating point should be in the opposite direction in order to move back towards the MPP. This method can be referred to as the increment and check method.

Since the variations in the insolation levels cause the current vs. voltage graphs to change, the MPP will vary accordingly. **Figure 1.1** shows the MPPs for a few different insolation levels, indicating that the MPP is not a linear function of the insolation value. The power vs. I_S curve in **Figure 1.2** indicates that the loss in power can be considerable if the MPP is not reached, which indicates the importance of MPP tracking.

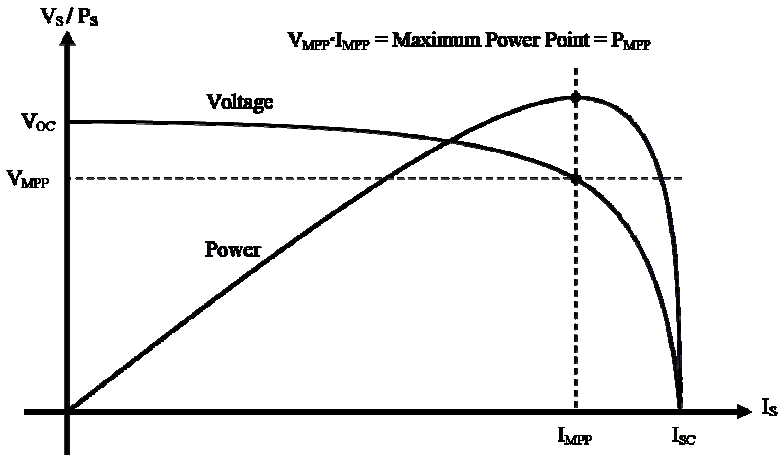

Figure 1.2: MPP and V_S vs. I_S.

The open loop method can typically find the MPP faster since it does not have to step through several operating points, but the closed loop scheme is typically more accurate since it can accommodate changes such as temperature and aging. In a comparison of several types of controls [5] it was found that there was not much difference in their efficiencies, so the choice of control scheme often comes down to ease of implementation.

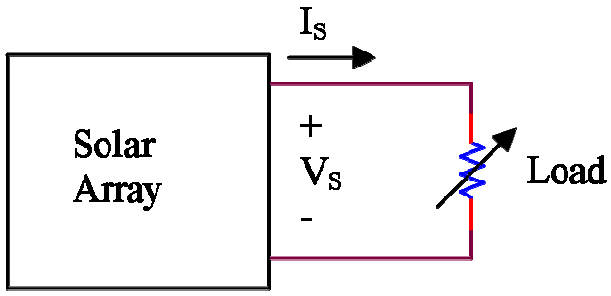

Figure 1.3: Adjustable load.

As shown in **Figure 1.3**, MPPT could be achieved simply by varying the load, but this is not a very practical solution for most applications since most loads cannot be changed dynamically.

A conventional DC-AC MPPT system, shown in **Figure 1.4**, connects the DC output from the solar array to an inverter which produces alternating current. The output of the inverter is then connected to a local load in a stand alone system or to the power grid.

This system is most commonly connected to the power grid, which approximates an ideal voltage source. This means v(t) is not affected by the presence of i(t) or the local load, R_L, i.e., it is what power systems engineers refer to as an infinite bus. Since the inverter's output voltage v(t) will remain constant, the output current can be varied even for a constant local load, and this change in the inverter's output current will cause a variation in the operating point. With this arrangement, AC power can flow to or from the grid, depending on the load and the available solar power.

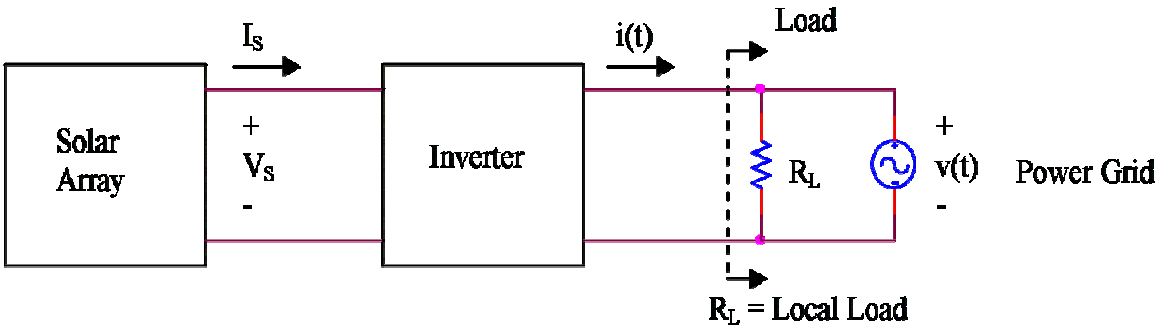

Figure 1.4: Inverter based system.

The vast majority of solar arrays in use, process their energy through an inverter and feed that energy onto the power grid. Due to this popularity a vast majority of the research occurs on inverter based systems [15-22]. There are some down sides to this type of system, however, especially when the desired load requires DC energy.

The main drawback of this system is the complexity and cost of the inverter. While the inverter is typically only 10-15% of the total cost [23], it is still a significant expense. In addition to the cost issue, the inverter also has a relatively low efficiency which can be as low as 85% [23], although most are somewhat higher and can reach as high as 97% [22]. When used for a DC load, a rectifier/regulator is also required, which adds even more cost, and further reduces the efficiency.

If the desired load requires DC energy the system of choice most often uses DC-DC converters. These systems can consist of a single source tied to a single converter; however, due to the inconsistent nature of solar power the power grid is often used as an additional source. The systems in [24-26] essentially use two different DC-DC converters, one for the solar array and another for the power grid. By varying the switching frequency of the respective converters MPPT of the solar array can be achieved. The system proposed here also uses the grid as a source but unlike in [24-26] there is essentially only one converter which controls the amount of power from the grid. This allows a single switching device to control the MPP of the solar array, resulting in a lower cost and higher efficiency.

1.3 BASIC MPP TRACKING FOR A DC LOAD

Figure 1.5 shows a simple system using a solar array and the AC grid to power a DC load.

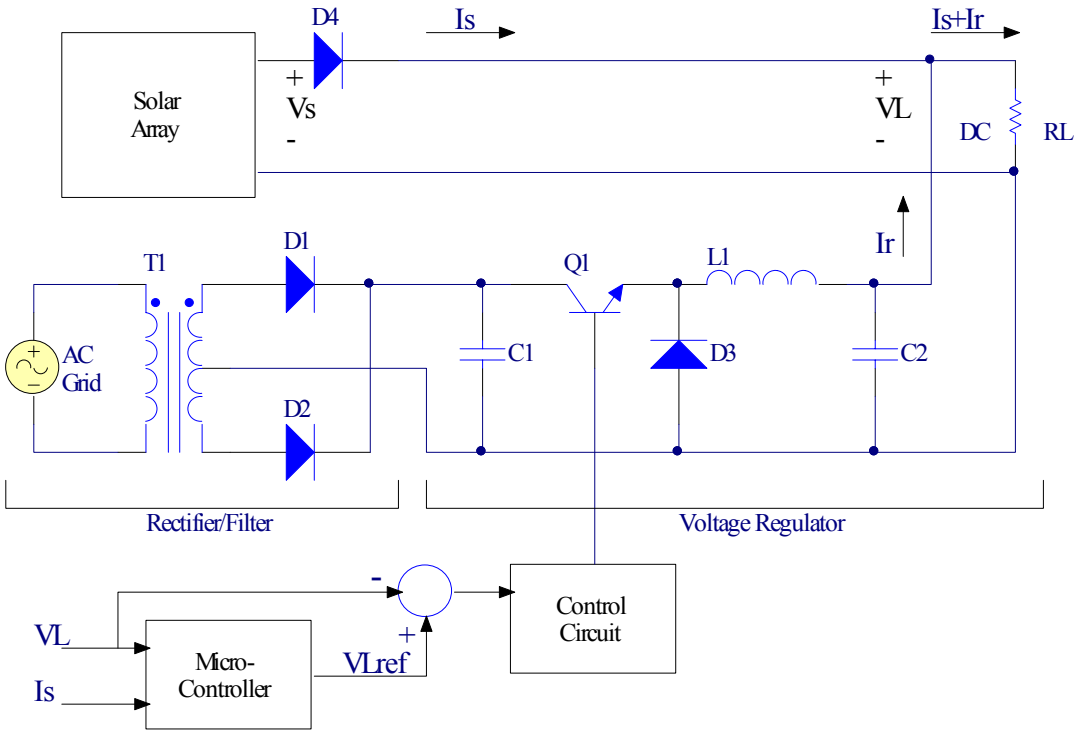

Figure 1.5: Proposed MPPT system.

As seen from the V_S vs. I_S curves in **Figure 1.1**, a solar array has a fairly high output resistance, and therefore in comparison, the output of the voltage regulator in **Figure 1.5** can be regarded as an ideal voltage source. Since the voltage drop across D_4 is very small, $V_S \approx V_L$.

As long as $\frac{V_L^2}{R_L} > V_L I_S$, then, $I_R = \frac{V_L}{R_L} - I_S > 0$ and $V_S \approx V_L$ will be determined by V_{REF} which is set by the microcontroller. The micro measures V_S and I_S, and in a manner similar to [2] adjusts V_{LREF} in $\pm\Delta V$ increments to maximize $V_S I_S = P_{SMAX}$.

The 60Hz transformer, T_1, provides voltage scaling and allows grounding of the negative rail for the load. The regulator in **Figure 1.4** is a simple buck circuit using PWM to adjust $V_L=V_{LREF}$. Size and weight are usually of secondary importance in this type of application so the switching frequency can be chosen to minimize losses and cost. Although a BJT is shown for Q_1, lower voltage applications would probably use a MOSFET while an IGBT would be chosen for higher voltages.

As the solar insolation level varies, V_S also will vary somewhat to track the MPP, e.g. ±10%. However, V_S variations of this size are acceptable for many loads, such as fluorescent lights. The optimum V_S will decrease at lower levels of insolation, so the micro will need to limit V_{SMIN}. Once V_{SMIN} is reached, the solar panels will continue to supply power (although below the peak value) until the open circuit value of V_S in **Figure 1.1** drops below V_{SMIN}. At this point D_4 in **Figure 1.5** will be reverse biased, and all of the power will come from the grid.

If the load decreases to a value below P_{SMAX}, the regulator will shut off since V_L will exceed V_{LREF}. If the load continues to decrease, V_L will continue to rise and will reach the open circuit V_S in **Figure 1.1** if the load draws no current. If left uncorrected, this could produce a value for V_L that could be excessive since the open circuit voltage can exceed the normal V_L by at least +38% for some solar panels [21].

If this high voltage at a small load cannot be tolerated, a simple solution would be to replace the circuit in **Figure 1.5** with the one in **Figure 1.6**. Relay X1 in **Figure 1.6** remains in the NC position until $V_L>V_{LMAX}$, at which time it is switched to the NO position. At this point, V_S will exceed the rectified grid voltage, and D_1 and D_2 will be biased off. The microcontroller will now select V_{LMAX} as the reference for the voltage

regulator which will limit $V_L=V_{LMAX}$. If the load I_S increases enough so the V_S drops and the regulator cannot hold $V_L=V_{LMAX}$, X_1 will return to the NC position, and the regulator will become active and hold $V_SI_S=P_{SMAX}$ as long as $\frac{V_L^2}{R_L} > P_{SMAX}$.

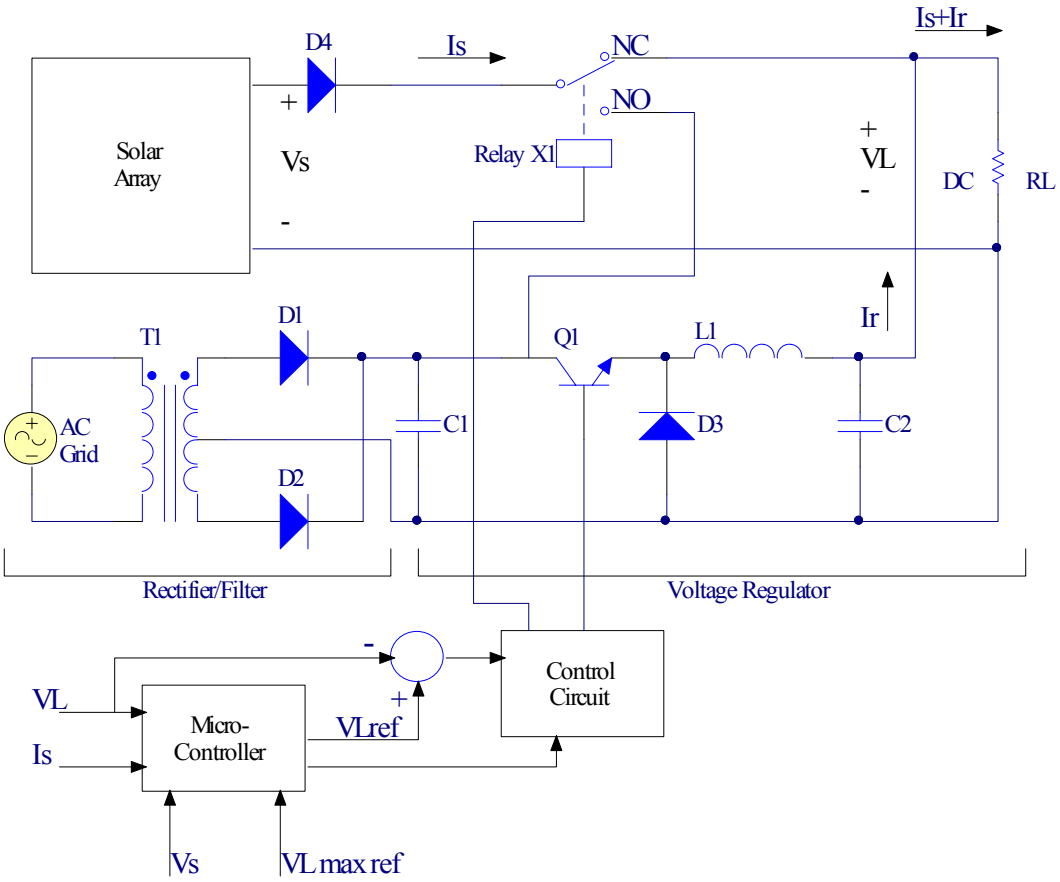

Figure 1.6: Proposed V_{MAX} limit circuit for low power load.

To summarize, this system can provide:

1. MPP tracking for normal loads over the vast majority of the insolation range.

2. At lower insolation levels where only a small amount of solar energy is available, the array will operate at a sub-optimum level until the V_S open circuit voltage drops below V_{MIN}. Below this point all power is supplied by the grid.

3. For very small loads where $P_{SMAX} > \frac{V_L^2}{R_L}$, V_S will rise above the optimum level; the regulator in **Figure 1.5** will cut-off; and the entire load is supplied by the solar array. If necessary, the circuit in **Figure 1.5** can be replaced with **Figure 1.6** to prevent $V_L > V_{LMAX}$.

1.4 IMPLEMENTATION

Certain aspects of the implementation were derived from an earlier project based on a 1kW solar array and described in [1, 27]. A photograph of this array is shown for reference in **Fig. 1.7**.

Figure 1.7: 1kW roof mounted solar array.

A 6kW system was constructed to process the power from one of the two 6kW solar arrays in **Figure 1.8**. This 6kW array consists of 108 model FS-57 solar panels from First Solar. These panels are also constructed from CdTe thin film and have a rated power value of 57.5 watts each [21], giving the array a rated maximum power output of 6210 W. At full sun and no load, this array can reach an open circuit voltage of about 90 Vdc. All of the solar panels are connected in parallel to provide in a rated maximum power point of about 62 V at 100 A which is intended to power an electrolyzer for producing hydrogen.

Figure 1.8: Two 6kW pole mounted solar arrays.

As indicated earlier, this PPT system is intended for loads that slightly exceed the maximum power capability of the solar array so PPT can be achieved over a wide range of insolation levels. The original intent was to use an electrolyzer with a rating slightly above the 6210 W rating of the array, but budget restrictions would only allow the purchase of a 2 kW electrolyzer from Avalence, LLC. The Avalence unit also operates at 30 Vdc instead of 62 Vdc, so a DC-DC converter from Zahn Electronics had to be connected between the array output and the electrolyzer input.

Therefore the 2 kW electrolyzer will not fully load the 6210 W array when the PPT point is above 2 kW, but PPT will still occur when the available solar power is less than 2 kW.

A block diagram of the system is shown in **Figure 1.9**. The long term goal for this system is to implement the rectifier/regulator using a relatively simple buck regulator circuit similar to those shown in **Figures 1.5 and 1.6**. However, the initial proof of concept phase used a commercial 10 kW DC power supply with an output voltage that could be programmed externally. The rectifier/regulator in this system is provided by a DC power supply from Lambda Americas, model ESS-80-125 [28]. This supply is capable of providing up to 80 V and 125 A, and can be externally controlled by a voltage signal.

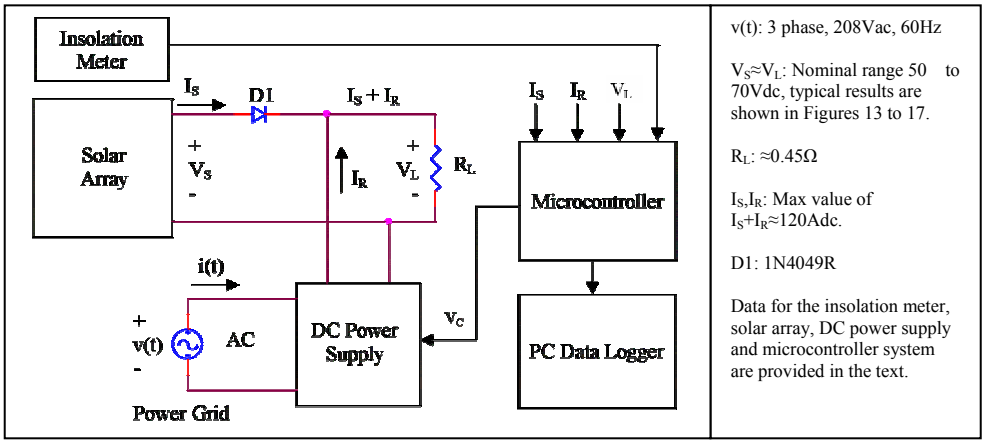

Figure 1.9: Block diagram for the 6 kW solar system with MPPT.

The control system in **Figure 1.9** uses the measured values of the solar current, I_S, and load voltage, V_L, to provide MPPT as described previously. At each time interval the microcontroller determines the next $\pm\Delta V_L$ ($\Delta V_L \approx 0.3V$) increment for the DC power

supply, which is controlled by V_C in **Figure 1.9**. The insolation measurement (i.e., available sunlight power) and the current of the DC power supply, I_R, are used only for data logging proposes.

An Infineon C505CA 8bit microcontroller was chosen to implement the control system. The C505CA has a clock frequency of 10 MHz, a 10-bit analog to digital converter (ADC), and a timer which can be used to provide a digital to analog converter (DAC). Both the ADC and the DAC have a 0-5 V range. For control and data logging purposes, this system requires one output and four inputs.

The first of these inputs is the load voltage, V_L, which has a range of 0-80 V but will typically operate over a range of about 50-70 V. In order for the ADC to measure this voltage, it must be processed by the voltage divider and optical isolator shown in **Figure 1.10**.

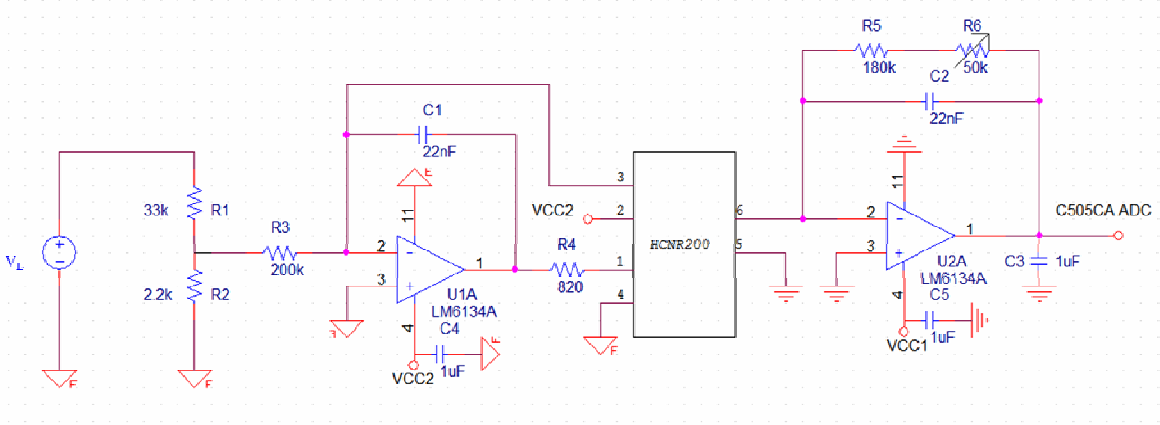

Figure 1.10: Voltage measurement circuit.

The R_1-R_2 voltage divider in **Figure 1.10** attenuates the 0-80 V V_L voltage to 0-5 V. The LM6134 op-amp in U1A is configured to attenuate the input signal to match the

level needed by the HCNR200 optical isolator. U2A is configured to restore the signal to 0-5 V to match the range of the C505CA ADC.

The next two inputs are the currents I_S and I_R, which are measured using two LEM model LA 100-S Hall Effect current transducers connected to identical circuits similar to that in **Figure 1.11**.

I_R is not required for the control system but is of interest for comparison with I_S. The transducer has a measurement range of ±150 A, and a current ratio of 1000:1. This results in a secondary output current, I_{SEC}, with a range of ±150 mA. For this application the current will always be positive, therefore I_{SEC} can be converted into a voltage signal in the range of the ADC using the circuit in **Figure 1.11**.

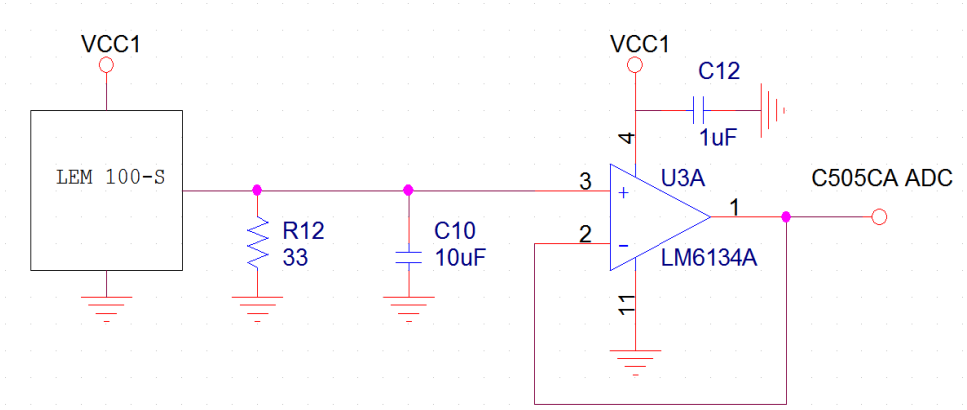

Figure 1.11: Current measurement circuit for I_S and I_R.

The DAC output from the microcontroller connected to pin 5 of U2B in **Figure 1.12** is used to control the voltage of the power supply. The signal generated by the DAC is actually a 6.5 kHz PWM waveform which is filtered to remove the AC harmonics and leave only the DC component. U2B is used to buffer the PWM output of the microcontroller.

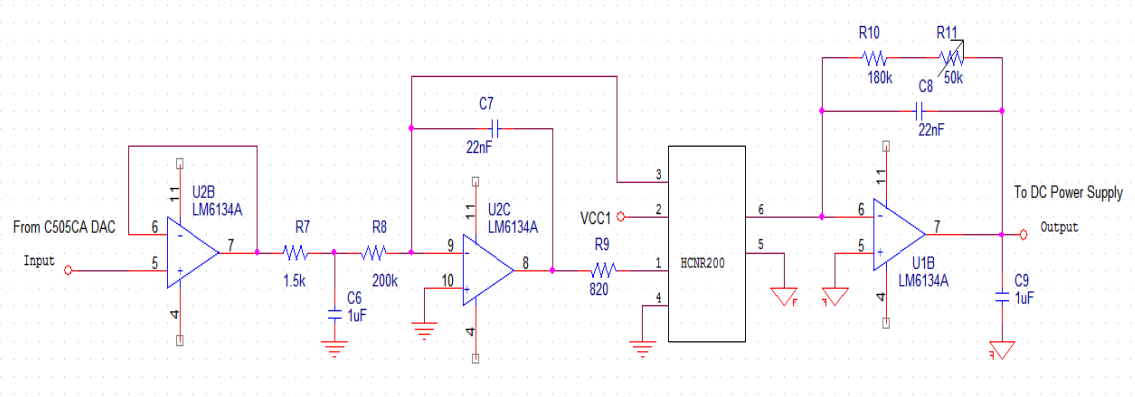

Figure 1.12: Power supply voltage control circuit.

The final input is from an insolation meter which is used to determine the efficiency of the solar panels. The insolation meter is a LI-COR model number LI-190SA Quantum Sensor and is connected to a Universal Transconductance Amplifier from EME Systems to produce a 0-5 V output. This sensor's output is measured in $\mu mol \cdot m^{-2} \cdot s^{-1}$, which needs to be converted to $W \cdot m^{-2}$. This conversion, which is derived below, is accomplished by dividing the $\mu mol \cdot m^{-2} \cdot s^{-1}$ value by 4.6 $\mu mol \cdot J^{-1}$.

$$E = \frac{h \cdot c}{\lambda} = 3.612 \cdot 10^{-19} J \cdot mol^{-1} \tag{1.1}$$

$$\frac{1}{E \cdot \mu mol} \approx 4.6 \mu mol \cdot J^{-1} \tag{1.2}$$

Where $h = 6.626 \times 10^{-34}, c = 2.998 \times 10^{8}, \lambda = Midpoint 550nm, \mu mol = 6.022 \times 10^{17}.$

Since the insolation meter does not have exactly the same wavelength response range as the solar panels, a correction factor is used to account for the unmeasured wavelengths. Using the amount of solar power at different wavelengths given by the ASTM G173 Standard, a correction factor can be determined. The amount of power in the sensor response range (400-700 nm) is about 431 W/m^2, while the solar panel response range (350-850 nm) is about 657 W/m^2. The full spectrum range for sunlight (280-4000 nm) is about 1000 W/m^2. The correction factor, CF_1, used to relate the sensor's range (400-700 nm) to the panel's range (350-850 nm) is given by **Equation 1.4**. CF_2, the correction factor to relate the panel's range (350-850 nm) to the full sun range (280-4000 nm) is given in **Equation 1.5**.

$$CF = \frac{Power\_of\_the\_desired\_range}{Power\_of\_the\_measured\_range} \tag{1.3}$$

$$CF_1 = \frac{657W/m^2}{431W/m^2} \approx 1.52 \tag{1.4}$$

$$CF_2 = \frac{1000W/m^2}{657W/m^2} \approx 1.52 \tag{1.5}$$

Even with these correction factors, some slight errors remain due to variations in which wavelengths actually reach the solar panels. For example, variations caused by morning and evening angle of incidence and cloud cover will not affect all wavelengths of light equally.

The panels have a rated maximum power of 57.5 W based on the ASTM G173 Standard. The effective surface area of each panel is 0.72 m^2. Therefore the rated efficiency, Eff_1, of the panel at the rated maximum power compared to the full spectrum (280-4000 nm) of light can be calculated using **Equation 1.6**.

$$Eff_1 = \frac{Power}{Insolation \cdot Area} = 7.98\% \tag{1.6}$$

To test the system with the 6 kW array, R_L was adjusted to 0.45 Ω to provide a load of almost 8 kW. This was somewhat larger than necessary, but this level was chosen to ensure that the solar array could always reach its maximum power level, which may exceed 6 kW at full sun. These tests were conducted during very good sunlight conditions in March 2006. At this location in northern Ohio, the solar output power will be considerably less at other times of the year, especially during the winter months.

To test the effectiveness of the control system, the DC supply voltage was first varied manually to determine the MPP. Next the control system was activated and allowed to search for the MPP. **Figure 1.13** shows a set of test results for both manual and automatic controls that were conducted in March 2007 about 10 months after the system was installed.

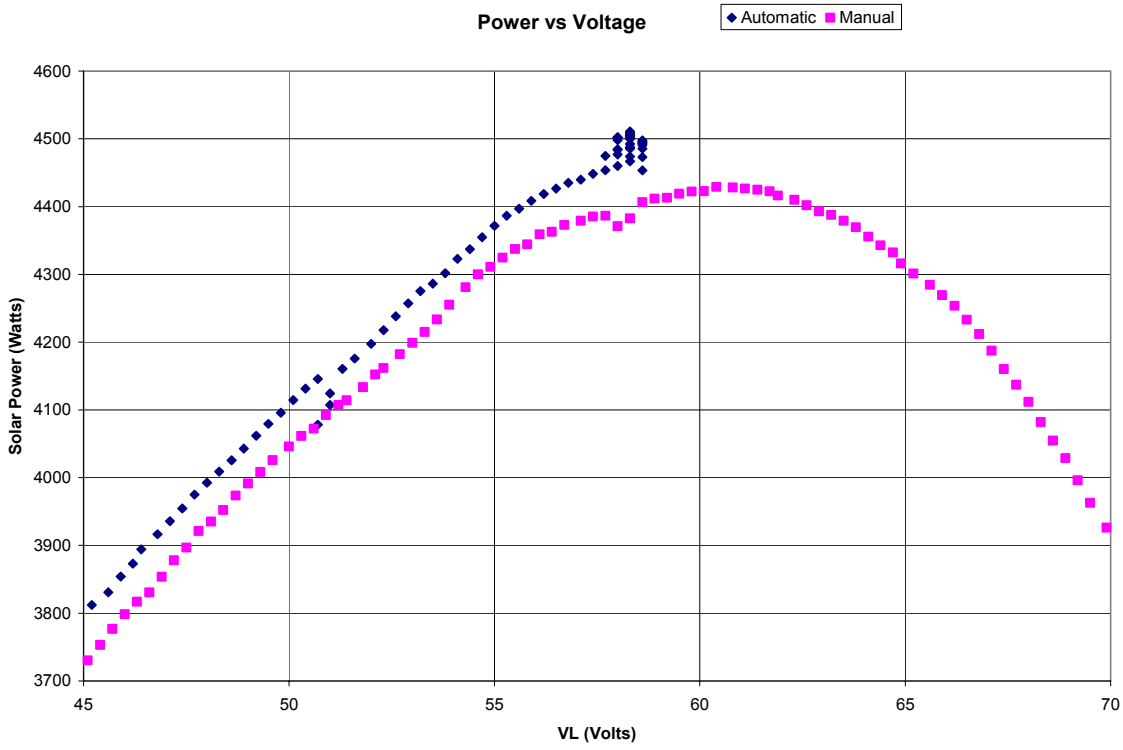

Figure 1.13: Operating point for the solar system in Figure 1.9 for March 2007.

Figures 1.14 to 1.17 show similar results for a series of tests at various insolation levels that were conducted in December 2007 after the system had been in operation for about 19 months. All of these figures show that the automatic control system steps up to, and then oscillates very close to the MPP found by manual control. There is a slight difference between the automatic and manual control graphs, since the two tests could not be performed at exactly the same time, and the insolation usually changed slightly between the two tests.

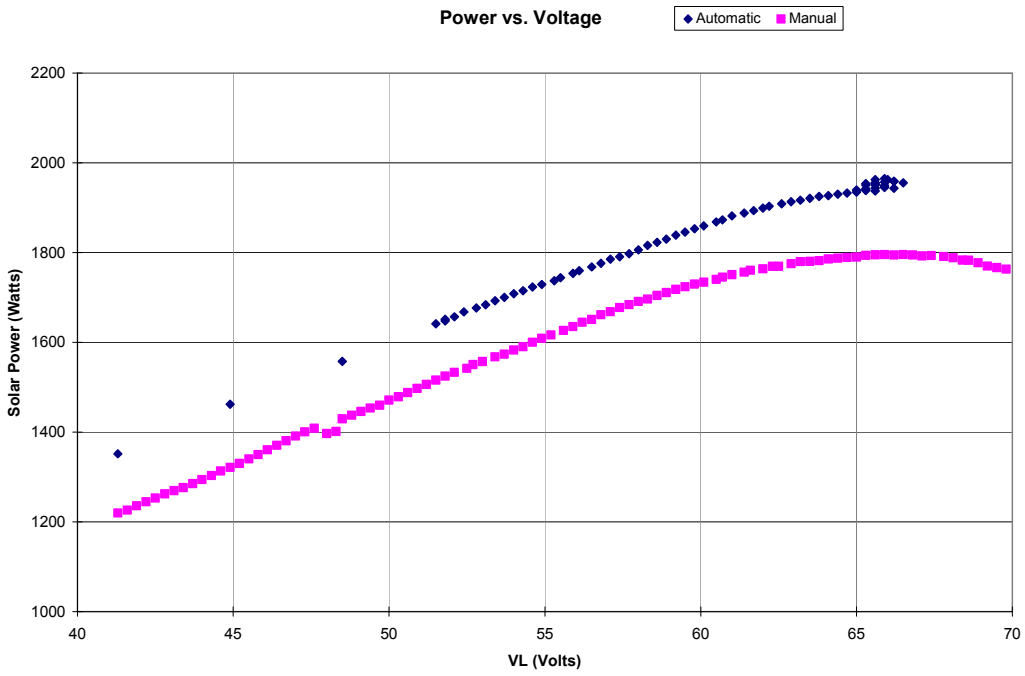

Figure 1.14: Operation for an MPP of about 1950 W, December 2007.

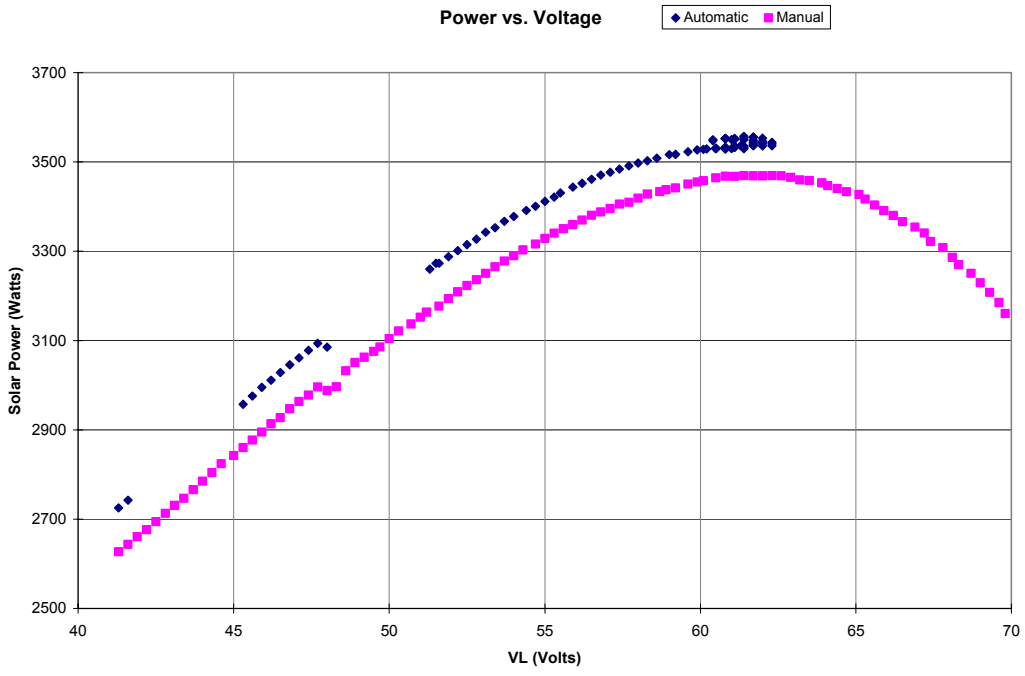

Figure 1.15: Operation for an MPP of about 3550 W, December 2007.

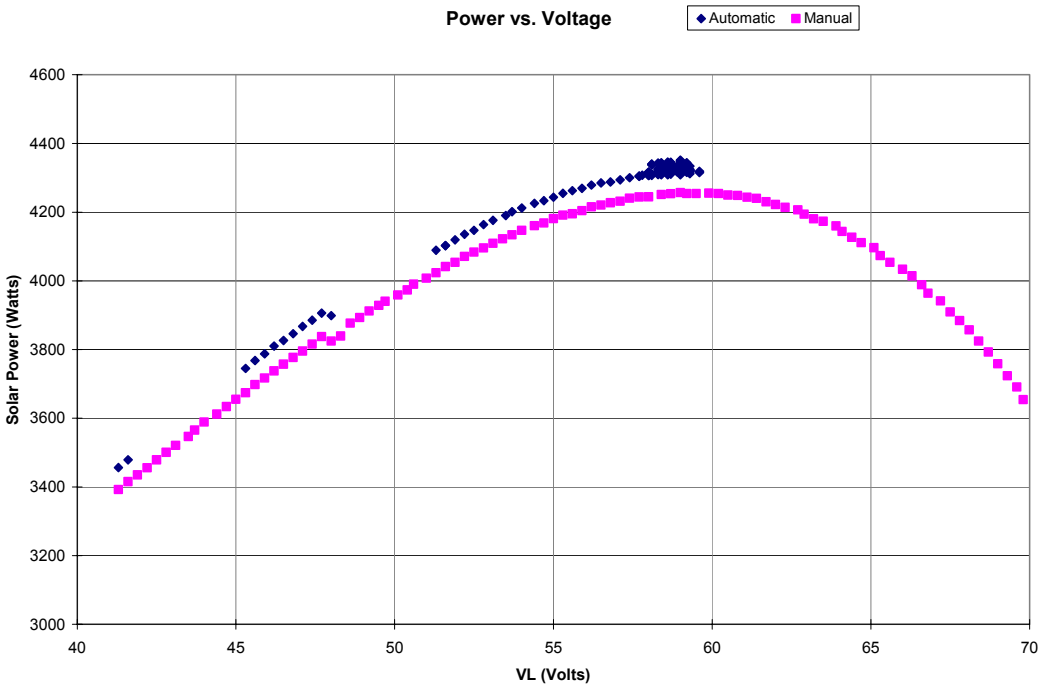

Figure 1.16: Operation for an MPP of about 4350 W, December 2007.

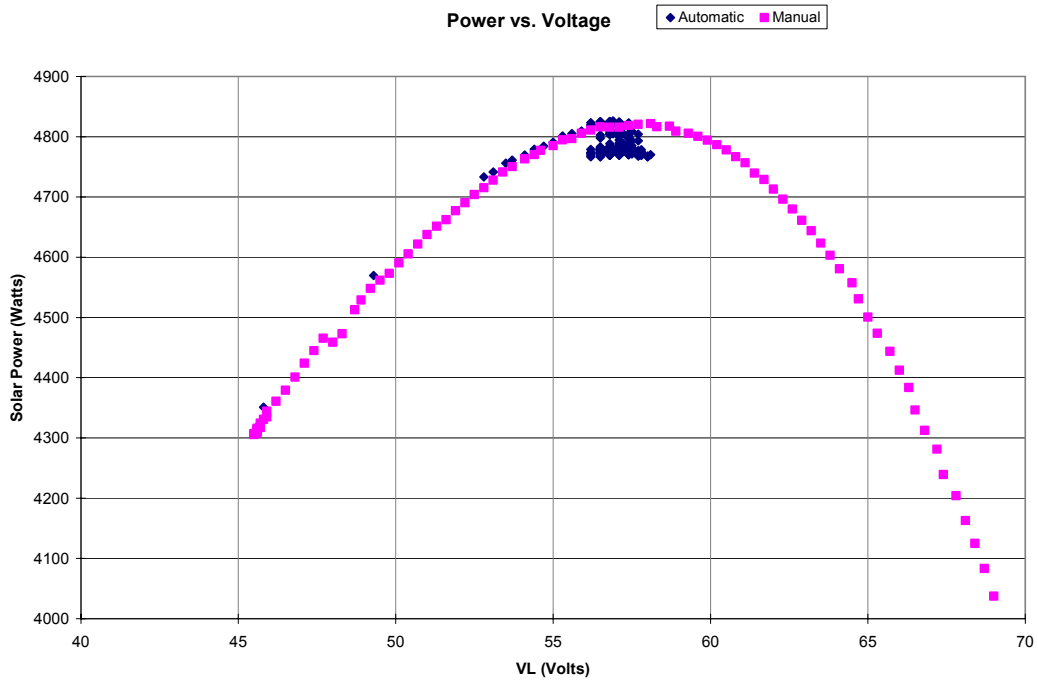

Figure 1.17: Operation for an MPP of about 4800 W, December 2007.

For the next test, the efficiency of the array was measured to determine if it was consistent with the ratings for the panels. On a clear sunny day around solar noon in March 2007, operational data was collected and used to compare the measured efficiency to the calculated efficiency. **Equation 1.7** was used to find the measured efficiency, Eff_2, of the solar panels with respect to the full spectrum (280-4000 nm) of light.

$$Eff_2 = \frac{Power}{Insolation \cdot CF_1 \cdot CF_2} = 8.53\% \tag{1.7}$$

The measured efficiency was close to the calculated efficiency of 7.98% based on the panel ratings, and the slight differences depend on several factors. First, the power of a solar panel is often underrated to ensure the panel will meet its rated value. Second, the rated value was taken at a specific temperature and angle of incidence that may not match the system conditions. Third, there will be a small error in the measurements in both the insolation level and power value.

The efficiency of processing the power from the solar panels is very high since the only loss in that part of the system is that caused by the blocking diode D_1 in **Figure 1.9**. This efficiency, Eff_{SOLAR}, was calculated using **Equation 1.8**, and the results for a range of power levels are shown in **Table 1**.

$$Eff_{SOLAR} = \frac{P_{OUTPUT}}{P_{INPUT}} = \frac{P_{OUTPUT}}{P_{OUTPUT} + I \cdot V_{DIODE}} \tag{1.8}$$

Table 1: Solar power processing efficiency at various power levels for March 2007.

POWER OUTPUT	EFFICIENCY
1000 W	98.4%
2000 W	98.7%
3000 W	98.8%
4000 W	98.7%
5000 W	98.7%
6000 W	98.5%

The total system efficiency also depends on the efficiency of the rectifier/regulator. The commercial DC power supply used to perform this function only has a rated efficiency of only 85-91 % [28], which is relatively low compared to a custom designed buck regulator which should be able to achieve at least 95% [27].

This 6 kW system was placed in operation in May 2006 and has been running continuously for about 20 months. The system has been functioning with a temporary resistive test load (while awaiting delivery of the electrolyzer) except for a few days when grid power outages occurred. The solar array will still provide power to the load during an outage, but V_S will drop below the value corresponding to the MPP whenever grid power is not available. Practical loads would have to be reduced or disconnected during these outages if these low values of V_S were unacceptable.

1.5 CONCLUSIONS

It has been shown that solar installations in close proximity to a large DC load can reduce costs and losses by using a DC/DC conversion system instead of the usual

DC/AC. To achieve MPPT, this load should be greater than the peak available solar power, and the difference is supplied by the AC grid. This also makes it easy to implement MPPT over a wide range of solar insolation levels.

Interest in this concept is likely to increase as the use of solar arrays and solar shingles becomes more widespread. This design scheme has been implemented in two installations on the University of Toledo campus: a 1 kW proof of concept system and a 6 kW system to supply a 2 kW electrolyzer.

1.6 REFERENCES

[1] J. Moening, “A Maximum Power Point Tracking System for Alternative Energy Sources with Direct Current Loads,” M.S. thesis, Dept. Elec. Eng., The University of Toledo, Toledo, Ohio, 2006.stems," *Trans. on Industrial Electronics*, vol. 53, no. 6, pp. 1889-1897, Dec. 2006.

[2] M. Jantsch, M. Real, H. Haberlin, C. Whitaker, K. Kurokawa, G. Blasser, P. Kremer, and C.W.G. Verhoeve, “Measurement of PV Maximum Power Point Tracking Performance,” *14th European Photovoltaic Solar Energy Conference and Exhibition*, 1997.

[3] E. Koutroulis, K. Kalaitzakis, and N. Voulgaris, “Development of a Microcontroller-Based Photovoltaic Power Point Tracking Control System,” *IEEE Transactions on Power Electronics*, Volume 16(1), 2001, pp. 44-56.

[4] W. Wu, N. Pongratananukul, W. Qui, K. Rustom, T. Kasparis, and I. Batarseh, “DSP-based Multiple Peak Power Tracking for Expandable Power Systems,” *Applied Power Electronics Conference and Exposition*, 2003, Vol. 1, pp. 525-530.

[5] D.P. Hohm, and M.E. Ropp, “Comparative Study of Maximum Power Point Tracking Algorithms,” *Progress in Photovoltaics*, 2003, Volume 11, pp. 47-62.

[6] A. Goetzberger, and V.U. Hoffmann, *Photoelectric Solar Energy Generation*. Springer-Verlag Berlin Heidelberg, 2005.

[7] J.A. Jiang, T.L. Huang, Y.T. Hsiao, and C.H. Chen, “Maximum Power Tracking for Photovoltaic Power Systems,” *Tamkang Journal of Science and Engineering*, 2005, Volume 8(2), pp. 147-153.

[8] N. Mutoh, M. Ohno, T. Inoue, "A Method for MPPT Control While Searching for Parameters Corresponding to Weather Conditions for PV Generation Systems," *Trans. on Industrial Electronics*, vol. 53, no. 4, pp. 1055-1065, June 2006.

[9] W. Xiao, M.G.J. Lind, W.G. Dunford, A. Capel, "Real-Time Identification of Optimal Operating Points in Photovoltaic Power Systems," *Trans. on Industrial Electronics*, vol. 53, no. 4, pp. 1017- 1026, June 2006.

[10] J.-M. Kwon, K.-H. Nam, B.-H. Kwon, "Photovoltaic Power Conditioning System With Line Connection," *Trans. on Industrial Electronics*, vol. 53, no. 4, pp. 1048-1054, June 2006.

[11] Weidong Xiao, William G. Dunford, Patrick R. Palmer, Antoine Capel, "Regulation of Photovoltaic Voltage," *Trans. on Industrial Electronics*, vol. 54, no. 3, pp. 1365-1374, June 2007.

[12] Weidong Xiao, Nathan Ozog, William G. Dunford, "Topology Study of Photovoltaic Interface for Maximum Power Point Tracking," *Trans. on Industrial Electronics*, vol. 54, no. 3, pp. 1696-1704, June 2007.

[13] K.K. Tse, B.M.T. Ho, H.S.-H. Chung, S.Y.R. Hui, "A comparative study of maximum-power-point trackers for photovoltaic panels using switching-frequency modulation scheme," Trans. on Industrial Electronics, vol. 51, no. 2, pp. 410- 418, April 2004.

[14] M.R. Patel, *Wind and Solar Power Systems Design, Analysis, and Operation*, Talyor & Francis Group, 2006.

[15] M.H. Rashid, *Power Electronics Handbook,* Academic Press, 2001.

[16] I.-S. Kim, M.-B. Kim, M.-J. Youn, "New Maximum Power Point Tracker Using Sliding-Mode Observer for Estimation of Solar Array Current in the Grid-Connected Photovoltaic System," *Trans. on Industrial Electronics*, vol. 53, no. 4, pp. 1027-1035, June 2006.

[17] J.-H. Park, J.-Y. Ahn, B.-H. Cho, G.-J. Yu, "Dual-Module-Based Maximum Power Point Tracking Control of Photovoltaic Systems," *Trans. On Industrial Electronics*, vol. 53, no. 4, pp. 1036- 1047, June 2006.

[18] J.M. Carrasco, L.G. Franquelo, J.T. Bialasiewicz, E. Galvan, R.C. PortilloGuisado, M.A.M. Prats, J.I. Leon, N. Moreno-Alfonso, "Power-Electronic Systems for the Grid Integration of Renewable Energy Sources: A Survey," *Trans. on Industrial Electronics*, vol. 53, no. 4, pp. 1002- 1016, June 2006

[19] E. Roman, R. Alonso, P. Ibanez, S. Elorduizapatarietxe, D. Goitia, "Intelligent PV Module for Grid-Connected PV Systems," *Trans. On Industrial Electronics*, vol. 53, no. 4, pp. 1066- 1073, June 2006

[20] H. Koizumi, T. Mizuno, T. Kaito, Y. Noda, N. Goshima, M. Kawasaki, K.Nagasaka, K. Kurokawa, "A Novel Microcontroller for Grid-Connected Photovoltaic Sy r of the solar-cell power supply system," *Trans. on Industrial Electronics*, vol. 53, no. 2, pp. 495- 499, April 2006.

[21] M. Rico-Secades, E.L. Corominas, J. Garcia, J. Ribas, A. J. Calleja, J.M. Alonso, and J. Cardesin, “Low Cost Electronic Ballast for a 36-W Fluorescent Lamp Based on Current-Mode-Controlled Boost Inverter for a 120-V DC Bus Power Distribution,” *Trans. on Power Electronics*, vol. 21, no. 4, pp. 1099-1106, July 2006.

[22] FS Series Solar Module Product Datasheet, Available: http://www.firstsolar.com, March 2006,

[23] Y.C. Kuo, T.J. Liang, and J.F. Chen, “A High-Efficiency Single-Phase Three-Wire Photovoltaic Energy Conversion System,” *Trans. on Industrial Electronics*, vol. 50, no. 1, pp. 116-122, February 2003.

[24] B.M.T. Ho, and H.S.H. Chung, “An Integrated Inverter with Maximum Power Tracking for Grid-Connected PV Systems.” *Trans. On Power Electronics*, vol. 20, no. 4, pp. 953-962, July 2005.

[25] R. Gonzalez, J. Lopez, P. Sanchis, and L. Marroyo, “Transformerless Inverter for Single-Phase Photovoltaic Systems,” *Trans. on Power Electronics*, vol. 22, no. 2, pp. 693-697, March 2007.

[26] H. Matsuo, W. Lin, F. Kurokawa, T. Shigemizu, and N. Watanabe, "Characteristics of Multiple-Input DC-DC Converter," *Trans. on Industrial Electronics*, vol. 51, no. 3, pp. 625-631, June 2004.

[27] V. Madineni, "A Solar Powered DC Distribution System," M.S. thesis, Dept. Elec. Eng., The University of Toledo, Toledo, Ohio, 2004.

[28] K. Kobayashi, H. Matsuo, Y. Sekine, "An excellent operating point tracke

[29] March 2006, ESS Series Product Datasheet, Available: http://www.lambda-emi.com

Task 2: Development of advanced materials for substrate-type PEC cells.

Performance analysis of optimized electrocatalytic porous nickel cathodes fabricated by pulsed DC electroplating technique

1. Introduction:

Previous work on the development of electrocatalytic porous electrodes was based on co-deposition of nickel and zinc by using direct current power supply at this laboratory. Although these electrodes showed very good current densities, the adherence of porous structures to the substrate was not very good. Therefore, a pulsed DC power supply (Pinnacle Plus from Advanced Energy) capable of producing pulsed DC power from 5 kHz to 350 kHz was procured and experiments were conducted to improve the adherence of deposited porous nickel coating.

The main principle behind producing porous nickel coating is based on co-deposition of nickel and zinc by electroplating and then leaching out zinc to leave a porous structure of electrocatalytic nickel to increase the surface area. Increased catalytic area reduces the over-potential and thereby improving the efficiency of photoelectrochemical cell for hydrogen production. The over-potential is an inherent potential barrier between the electrode and electrolyte and it is very important to keep this value at a minimum. In advanced hydrogen generation systems, the cathodic over-potential varies from 70 to 150 mV, while anodic over-potential varies from 200 to 250 mV.

In the proposed substrate type photoelectrochemical solar hydrogen generator, the rear side of the triple junction amorphous silicon solar cells is negative and thus the reduction reaction, i.e. hydrogen evolution occurs at the rear side of the electrochemical

cell. As the triple junction solar cell generates 2.2 to 2.3 volts, open circuit voltage, the operating voltage lies in the range 1.75 to 1.90 volts. In order to achieve this figure, it is very essential to have the over-potential kept at a minimum to minimize the potential losses at the electrode interface.

Keeping all these requirements in view, the developmental work was commenced to produce low over-potential catalysts to achieve the goal of producing efficient generation of photoelectrochemical hydrogen.

The substrate chosen in these experiments were 201 annealed nickel foil of 5 mil thickness obtained from All Foils Inc, Ohio. The porous nickel coating involves three steps, as described in the following four phases:

Phase 1: Electroplating of pure nickel on the substrate.

Phase II: Co-deposition of nickel and zinc on the substrate.

Phase III: Enhanced co-deposition of zinc.

Phase IV: Leaching of zinc and producing porous nickel structure.

In this laboratory, we have used the 28.6 cm × 5.0 cm nickel sheets as electrodes. Electroplating was conducted by placing a nickel cathode at the center and two nickel anodes on both sides, so that a uniform deposition of nickel and zinc on cathode substrates is obtained. The distance between the anode and cathode was 1 cm as shown in **Figs. 1a and 1b**.

2. Experimental Method

The electrodes were made by electrodeposition of nickel on the nickel sheets. After running three phases and leaching the electrode in 30 % KOH solution, porous nickel electrodes were obtained. The electroplating process involves following three experimental steps.

Phase I: Electroplating of nickel on to the substrate.

During this phase of electroplating pure nickel is plated on to the substrate. For this operation, roughened, ammonium hydroxide treated nickel sheets have been chosen as the substrate. The plating bath solution was prepared by addition of 330 g of nickel sulfate, 45 g of nickel chloride, and 37 g of boric acid in one liter of deionized water. This solution was kept at 50°C till all the salts are dissolved to produce a homogenous solution.

In this phase, the electrodes are placed in the electroplating tank and a constant current density of 50 mA/cm^2 was passed for 40 min using a pulsed DC power supply at 2.415 V. The frequency of the power supply was varied from 5 to 200 KHz for different sets of experiments to get an optimum operating frequency. During the electroplating operation, the bath temperature was maintained at 50°C.

Phase II: Co - Deposition of zinc and nickel.

During this phase, zinc and nickel are co-deposited on the plated nickel obtained after phase I. The co-deposition of pulsed DC electroplating was carried out for 40 min. This process involved the addition of anhydrous zinc chloride 5 times at intervals of 8 min. This regular addition results in co-deposition of zinc in addition to nickel.

Table 1: Amount of $ZnCl_2$ added at different intervals during Phase II.

Sr. No.	Plating Current (amperes)	Plating Voltage (volts)	Current Density (mA/cm^2)	Time of addition of $ZnCl_2$ addition (minutes)	Amount of $ZnCl_2$ addition (grams)	Total $ZnCl_2$ in bath (grams)
1	5.80	2.203	40	0	9.34	9.34
2	5.80	2.203	40	8	12.48	21.82
3	5.80	2.203	40	16	12.48	34.30
4	5.80	2.203	40	24	12.48	46.78
5	5.80	2.203	40	32	12.48	59.26

Phase III: Enhanced co-deposition of zinc.

The enhanced co-deposition of zinc and nickel is achieved by replacing the electrolytic bath by the $ZnCl_2$ bath solution, which is prepared by adding 24 g of anhydrous $ZnCl_2$ powder in 600 mL of distilled water at 50°C. The electroplating was carried out at 50 mA/cm^2 at 2.415 V. The samples were prepared at 5, 10, 15, 20, 30, 35, 50, 100 and 200 kHz.

Phase IV: **Leaching of zinc.**

During this phase the zinc is leached out in 30 % potassium hydroxide solution for 12 hr or at 50°C for 2 hr. After complete leaching of zinc, the electrodes were cleaned in deionized water and photographed under microscope to observe the porous structure formation. The electrochemical studies on these porous electrodes were performed to check the performance.

2.1: Equipments used:

The following instruments were used in these experiments:

- Pulsed DC power supply unit - DC Pinnacle Plus from Advanced Energy. Model No. 3152433-102 T.
- Voltalab model PG Z301 674R057 N005 from Dynamic-EIS Voltametry.
- Optical Microscope model BHT 229407 BHT series from Olympus System Inc.
- Heater – model Cimarec HP131535 from Barnstead Thermodyne.
- Precision Digital Multimeter model 38XR from Meterman.

3: Optimization of frequencies of applied pulsed DC power.

The porous electrocatalytic nickel electrodes were prepared at different frequencies from 5 KHz to 200 KHz. The performance of the samples with respect to current densities is shown in the following tables. The following tables show data for different size electrodes for hydrogen generation in an alkaline electrolyzer. The distance between anode and cathode is kept at 2 cm and current densities are measured during hydrogen evolution at standard electrolyte concentration of 30 % potassium hydroxide. **Table 2** shows the current densities measured for samples prepared at different frequencies at 1.9 V operating voltage for electrolytic hydrogen generation.

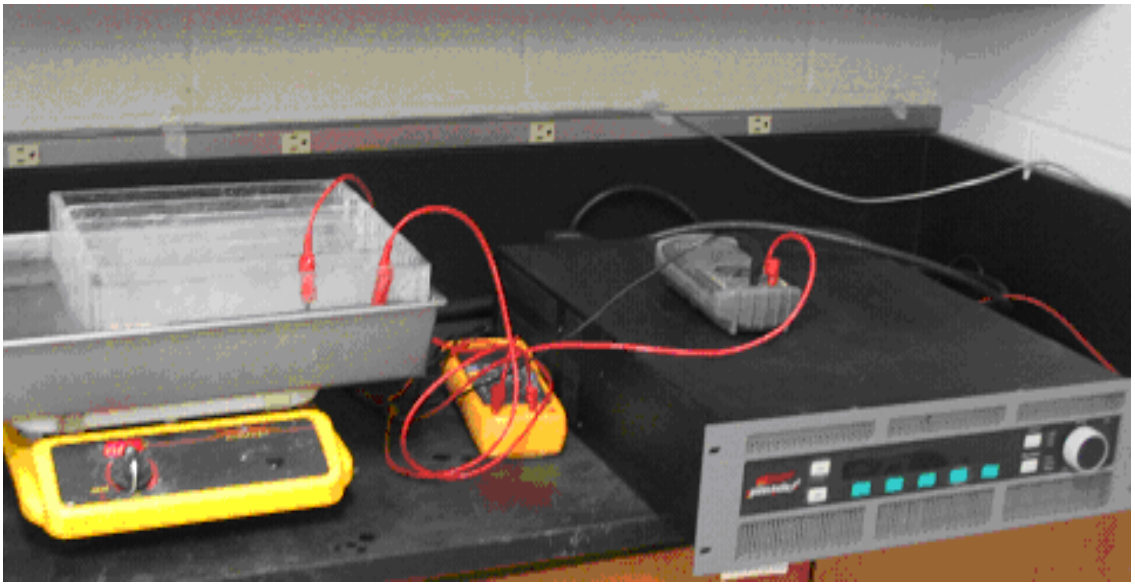

Fig 1a: Shows power supply, heater, plating bath and precision digital multimeters for measuring current density.

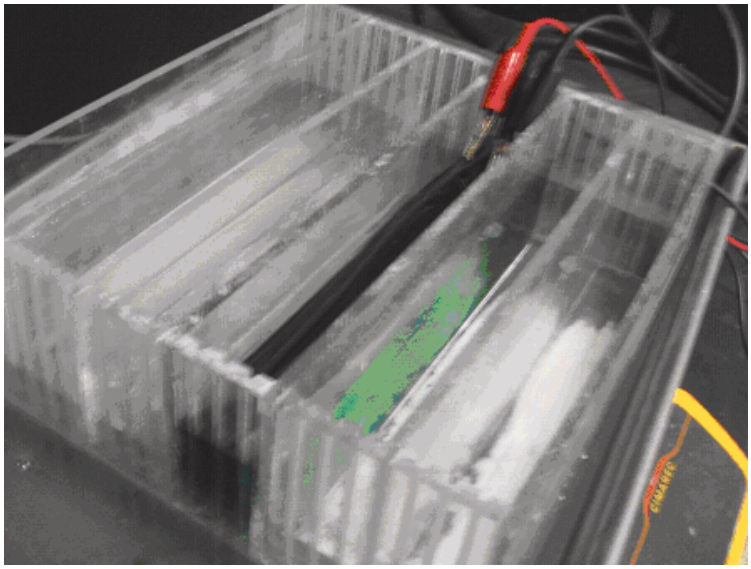

Fig 1b: The electroplating bath in which electro-catalytic porous electrodes were prepared by passing pulsed DC current.

The performance of porous nickel cathodes at different frequencies was evaluated after carrying a series of experiment at different supply voltages varying from 1.8, 1.9, and 2.0 V. With the help of these experiment and the study of the physical

characteristics of the electrode the optimization of conditions were evaluated for the process of electroplating.

Experiment 1: Testing of electroplated samples with platinum foil.

Specifications: Cathode: 1 × 1.5 inch electroplated nickel sheet.

Anode: 1 × 1.5 inch platinum foil.

Table 2: The current densities at different frequencies with respect to platinum foil.

Sr. No	**Frequency** (kHz)	**Current @ 1.8 V** (amp)	**Current density @ 1.8 V** (mA/cm^2)	**Current @1.9 V** (amp)	**Current density @ 1.9 V** (mA/cm^2)	**Current @ 2.0 V** (amp)	**Current density @ 2.0 V** (mA/cm^2)
1	10	0.238	24.61	0.182	18.82	0.090	9.307
2	10	0.253	26.16	0.157	16.23	0.081	8.370
3	20	0.256	26.47	0.168	17.37	0.094	9.720
4	20	0.294	30.40	0.190	19.64	0.103	10.65
5	50	0.235	24.31	0.168	17.37	0.120	12.41
6	100	0.223	23.06	0.181	18.71	0.082	8.47

The plot indicates optimum values of frequency around 20 KHz of the power supply.

Experiment 2: Testing of electroplated samples with sintered electrode.

Specifications: Cathode: 1 × 1.5 inch electroplated nickel foil

Anode: 1 × 1.5 inch sintered (80% Mo: 10% Al: 10% cobalt oxide)

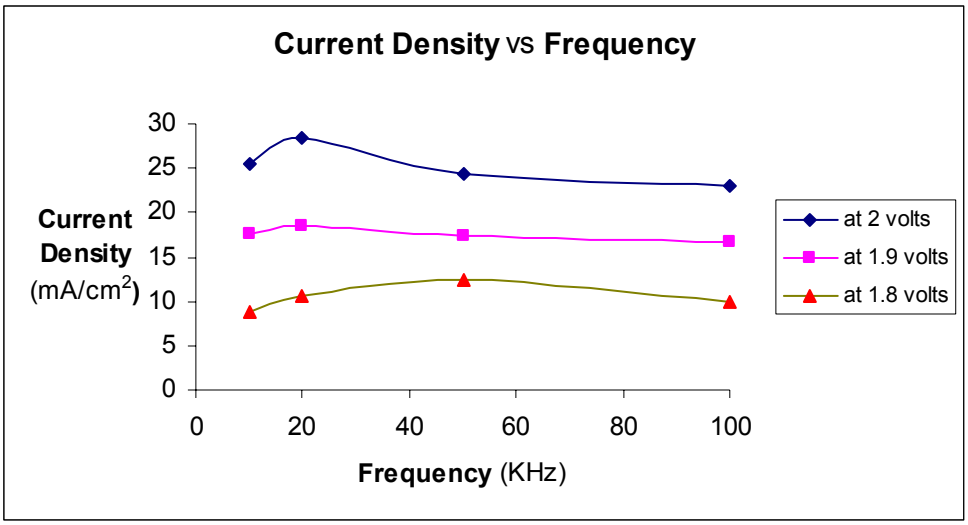

Fig 2: Power plot of average current density vs. frequency after plotting with platinum foil anode.

Table 3: The current densities at different frequencies with respect to sintered electrode.

Sr. No	**Frequency** (kHz)	**Current @ 1.8 V** (amp)	**Current density @ 1.8 V** (mA/cm^2)	**Current @1.9** V (amp)	**Current density @ 1.9 V** (mA/cm^2)	**Current @ 2.0 V** (amp)	**Current density @ 2.0 V** (mA/cm^2)
1	10	0.489	50.56	0.374	38.67	0.258	26.68
3	20	0.502	51.91	0.395	40.84	0.282	29.16
4	20	0.535	55.35	0.397	41.05	0.294	30.40
5	50	0.512	52.94	0.382	39.50	0.258	26.68
6	100	0.491	50.77	0.352	36.40	0.244	25.53

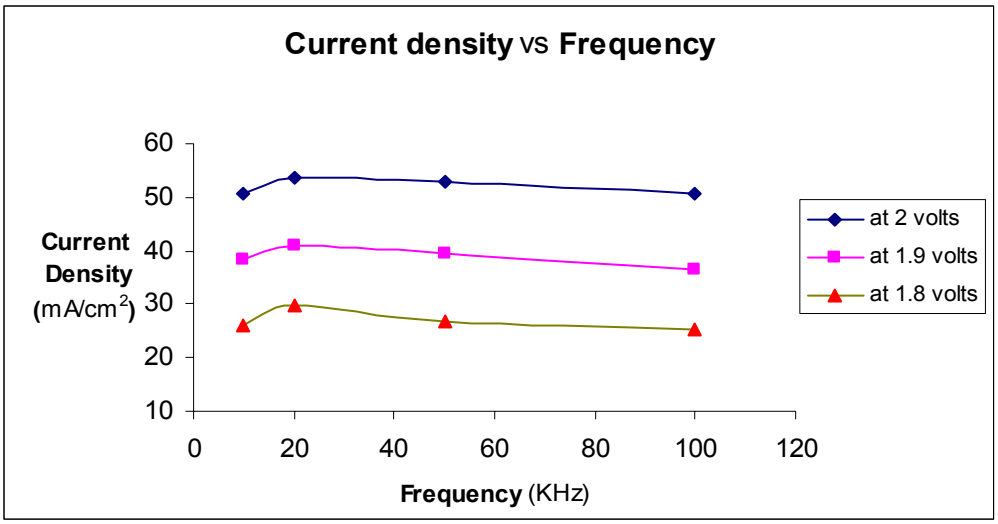

Fig 3: Power plot of average current density vs. frequency after plotting with sintered electrode as an anode.

These experiments also indicate the optimum frequency of pulsed electroplating around 20 KHz.

Experiment 3: Testing of electroplated samples with plain nickel sheet.

Specifications: Cathode: 2 × 2 inch electroplated nickel foil

Anode: 2 × 2 inch plain nickel sheet

Table 4: The current densities at different frequencies with respect to plain nickel sheet

Sr. No	**Frequency** (kHz)	**Current @ 1.8 V** (amp)	**Current density @ 1.8 V** (mA/cm^2)	**Current @1.9 V** (amp)	**Current density @ 1.9 V** (mA/cm^2)	**Current @ 2.0 V** (amp)	**Current density @ 2.0 V** (mA/cm^2)
1	10	0.22	8.52	0.13	5.03	0.07	2.70
3	20	0.36	13.95	0.24	9.30	0.14	5.42
4	50	0.23	8.91	0.13	5.03	0.06	2.32
5	100	0.32	12.4	0.23	8.91	0.14	5.42
6	200	0.26	10.07	0.18	6.97	0.10	3.87

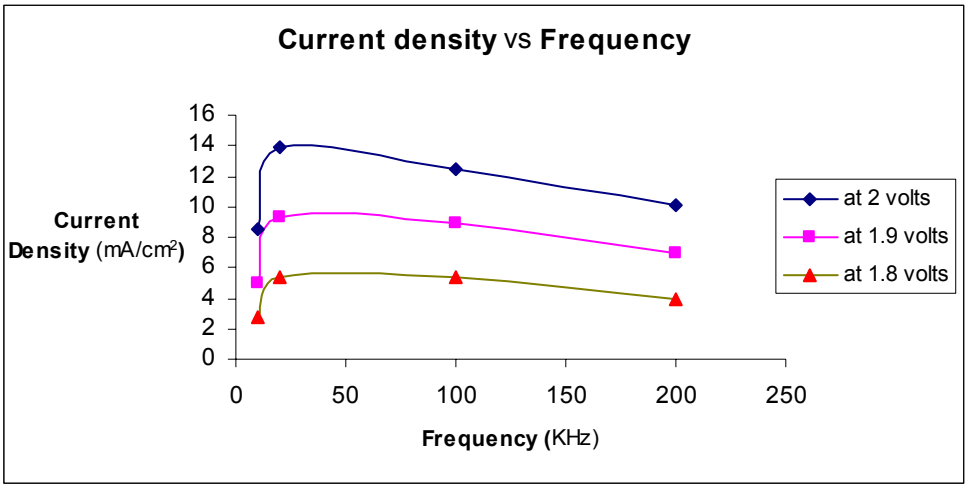

Fig 4: Power plot of average current density vs. frequency after plotting with plain nickel sheet as the anode.

The graphical analysis of these experiments clearly points out the optimum frequency of pulsed DC electroplating lies at approximately 20 KHz.

Experiment 4: Testing of electroplated samples with sintered electrode.

Specifications: Cathode: 2 × 4 inch electroplated nickel foil.

Anode: 2 × 4 inch sintered (80% Mo: 10% Al: 10% cobalt oxide)

Table 5: The current densities at different frequencies with respect to sintered electrode

Sr. No	**Frequency** (kHz)	**Current @ 1.8 V** (amp)	**Current density @ 1.8 V** (mA/cm^2)	**Current @1.9 V** (amp)	**Current density @ 1.9 V** (mA/cm^2)	**Current @ 2.0 V** (amp)	**Current density @ 2.0 V** (mA/cm^2)
1	10	1.16	22.40	0.78	15.17	0.64	12.42
2	10	1.05	20.34	0.81	15.52	0.62	12.02
3	20	1.75	33.88	1.33	25.80	0.94	18.15
4	20	1.63	31.58	1.27	24.70	0.96	18.64
5	100	1.38	26.88	0.94	20.56	0.76	14.91
6	100	1.36	26.37	0.96	20.49	0.75	14.58

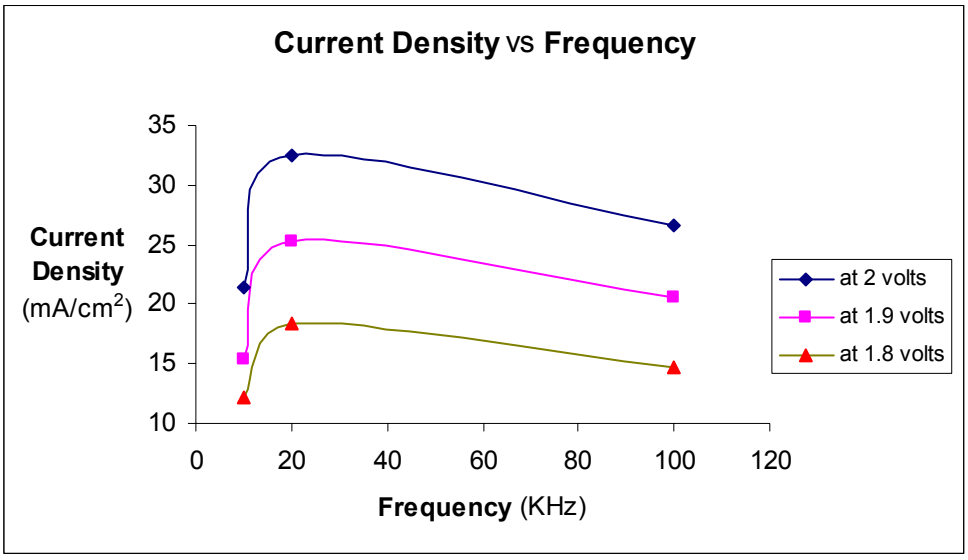

Fig 5: Power plot of current density vs. frequency after plotting with sintered electrode as an anode.

The graphical analysis after these experiments also indicates that the optimum frequency of pulsed DC electroplating with respect to high current density lies near the frequency of 20 KHz.

The measurements of current densities measured with respect to platinum foil, sintered electrode, and plain nickel sheet at different frequencies show that the optimum frequency of applied pulsed DC lies around 20 KHz. Further studies may be required to confirm the same.

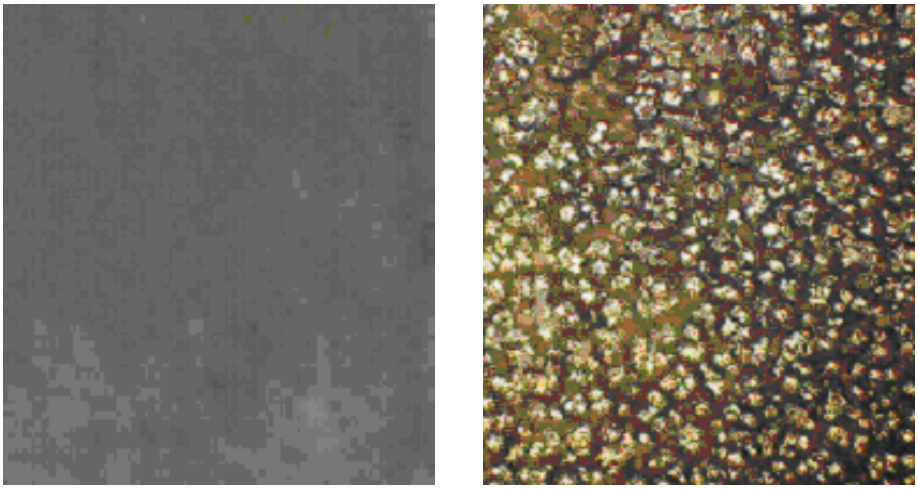

Fig 6. The photographs show an electroplated electrode sample made at the frequency of 20 KHz, without magnification (left) and with magnification of 20 × (right).

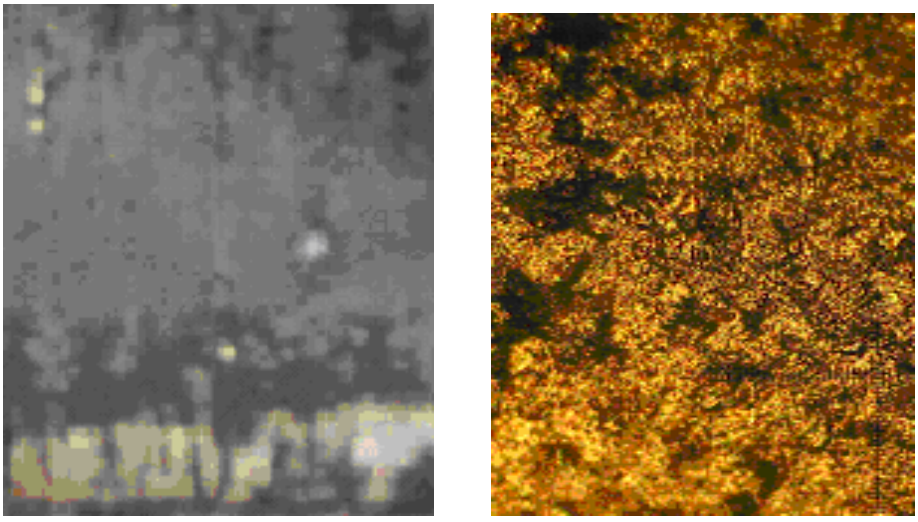

Fig 7. The pictures show an electroplated sample made at frequency of 100 KHz without magnification (left) and with magnification of 20 × (right).

The physical conditions of the electroplated samples with respect to coating uniformity and adhesion were observed in **Figures 6 and 7**. It can be seen that the adhesion is much better in the electroplated samples made at a frequency of 20 KHz than those made at 100 KHz.

The cross sectional view of the substrate and the coated electrode are shown in the following figures.

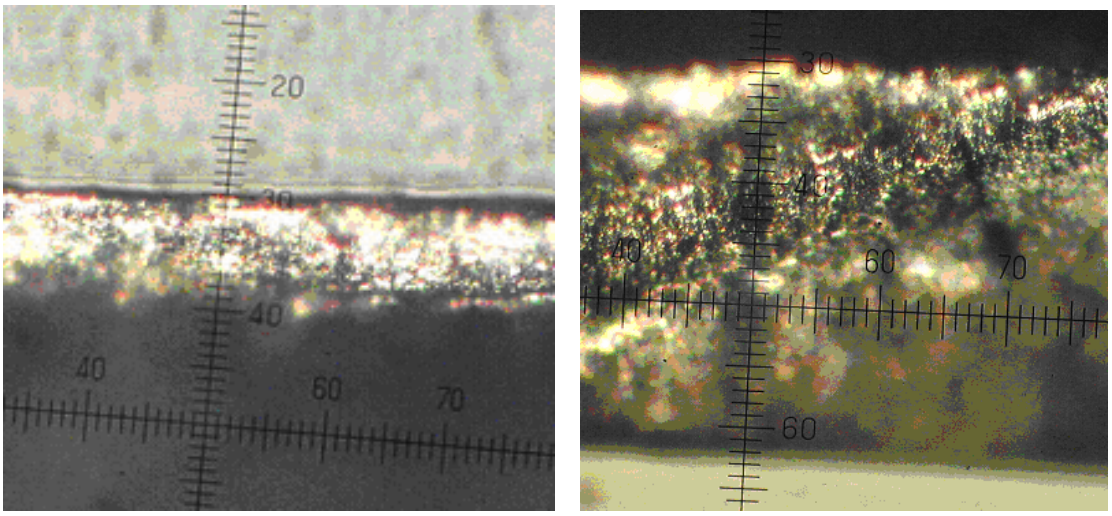

Fig 8: The pictures show cross sectional view of substrate (left) and coated electrodes at 20 × magnification (right).

The thickness of the coating, as observed at the cross section at 20× magnification indicates that the coated thickness on each side is 140 μm on both sides of the substrate. The substrate thickness is 127 μm.

Therefore, from the electrochemical studies and physical observations, it may be concluded that the samples prepared between frequencies at 20 KHz produced stronger and better porous electrocatalytic electrodes for hydrogen generation.

4. Physical Characteristics

The electroplated electrode samples prepared at 10 kHz and 20 kHz using pulsed DC power are photographed at 20 × and 10 × magnification using Olympus optical microscope. These are shown in the figures 9 and 10 in the following.

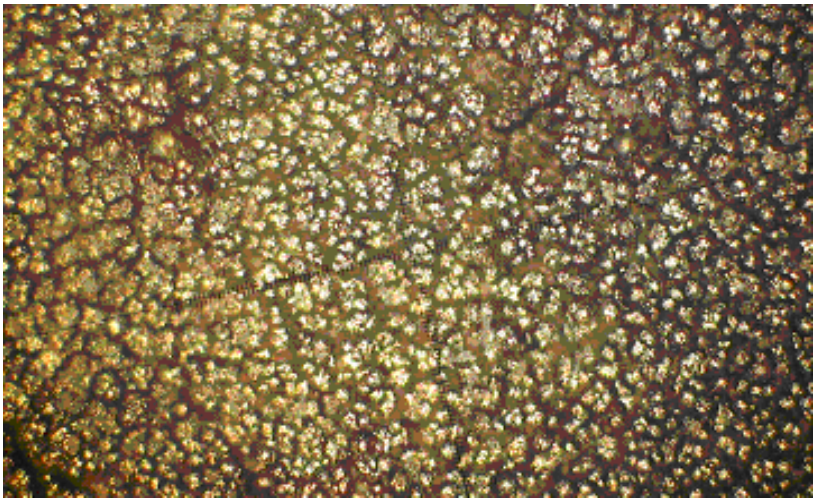

Fig 9: The above figure shows 20 × magnification of the electrode sample prepared at 20 kHz.

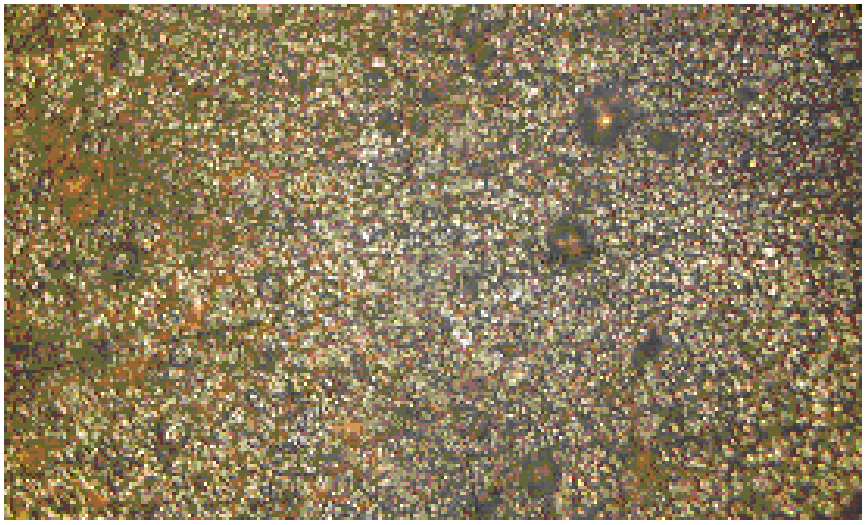

Fig 10: The above figure shows 10 × magnification of the electrode sample prepared at 20 kHz.

5. Electrochemical analysis of the electrodes

5.1. VoltaLAB set-up**:**

The Tafel plots were obtained by three electrode experiments with porous nickel electrode as cathode, platinum mesh electrode as anode, and standard calomel electrode as the reference electrode. This instrument is provided by Radiometer Analytical Cell and the model number details were PG2301 Dyanamic –EIS Voltametry VL40.

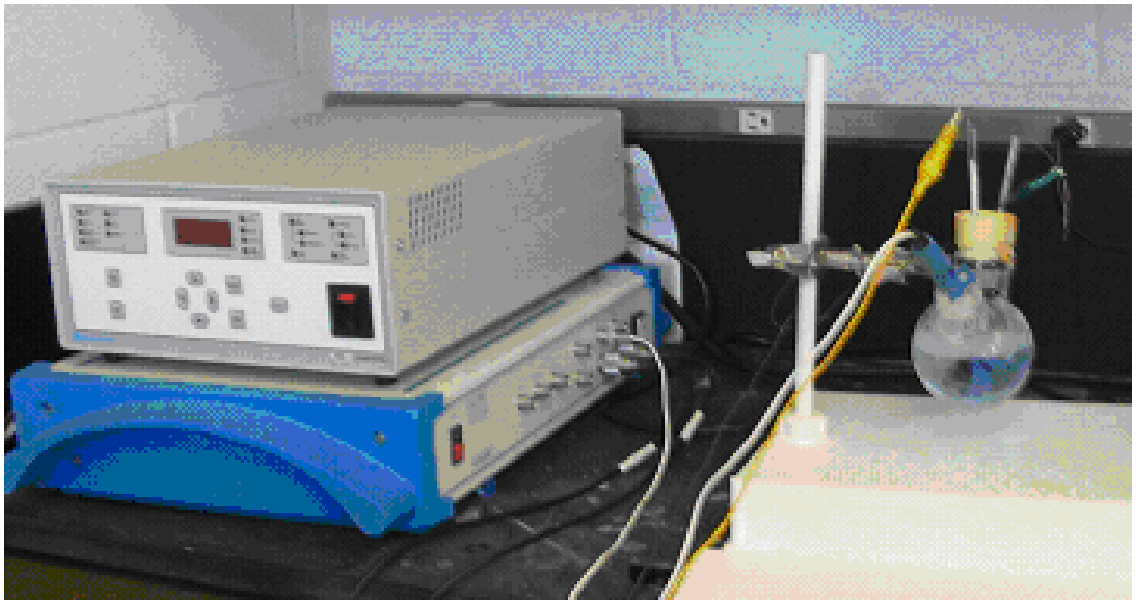

Fig 11: The set-up photograph with PG2301 Dyanamic-EIS Voltametry VL40 instrument and three electrode set-up.

The electrode is characterized by over-potential. By increasing the surface area with porous structure, the over-potential is reduced to lower values, so that, higher current density could be obtained at operating voltages. The lower potential reduces the energy losses associated in an electrochemical cell. One of the commonly used methods for determination of over-potential is by Tafel plots.

The Tafel plots for porous electrodes produced at different frequencies by pulsed DC power are shown in the following figures. These plots were drawn by sweeping the applied voltage in both directions using three electrode configurations, in which the counter electrode is platinum mesh and reference electrode is a standard calomel electrode.

5.2: Determination of over-potential by Tafel plots for electrodes prepared at different frequencies.

5.2a Tafel plots for the electrode sample made at a frequency of 10 kHz:

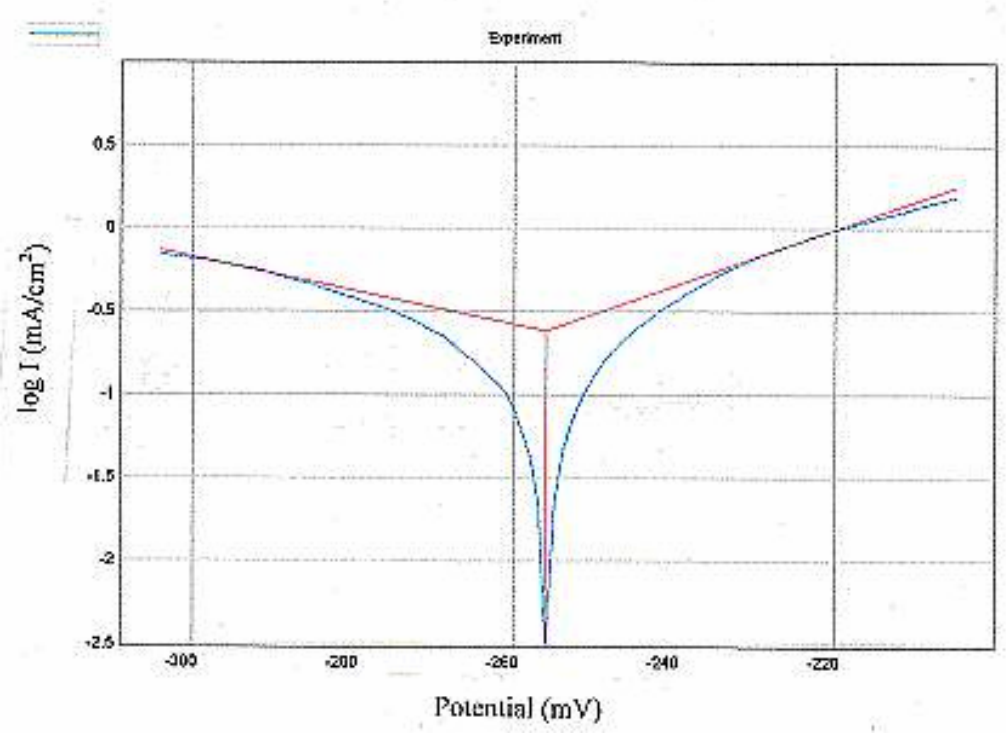

Testing Conditions:

Smoothing	9
Calculation Zone	50 mV
Segment	8mV
Atomic mass	58.69g
Valence	2
Density	8.9

The cathodic over-potential obtained from the above plot is: -99.3 mV.

5.2b: Tafel plot for the electrode sample made at the frequency of 20 kHz:

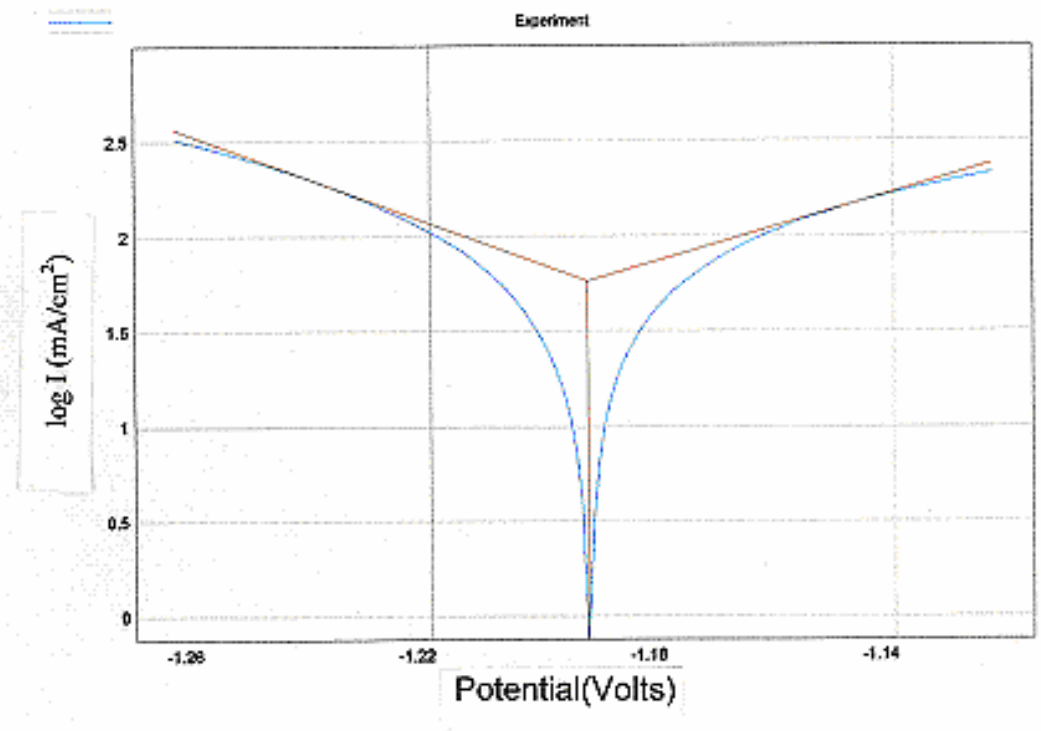

Testing Conditions:

Smoothing	9
Calculation Zone	50 mV
Segment	8mV

Atomic mass	58.69g
Valence	2
Density	8.9

The cathodic over-potential obtained from the above plot is: -88.6 mV.

5.2c: Tafel plot for the electrode sample made at the frequency of 100 kHz:

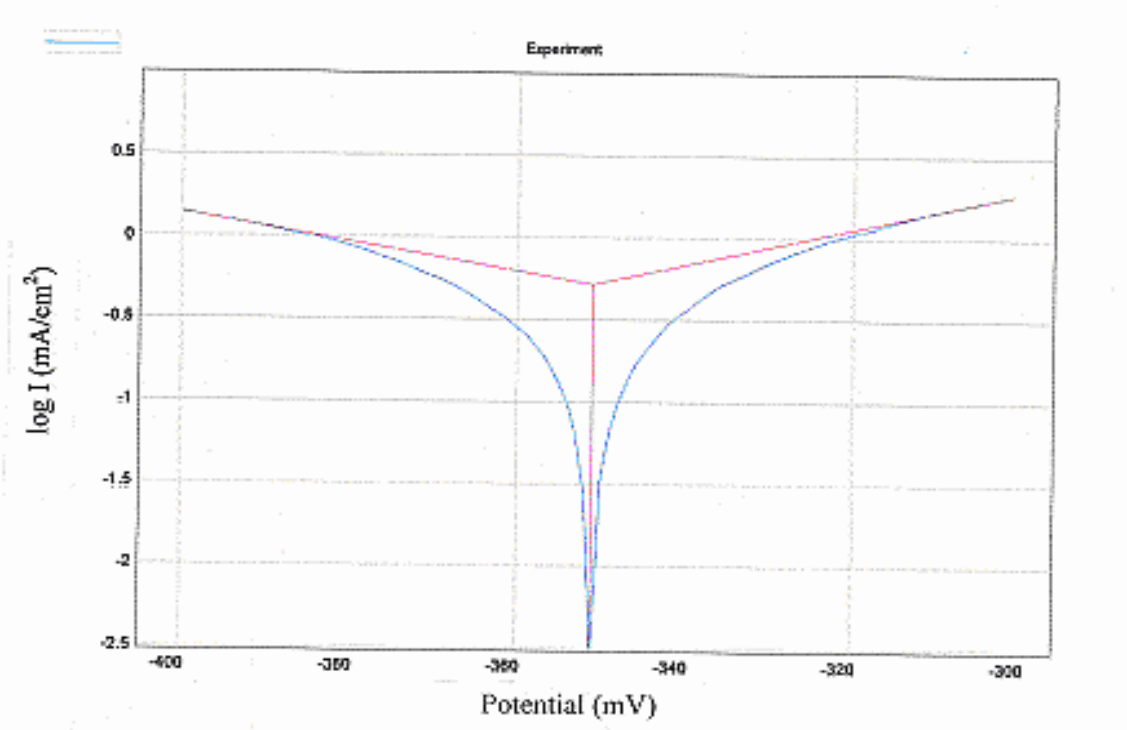

Testing Conditions:

Smoothing	9
Calculation Zone	50 mV
Segment	8mV
Atomic mass	58.69g
Valence	2
Density	8.9

The cathodic over-potential obtained from the above plot is: -113.1 mV.

Table 6: Cathodic Over-Potentials determined from Tafel Plots

Sr. No.	**Frequency** (KHz)	**Over - potential** (mV)
1	10	-99.3
2	20	-88.6
3	100	-113.1

Porous electrocatalytic electrodes produced at 20 KHz showed the lowest over-potential of 88.6 mV indicating the optimization at that applied pulsed DC frequency.

These cathodic over-potentials determined from the Tafel plots show that these electrodes show low values indicating that these experiments produced very good cathodes suitable for photoelectrochemical hydrogen generation in substrate type solar cell configuration.

The efforts by GE, University of Stuttgart, etc. are focusing on vacuum plasma sprayed porous electrodes. The cathodic over-potential in most of these plasma electrodes tend to be in the range of 80 to 150 mV. This laboratory also carried out experiments on the same. However, it has been observed that the cost of vacuum plasma sprayed electrodes is quite substantial compared to simple pulsed DC electrodes. As far as the researcher's knowledge is concerned, this is the first attempt to produce and optimize large electrodes using pulsed DC power and met with some success in this direction.

Further experiments may be needed for long term stability studies inside a photo-electrochemical hydrogen unit using triple junction amorphous silicon based substrate type solar cells for efficient generation of solar hydrogen.

6. Summary

The DC power supply based electroplated porous nickel electrodes prepared during the previous work at the laboratory showed poor adherence to the nickel substrate. Therefore pulsed DC power supply has been used to produce the porous electrodes for photoelectrochemical cells and the performance of these electrodes are analyzed and presented in this report. The applied frequencies during electroplating were varied from 10 to 100 KHz and samples of size 2 inch × 11.5 inch were prepared in the electroplating bath.

The pulsed DC electroplated porous nickel electrodes are preferred to be used as cathodes due to the fact that the strength of its adherence to the substrate including anodic dissolution is still unknown. Therefore the measurements are made using these electrodes as cathodes for the substrate type solar cells in the photoelectrochemical hydrogen generation.

The current density measurements made for 1 × 1.5 inch size electroplated porous cathode and same dimension platinum foil anode at 1.8, 1.9, and 2.0 V showed that the optimum frequency for pulsed DC plating is around 20 KHz. To confirm the observation, similar studies were conducted with different dimensions of anodes and cathodes and different anode materials. The second set included 1 × 1.5 inch size electroplated cathode with sintered Ni-Co_3O_4 anode; third set consisted of 2 × 2 inch size electroplated cathode and same size plain nickel sheet anode; the forth set with 2 × 4 inch size electroplated cathode and sintered Ni-Co_3O_4 anode. All these experiments concluded that the optimum frequency for electroplated porous nickel used as cathode

is around 20 KHz. The sintered nickel-cobalt oxide anode was prepared at this laboratory.

The comparison of physical observations of the electroplated porous electrodes prepared at 20 KHz and 100 KHz without magnification and with 20 × magnification showed that the electrode prepared at 20 KHz was adhering stronger than the electrode prepared at 100 KHz. It was observed that the electrodes deposited at 100 KHz had poor deposition.

The thickness of the electroplating was found to be about 140 μm on both sides over the plain nickel sheet of 127 μm thickness by Optical Microscope BHT series from Olympus System Inc.

The cathodic over-potential measurements were determined from the Tafel plots obtained from 3 terminal electrodes electrochemical analysis using Dynamic-EIS Voltametry, which is a part of the VoltaLAB model PG Z301. In these experiments electroplated porous electrodes were used as cathodes, platinum mesh as the anode, and standard calomel electrode as the reference electrode. The lowest cathodic over-potential was found to be 88.6 mV for electrodes prepared at 20 KHz compared to electrodes prepared at other frequencies. It may be noted that this is one of lowest over-potentials reported in the literature. The cathodic over-potential of best cathodes varies from 70 to 150 mV for the standard vacuum plasma deposited porous cathodes. This clearly indicates that the effort in developing a good electrocatalytic porous cathodes for photoelectrochemical hydrogen generation prepared by novel pulsed DC technique is a success.

6. Surface Analysis

6.1. Introduction

The development of porous electrocatalytic nickel electrodes by pulsed DC electroplating technique for photoelectrochemical hydrogen generation is reported in this task. A series of experiments were conducted from 5 to 200 KHz and led to an optimized frequency of 20 KHz pulsed DC for electroplating. This produced stable electrochemical electrodes with strong adherence to the nickel substrate. The thickness of plating was found to be around 140 μm on nickel substrate. Tafel plots obtained from the electrochemical studies using VoltaLAB showed an over-potential of 88 mV for electroplated electrodes produced at a pulsed DC frequency of 20 KHz.

More experiments were performed to view the uniformity of performance of the pulsed DC electroplated electrodes. Also the variation of current density and dynamic over-potentials were evaluated for different sizes of pulsed DC electroplated cathodes with a constant large area platinum mesh.

The purpose of the experiments were to find the variation of the dynamic over-potentials at different applied voltages, constant cathode-electrolyte potential (V_{cc}) and constant anode-electrolyte potential (V_{ac}). The following experiments have been conducted in this regards with different dimensions of the cathodes:

1. The variation of current density and dynamic over-potential for different cathode surface areas with respect to constant anode surface area and different applied voltages.

2. The variation of current density and dynamic over-potential for different cathode surface areas with respect to constant anode surface area and constant dynamic anodic over-potential (V_{ac}).
3. The variation of current density and dynamic over-potential for different cathode surface areas with respect to constant anode surface area and constant dynamic cathodic over-potential (V_{cc}).

In the proposed substrate-type photoelectrochemical solar hydrogen generator, the rear side of the triple junction amorphous silicon solar cells is negative and thus reduction reaction, i.e. hydrogen evolution occurs at the rear side of the electrochemical cell. With a triple junction solar cell generating 2.2 to 2.3 V (open circuit voltage), the operating voltage lies in the range of 1.75 to 1.90 V. In order to achieve this figure, it is essential to have the over-potential kept at a minimum to minimize the potential losses at the electrode interface. Porous nickel electroplated cathodes were prepared and their electrochemical parameters were studied with respect to large area platinum mesh anode. A large stable anode ensures low anodic over-potential and its variation is minimal with respect to the variation of small area cathodes to study the cathode characteristics.

6.2. Effect of cathode surface area on the current density and dynamic over-potentials.

6.2.1 The variation of current density and dynamic over-potential for different cathodic surface areas with respect to constant anodic surface area & different applied voltages.

Conditions of experiment:

Cathode — Electrode prepared at 20 KHz

Anode — Platinum mesh (356 cm^2 fixed area)

V_{ac}: — Voltage between anode and saturated calomel electrode.

V_{cc}: — Voltage between cathode and saturated calomel electrode.

V_{total}: — Voltage between anode and cathode.

Distance between electrodes: 3.1 cm

Area of cathode : 5.08 to 50.8 cm^2

Table 1: Current densities for different size of cathodes and its dynamic over-potential for cathodes prepared at 20 KHz pulsed DC power.

Sr. No.	**Cathode dimension** (cm)	**V_{total}** (V)	**V_{ac}** (V)	**V_{cc}** (V)	**Current** (Amp)	**Area** (cm^2)	**Current Density** (mA/cm^2)
1	5.08 X 10	1.8	0.5029	1.2100	0.336	50.8	6.61
		1.9	0.5297	1.2325	0.547	50.8	10.76
		2.0	0.5597	1.2522	0.775	50.8	15.25
2	5.08 X 9	1.8	0.5177	1.2132	0.347	45.72	7.58
		1.9	0.5362	1.2316	0.530	42.72	11.59
		2.0	0.5726	1.2438	0.734	45.72	16.05
3	5.08 X 8	1.8	0.5275	1.2147	0.237	40.64	5.83
		1.9	0.5658	1.2388	0.410	40.64	10.08
		2.0	0.5953	1.2616	0.597	40.64	14.68
4	5.08 X 7	1.8	0.5264	1.2265	0.222	35.56	6.24
		1.9	0.5569	1.2619	0.388	35.56	10.91
		2.0	0.5840	1.2915	0.592	35.56	16.64
5	5.08 X 6	1.8	0.5191	1.2358	0.234	30.48	7.67
		1.9	0.5447	1.2658	0.410	30.48	13.45
		2.0	0.5670	1.3004	0.625	30.48	20.50
6	5.08 X 5	1.8	0.5320	1.2253	0.218	25.4	8.58

		1.9	0.5591	1.2646	0.373	25.4	10.62
		2.0	0.5843	1.2958	0.556	25.4	14.76
7	5.08 X 4	1.8	0.5243	1.2417	0.208	20.32	10.23
		1.9	0.5416	1.2830	0.356	20.32	17.51
		2.0	0.5632	1.3236	0.543	20.32	26.72
8	5.08 X 3	1.8	0.5285	1.2411	0.154	15.24	10.10
		1.9	0.5651	1.2795	0.281	15.24	18.43
		2.0	0.5919	1.3158	0.415	15.24	29.19
9	5.08 X 2	1.8	0.5043	1.2658	0.142	10.13	13.97
		1.9	0.5328	1.3123	0.273	10.16	26.89
		2.0	0.5541	1.3551	0.428	10.16	42.13
10	5.08 X 1	1.8	0.4818	1.2964	0.113	5.08	22.24
		1.9	0.5073	1.3462	0.225	5.08	44.29
		2.0	0.5277	1.3972	0.369	5.08	72.63

The current density variations are plotted against the different cathode sizes, so that the performance of the cathode could be analyzed as in **Fig. 1**.

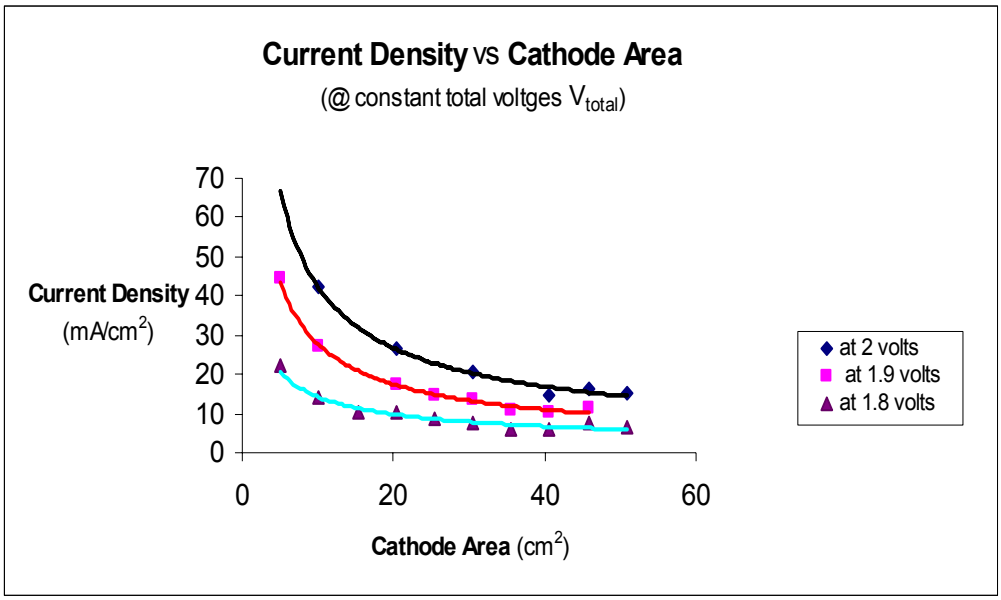

Fig. 1. The power plot of the current density versus the area of the electroplated cathode from 5.08 - 50.8 cm^2 prepared at 20 KHz with respect to constant area platinum mesh anode.

The graphical trend in the above plot indicates that as the size of the cathode increases, the current density decreases for constant anodic surface area. This may be

attributed to the increased potential drop with increase in the distance through which the current has to pass in the electrode structure.

The variation of current density with respect to dynamic cathodic over-potential (V_{cc}) between cathode and electrolytic interface at different sets of applied supply voltages at 1.8, 1.9 and 2.0 V are plotted in the **Fig. 2**.

The plotted trend indicates that the current density increases with a decrease in the size of the cathode, which in turn increases the potential between cathode and electrolyte interface (dynamic cathodic over-potential) at the same applied potential. This also indicates increase in energy losses at increased dynamic cathodic over-potential (V_{cc}).

The variation of current density with respect to dynamic anodic over-potential (V_{ac}) between the anode and electrolytic interface at different applied voltages of 1.8, 1.9 and 2.0 V are plotted in the **Fig. 3**.

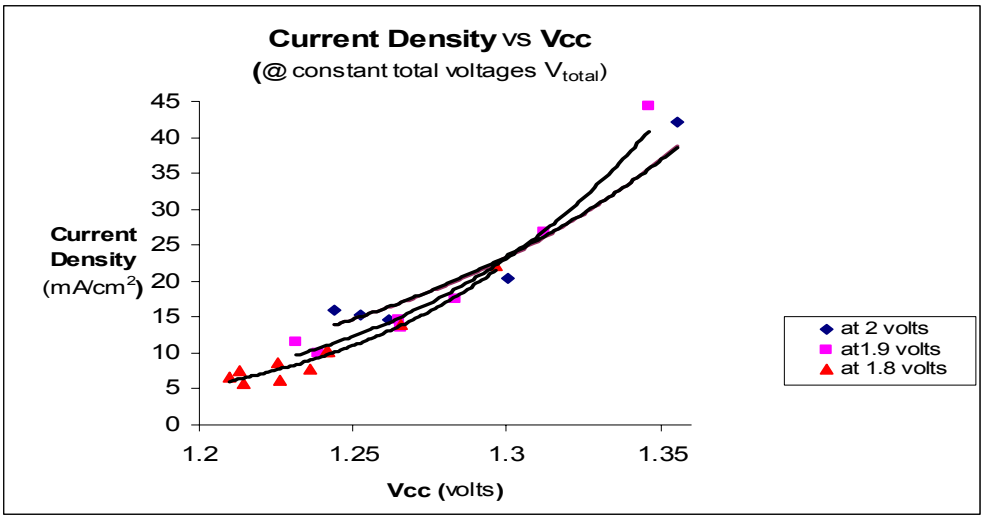

Fig. 2. The power plot of current density versus dynamic cathodic over-potential (V_{cc}) at different applied voltages.

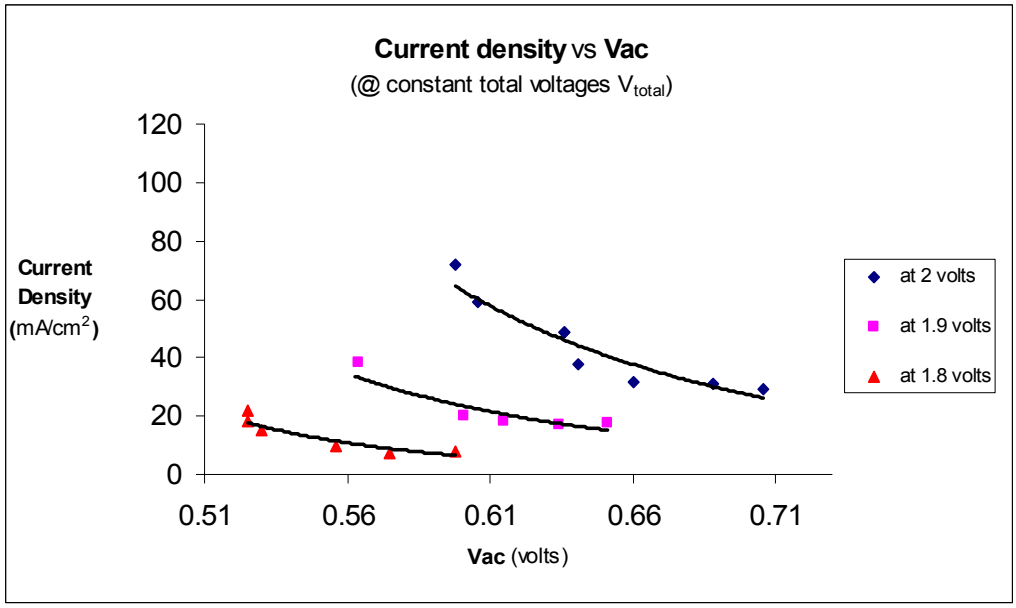

Fig. 3. The power plot of current density versus dynamic anodic over-potential (V_{ac}) at different applied voltages.

The graphical trend indicates that the current density decreases with increase in the potential between anode and electrolyte interface. This also indicates that the increase in the cathodic surface area increases the dynamic anodic over-potential (V_{ac}) for the large constant anodic surface area and different applied voltages.

6.2.2 The variation of current density and dynamic over-potential for different cathodic surface areas with respect to constant anodic surface area at different applied voltages.

Conditions of the experiment:

Cathode	Electrode prepared at 20 KHz
Anode	Platinum mesh (356 cm^2 fixed area)
Distance between electrodes	3.1 cm
Area of cathode	1 to 10 cm^2

Table 2: Current densities and dynamic over-potentials for different sizes of cathodes.

Sr. No.	**Cathode dimension** (cm)	V_{total} (V)	V_{ac} (V)	V_{cc} (V)	**Current** (Amp)	**Area** (cm^2)	**Current Density** (mA/cm^2)
1	1 X 10	1.8	0.598	1.200	0.082	10	8.2
		1.9	0.651	1.229	0.179	10	17.9
		2.0	0.706	1.253	0.294	10	29.4
2	1 X 9	1.8	0.575	1.212	0.065	9	7.22
		1.9	0.634	1.245	0.155	9	17.22
		2.0	0.688	1.273	0.277	9	30.77
3	1 X 8	1.8	0.512	1.233	0.238	8	8.5
		1.9	0.615	1.256	0.405	8	18
		2.0	0.660	1.286	0.597	8	31.75
4	1 X 7	1.8	0.556	1.234	0.070	7	10
		1.9	0.601	1.272	0.140	7	20
		2.0	0641	1.307	0.264	7	37.71
5	1 X 6	1.8	0.550	1.241	0.063	6	12.6
		1.9	0.595	1.282	0.134	6	26.8
		2.0	0.636	1.319	0.243	6	48.6
6	1 X 5	1.8	0.530	1.262	0.063	5	12.6
		1.9	0.595	1.282	0.134	5	26.8
		2.0	0.636	1.319	0.243	5	48.6
7	1 X 4	1.8	0.530	1.262	0.060	4	15
		1.9	0.571	1.306	0.127	4	31.75
		2.0	0.606	1.352	0.236	4	59
8	1 X 3	1.8	0.525	1.292	0.054	3	18
		1.9	0.564	1.316	0.115	3	38.33
		2.0	0.598	1.364	0.215	3	71.66
9	1 X 2	1.8	0.525	1.278	0.044	2	22
		1.9	0.564	1.330	0.096	2	48
		2.0	0.598	1.381	0.178	2	89
10	1 X 1	1.8	0.524	1.281	0.028	1	28
		1.9	0.563	1.328	0.275	1	59
		2.0	0.598	1.383	0.474	1	110

The current density variations are plotted against the different cathode sizes, so that the performance of the cathode could be analyzed as shown in **Fig. 4**.

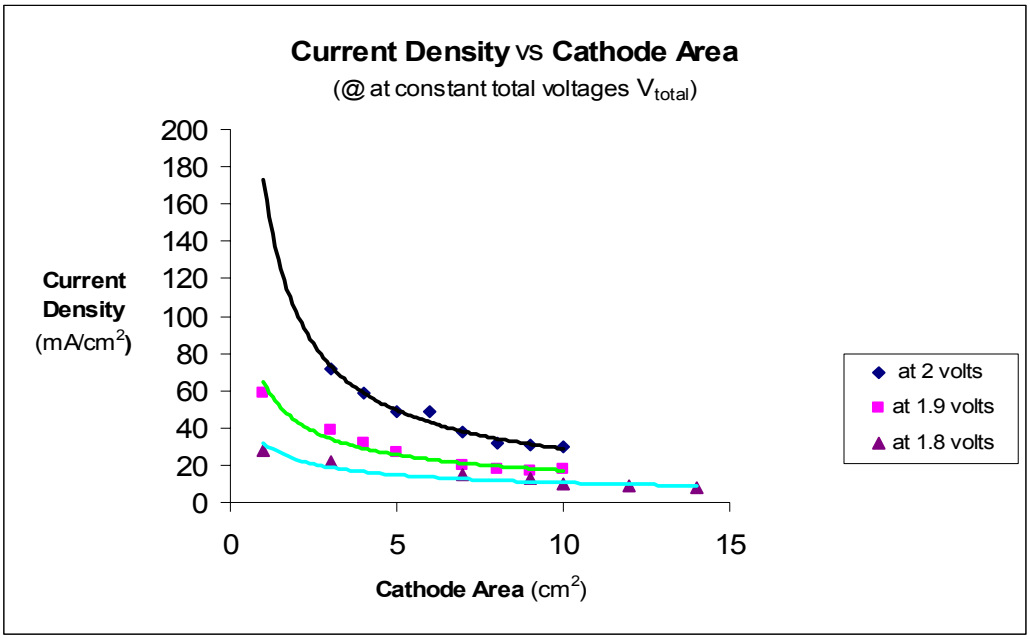

Fig. 4. The power plot of the current density versus the area of the electroplated cathode from 1 - 10 cm^2 prepared at 20 KHz with respect to constant area platinum mesh anode.

.

The graphical trend in the above plot indicates that as the size of the cathode increases, the current density decreases for constant applied voltage and constant anodic surface area. This may be attributed to the increased potential drop with increase in the distance through which the current has to pass in the electrode structure.

Fig. 5 presents the overall trend i.e. decrease in current density with increase in the dimension of the cathode for constant anode dimension and same sets of applied voltage over the size variations from 1 cm^2 to 50.8 cm^2.

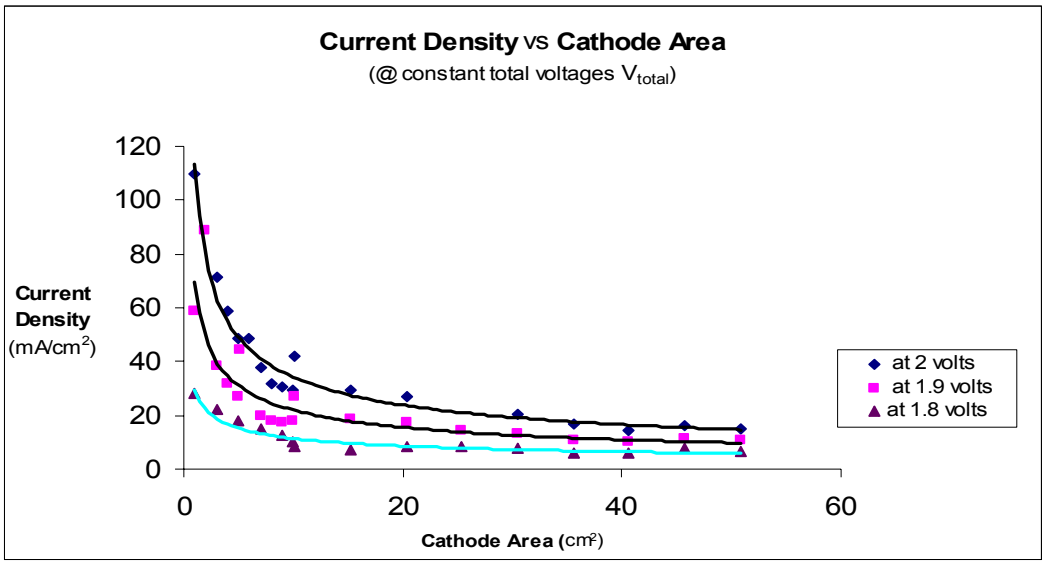

Fig. 5. The power plot of the current density versus the area of the electroplated cathode from 1 - 50.8 cm^2 prepared at 20 KHz with respect to constant area platinum mesh anode.

The variation of current density with respect to dynamic cathodic over-potential (V_{cc}) between cathode and electrolytic interface at different applied supply voltages at 1.8, 1.9 and 2.0 V are plotted in **Fig. 6**.

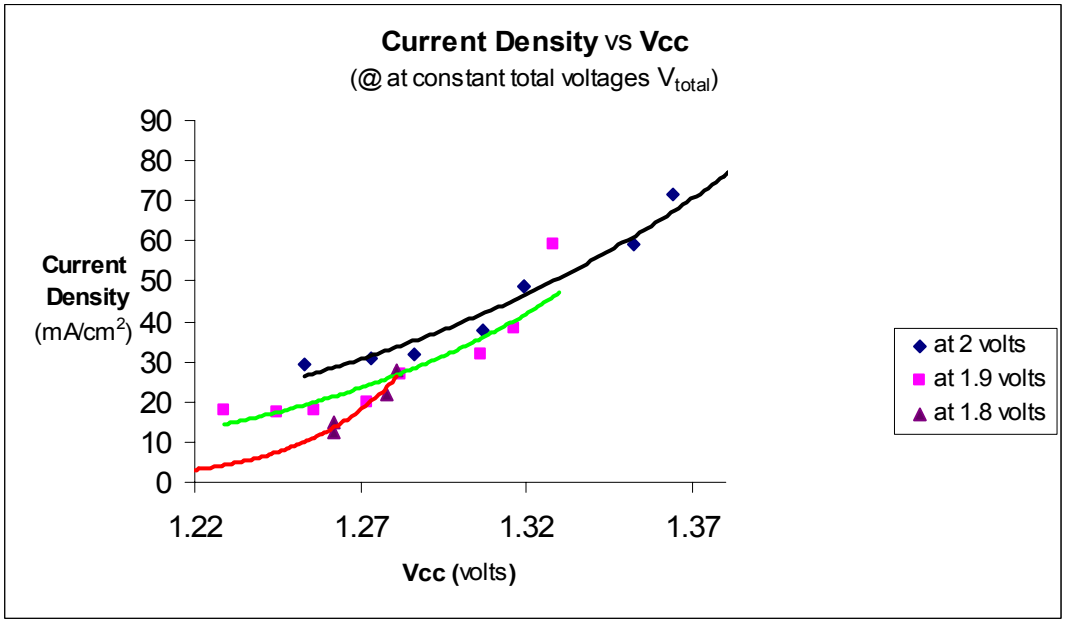

Fig. 6. The power plot of current density versus dynamic cathodic over-potential (V_{cc}) at different applied voltages.

The graphical analysis of the experiment shows that as the current density increases, increase in the dynamic cathodic over-potential (V_{cc}) is observed. It suggests that as we decrease the cathodic surface area, energy losses increases.

The variation of current density with respect to dynamic anodic over-potential (V_{ac}) between anode and electrolytic interface at different applied voltages at 1.8, 1.9 and 2.0 V are plotted in **Fig. 7**.

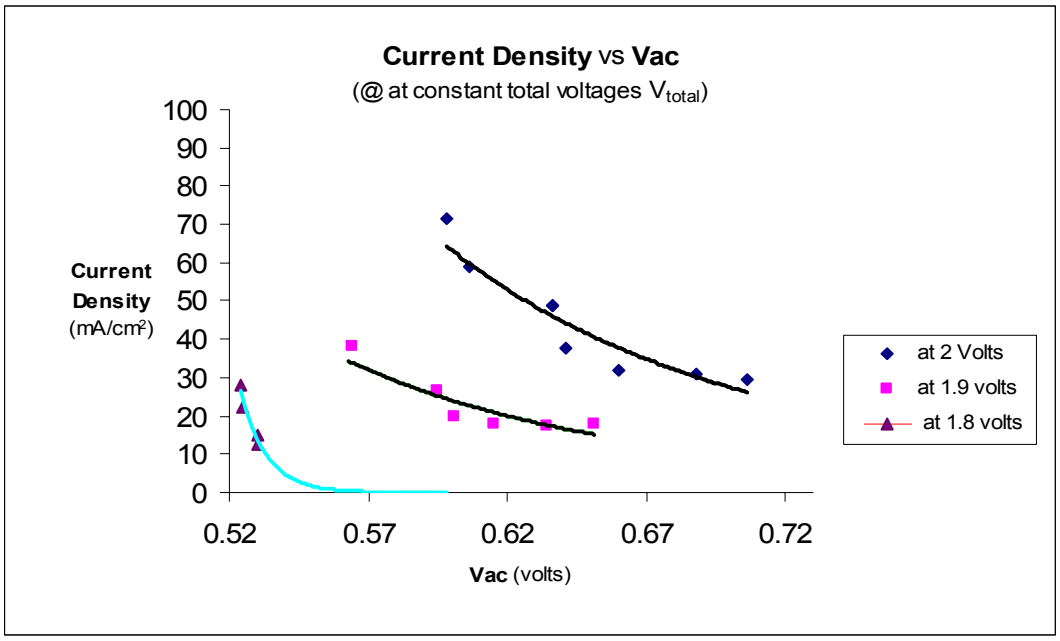

Fig. 7. The power plot of current density versus the voltage of the anode (V_{ac}) with reference to saturated calomel electrode.

The graphical trend indicates that as the current density decreases, there is an increase in the potential between anode and electrolyte interface. This also indicates that an increase in the cathodic surface area increases the dynamic anodic over-potential for the constant anodic surface area and constant applied voltage.

6.2.3. The variation of current density and dynamic over-potential for different cathodic surface areas with respect to constant anodic surface area and constant dynamic anodic over-potential (V_{ac}).

Conditions of the experiment:

Cathode	Electrode prepared at 20 KHz
Anode	Platinum mesh (356 cm^2 fixed area)
Distance between electrodes	3.1 cm
Area of cathode	1 to 10 cm^2

Table 3: Current densities for different size of cathodes and their dynamic over-potentials.

Sr. No.	**Cathode dimension** (cm)	**V_{total}** (V)	**V_{ac}** (V)	**V_{cc}** (V)	**Current** (Amp)	**Area** (cm^2)	**Current Density** (mA/cm^2)
1	1 X 10	1.839	0.610	1.216	0.106	10	10.6
		1.908	0.660	1.231	0.142	10	14.2
		1.998	0.710	1.253	0.248	10	24.8
2	1 X 9	1.854	0.610	1.230	0.100	9	11.11
		1.950	0.660	1.259	0.199	9	22.11
		2.044	0.710	1.283	0.326	9	36.22
3	1 X 8	1.884	0.610	1.233	0.118	8	14.75
		20.19	0.660	1.296	0.293	8	36.62
		2.0129	0.710	1.318	0.440	8	55
4	1 X 7	1.907	0.610	1.272	0.139	7	19.85
		20.44	0.660	1.324	0.326	7	46.65
		2.184	0.710	1.365	0.543	7	77.57
6	1 X 5	1.929	0.610	1.291	0.151	5	30.2
		2.083	0.660	1.352	0.363	5	72.6
		2.246	0.710	1.409	0.618	5	123.6
7	1 X 4	2.005	0.610	1.353	0.240	4	60
		2.206	0.660	1.447	0.529	4	132.25
		2.386	0.710	1.527	0.786	4	196.5
8	1 X 3	2.038	0.610	1.383	0.261	3	87
		2.253	0.660	1.492	0.571	3	190.33
		2.498	0.710	1.617	0.961	3	320.33

9	1 X 2	2.028	0.610	1.387	0.190	2	95
		2.177	0.660	1.467	0.334	2	167
		2.371	0.770	1.572	0.562	2	281
10	1 X 1	2.034	0.610	1.398	0.128	1	128
		2.236	0.660	1.517	0.275	1	275
		2.483	0.710	1.668	0.474	1	474

Current density variations are plotted against the different cathode sizes, so that the performance of the cathode could be analyzed as shown in **Fig. 8**.

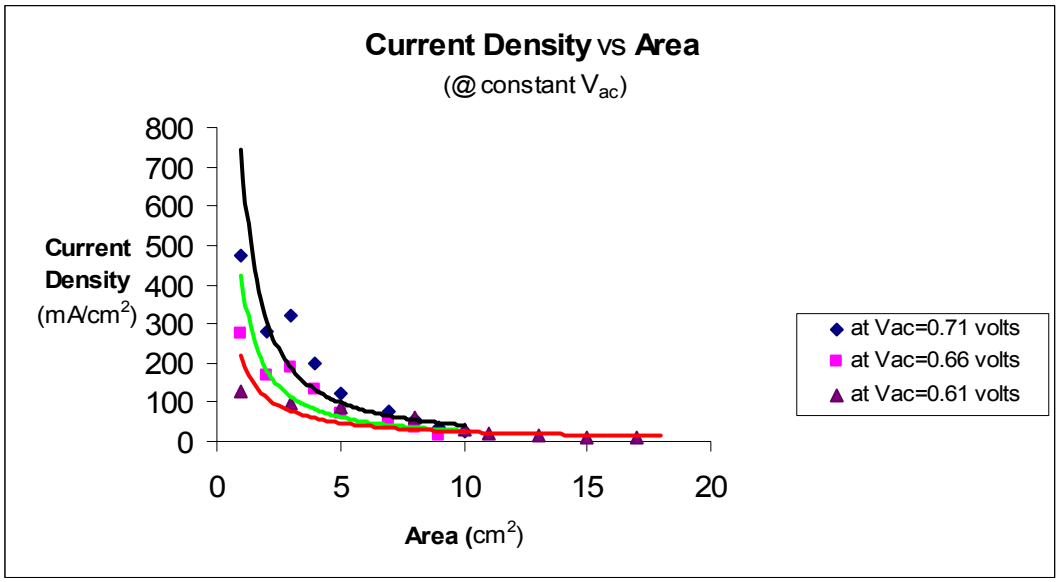

Fig. 8. The power plot of the current density versus the area of the DC pulsed electroplated cathode.

The graphical trend in the above plot indicates that as the size of the cathode increases, the current density again decreases for constant dynamic anodic over-potential (V_{ac}) and constant anodic surface area.

The variation of current density with respect to dynamic cathodic over-potential between cathode and electrolytic interface with constant anode voltages as plotted in **Fig. 9**.

The graphical analysis of the experiment shows that as the current density increases, increase in the dynamic cathodic over-potential is observed for constant sets

of dynamic anodic over-potential (V_{ac}) and constant anodic surface area. It suggests that as we decrease the cathodic surface area, energy losses increases.

6.2.4 The variation of current density and dynamic over-potential for different cathodic surface areas with respect to constant anodic surface area and constant dynamic anodic over-potential (V_{ac}).

Conditions of the experiment:

Cathode	Electrode prepared at 20 KHz
Anode	Platinum mesh (356 cm^2 fixed area)
Distance between electrodes	3.1 cm
Area of cathode	5.08 to 50.8 cm^2

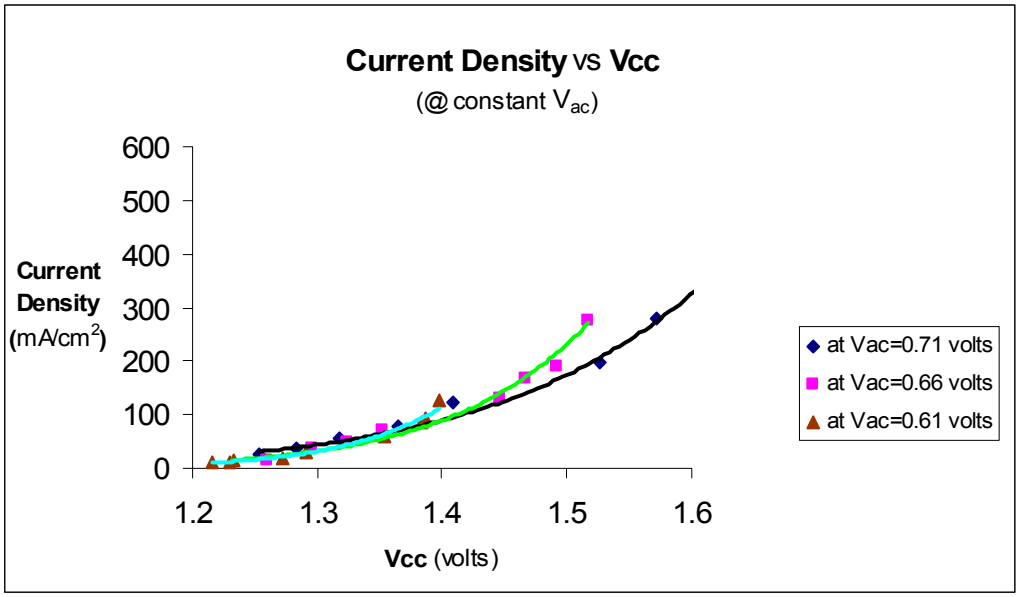

Fig. 9. The power plot of current density with the voltage of the cathode (V_{cc}) with reference to saturated calomel electrode when the voltage at the anode with reference to saturated calomel is constant.

Table 4: Current densities for different sizes of cathodes and their dynamic over-potentials.

Sr. No.	**Cathode dimension** (cm)	V_{total} (V)	V_{ac} (V)	V_{cc} (V)	**Current** (Amp)	**Area** (cm^2)	**Current Density** (mA/cm^2)
1	5.08 X 10	1.806	0.520	1.2201	0.430	50.8	8.46
		1.835	0.530	1.2236	0.498	50.8	9.80
		1.867	0.540	1.2287	0.566	50.8	11.14
2	5.08 X 9	1.825	0.520	1.2047	0.304	45.72	6.65
		1.862	0.530	1.2196	0.436	42.72	9.53
		1.910	0.540	1.2312	0.534	45.72	11.68
3	5.08 X 8	1.809	0.520	1.2197	0.261	40.64	6.42
		1.825	0.530	1.2249	0.292	40.64	7.18
		1.862	0.540	1.2328	0.351	40.64	8.63
4	5.08 X 7	1.801	0.520	1.2344	0.224	35.56	6.29
		1.841	0.530	1.2478	0.289	35.56	8.13
		1.877	0.540	1.2593	0.351	35.56	9.87
5	5.08 X 6	1.817	0.520	1.2422	0.238	30.48	7.81
		1.865	0.530	1.2596	0.324	30.48	10.62
		1.920	0.540	1.2814	0.450	30.48	14.76
6	5.08 X 5	1.799	0.520	1.2323	0.216	25.4	8.50
		1.828	0.530	1.2427	0.262	25.4	10.31
		1.859	0.540	1.2508	0.317	25.4	12.48
7	5.08 X 4	1.815	0.520	1.2497	0.216	20.32	10.63
		1.854	0.530	1.2661	0.274	20.32	13.48
		1.893	0.540	1.2824	0.342	20.32	16.83
8	5.08 X 3	1.787	0.520	1.2376	0.136	15.24	8.92
		1.812	0.530	1.2469	0.162	15.24	10.63
		1.842	0.540	1.2596	0.201	15.24	13.18
9	5.08 X 2	1.856	0.520	1.2927	0.204	10.13	20.07
		1.896	0.530	1.3110	0.259	10.16	25.49
		1.939	0.540	1.3301	0.326	10.16	32.08
10	5.08 X 1	1.957	0.520	1.3744	0.301	5.08	59.25
		2.015	0.530	1.4036	0.386	5.08	75.98
		2.072	0.540	1.4324	0.480	5.08	94.48

The variations of current density with reference to different sizes of the cathode with anode having constant area and at constant anode voltage are shown in **Fig. 10**.

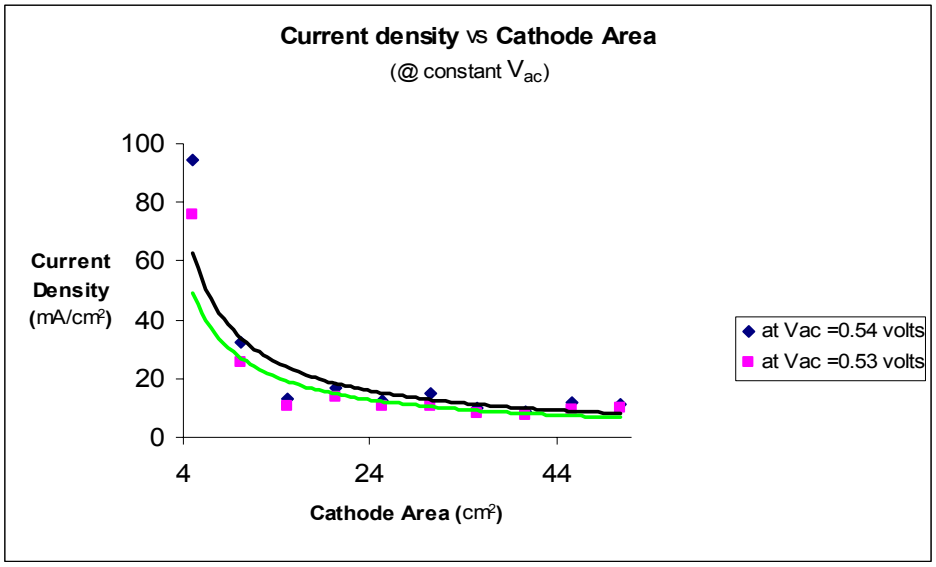

Fig. 10. The power plot of current density versus area of the DC pulsed electroplated cathode with constant voltage of the anode with respect to saturated calomel.

The profile of the graph shows that as the surface area is decreased for the cathode there is an increase in the current density for constant dynamic anodic over-potential (V_{ac}) and constant anodic surface area. This may be attributed to the increased potential drop with increase in the distance through which the current has to pass in the electrode structure.

The variations of current density with respect to dynamic cathodic over-potential between cathode and electrolytic interface, with constant anode area and at constant anode voltages for different sizes of the cathode are shown in **Fig. 11**.

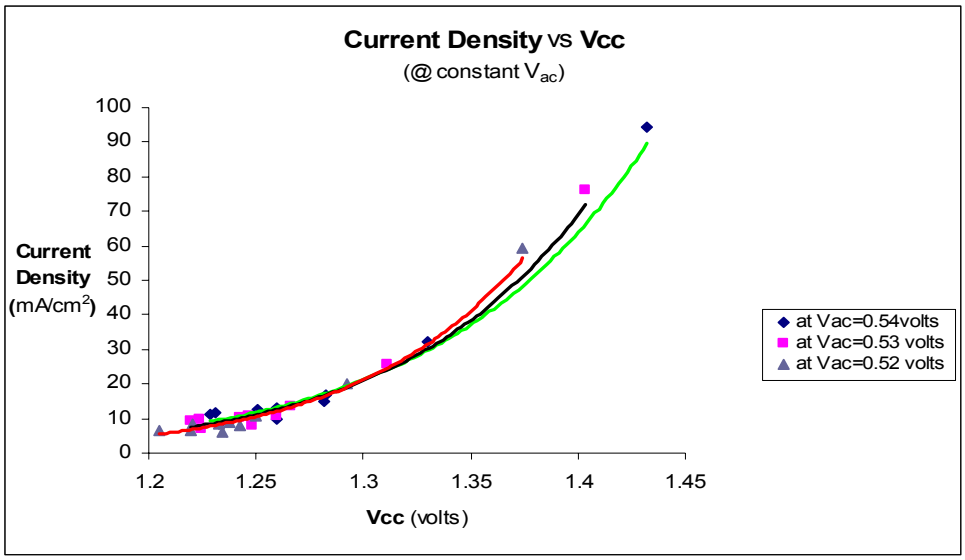

Fig. 11. The power plot of current density versus voltage of cathode (V_{cc}) with constant anode voltage with respect to saturated calomel.

The graphical analysis of the experiment shows that as the current density increases, increase in the dynamic cathodic over-potential is observed. It suggests that even with constant anode voltage the trend is continually observed i.e. as we decrease the cathodic surface area, energy losses increase.

6.2.5 The variation of current density and dynamic over-potential for different cathodic surface areas with respect to constant anodic surface area and constant dynamic anodic over-potential (V_{ac}).

Conditions of the experiment:

Cathode	Electrode prepared at 20 KHz
Anode	Platinum mesh (356 cm^2 fixed area)
Distance between electrodes	3.1 cm
Area of cathode	1 to 10 cm^2

Table 5: Current densities for different size of cathodes and their dynamic over-potentials.

Sr. No.	Cathode dimension (cm)	V_{total} (V)	V_{ac} (V)	V_{cc} (V)	Current (Amp)	Area (cm^2)	Current Density (mA/cm^2)
1	1 X 10	1.73	0.525	1.185	0.177	10	17.7
	1 X 10	1.821	0.55	1.225	0.374	10	37.4
	1 X 10	1.911	0.575	1.260	0.620	10	62
	1 X 10	2.001	0.600	1.294	0.902	10	90.2
	1 X 10	2.105	0.625	1.330	1.247	10	124.7
	1 X 10	2.222	0.650	1.372	1.666	10	166.6
	1 X 10	2.342	0.675	1.414	2.105	10	210.5
	1 X 10	2.497	0.700	1.459	2.735	10	273.5
2	1 X 9	1.774	0.525	1.226	0.176	9	19.55
	1 X 9	1.869	0.55	1.266	0.360	9	40
	1 X 9	1.953	0.575	1.298	0.562	9	62.44
	1 X 9	2.051	0.600	1.335	0.832	9	92.44
	1 X 9	2.172	0.625	1.378	1.194	9	132.66
	1 X 9	2.295	0.650	1.422	1.593	9	177
	1 X 9	2.447	0.675	1.475	2.078	9	230.88
	1 X 9	2.598	0.700	1.528	2.581	9	286.77
3	1 X 8	1.794	0.525	1.248	0.198	8	24.75
	1 X 8	1.903	0.55	1.298	0.447	8	55.87
	1 X 8	2.015	0.575	1.345	0.778	8	97.25
	1 X 8	2.133	0.600	1.395	1.164	8	145.51
	1 X 8	2.305	0.625	1.467	1.786	8	223.25
	1 X 8	2.479	0.650	1.533	2.345	8	293.12
	1 X 8	2.673	0.675	1.611	3.021	8	377.62
	1 X 8	2.823	0.700	1.673	3.566	8	445.75
4	1 X 7	1.811	0.525	1.261	0.191	7	27.28
	1 X 7	1.936	0.55	1.331	0.433	7	61.85
	1 X 7	2.119	0.575	1.431	0.897	7	128.14
	1 X 7	2.403	0.600	1.590	1.720	7	245.71
	1 X 7	2.742	0.625	1.780	2.715	7	387.85
	1 X 7	3.177	0.650	2.036	3.975	7	567.85
	1 X 7	3.653	0.675	2.308	5.42	7	774.28
5	1 X 6	1.810	0.525	1.258	0.140	6	23.33
	1 X 6	1.863	0.55	1.277	0.216	6	36
	1 X 6	1.948	0.575	1.316	0.372	6	62
	1 X 6	2.060	0.600	1.366	0.627	6	104.5
	1 X 6	2.225	0.625	1.439	1.070	6	178.33
	1 X 6	2.429	0.650	1.530	1.646	6	274.33
	1 X 6	2.668	0.675	1.639	2.373	6	395.5
	1 X 6	2.993	0.700	1.792	3.447	6	573.5

6	1 X 5	1.824	0.525	1.272	0.179	5	35.8
	1 X 5	1.943	0.55	1.336	0.400	5	80
	1 X 5	2.112	0.575	1.424	0.787	5	157.4
	1 X 5	2.349	0.600	1.548	1.404	5	280.8
	1 X 5	2.741	0.625	1.755	2.503	5	500.6
	1 X 5	3.222	0.650	2.007	3.914	5	782.8
	1 X 5	3.652	0.675	2.269	5.230	5	1046
7	1 X 4	1.814	0.525	1.266	0.159	4	39.75
	1 X 4	1.924	0.55	1.324	0.342	4	85.5
	1 X 4	2.074	0.575	1.404	0.649	4	162.25
	1 X 4	2.276	0.600	1.513	1.116	4	279
	1 X 4	2.510	0.625	1.642	1.685	4	421.25
	1 X 4	2.866	0.650	1.838	2.585	4	646.25
	1 X 4	3.208	0.675	2.043	3.500	4	875
	1 X 4	3.578	0.700	2.265	4.570	4	1142.5
8	1 X 3	1.828	0.525	1.286	0.145	3	48.33
	1 X 3	1.960	0.55	1.364	0.343	3	114.33
	1 X 3	2.108	0.575	1.454	0.617	3	205.33
	1 X 3	2.336	0.600	1.598	1.083	3	361
	1 X 3	2.674	0.625	1.816	1.795	3	598.33
	1 X 3	3.037	0.650	2.052	2.612	3	870.66
	1 X 3	3.503	0.675	2.353	3.675	3	1225
	1 X 3	3.937	0.700	2.638	4.69	3	1563.3
9	1 X 2	1.907	0.525	1.351	0.230	2	115
	1 X 2	2.064	0.55	1.456	0.451	2	225.5
	1 X 2	2.325	0.575	1.638	0.861	2	430.5
	1 X 2	2.615	0.600	1.843	1.352	2	676
	1 X 2	3.060	0.625	2.163	2.125	2	1062.5
	1 X 2	3.635	0.650	2.578	3.149	2	1574.5
	1 X 2	4.17	0.675	2.972	4.14	2	2070
10	1 X 1	2.111	0.525	1.539	0.356	1	356
	1 X 1	2.490	0.55	1.837	0.766	1	766
	1 X 1	2.997	0.575	2.243	1.364	1	1364
	1 X 1	3.726	0.600	2.835	2.262	1	2262
	1 X 1	4.74	0.625	3.676	3.556	1	3556
	1 X 1	6.06	0.650	4.76	5.20	1	5200

The current density variations are plotted against the different cathode sizes, so that the performance of the cathode could be analyzed as shown in **Fig. 12**.

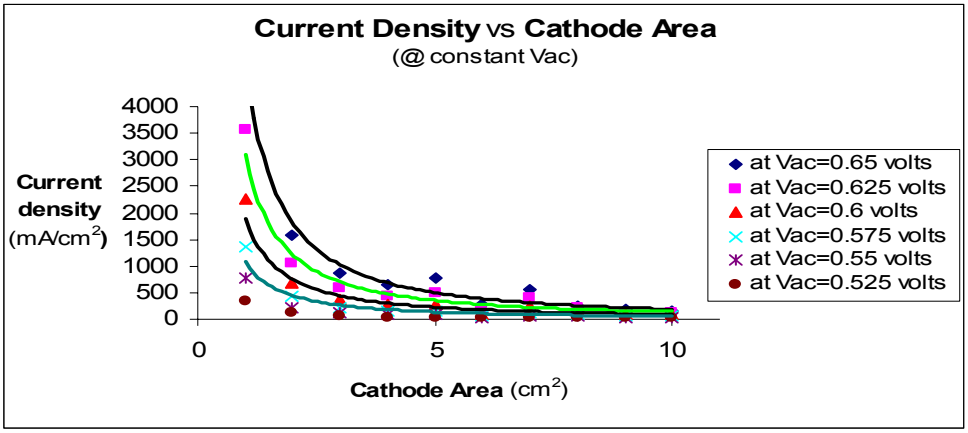

Fig. 12. The power plot of the current density versus the area of the DC pulsed, electroplated cathode.

The graphical trend in the above plot indicates that as the size of the cathode increases, the current density decreases for constant sets of anode voltages and constant anodic surface area. This may be attributed to the increased potential drop with increase in the distance through which the current has to pass in the electrode structure.

The variation of current density with respect to dynamic cathodic over-potential (V_{cc}) between cathode and electrolytic interface with constant anode voltages are plotted in **Fig. 13**.

The graphical analysis of the experiment shows that as the current density increases an increase in the dynamic cathodic over-potential is observed as seen from previous experiments. It suggests that as we decrease the cathodic surface area, energy losses increase.

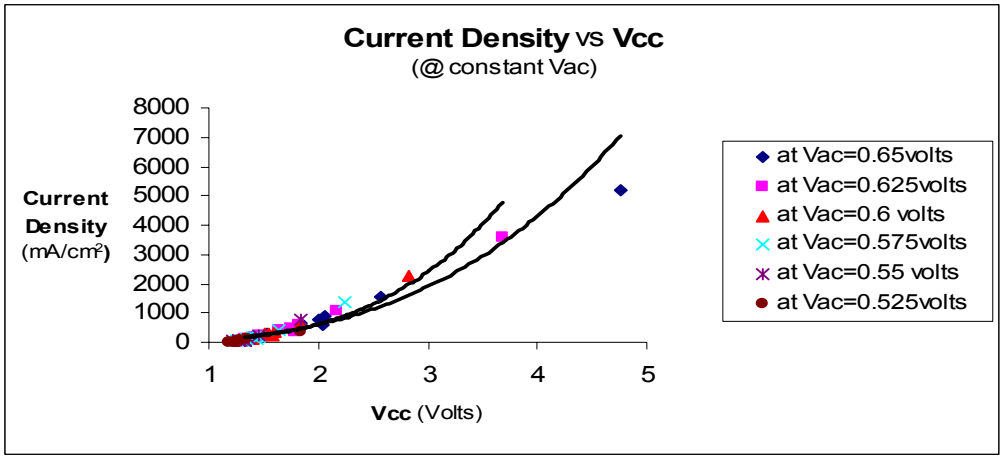

Fig. 13. The power plot of current density with the voltage of the cathode (V_{cc}) with reference to saturated calomel electrode when the voltage at the anode with reference to saturated calomel as constant.

6.2.6 The variation of current density and dynamic over-potential for different cathodic surface areas with respect to constant anodic surface area and constant dynamic cathodic over-potential (V_{cc}).

Conditions of the experiment:

Cathode	Electrode prepared at 20 KHz
Anode	Platinum mesh (356 cm^2 fixed area)
Distance between electrodes	3.1 cm
Area of cathode	1 to 10 cm^2

Table 6: Current densities for different size of cathodes and their dynamic over-potentials.

Sr. No.	**Cathode dimension** (cm)	**V_{total}** (V)	**V_{ac}** (V)	**V_{cc}** (V)	**Current** (Amp)	**Area** (cm^2)	**Current Density** (mA/cm^2)
1	1 X 10	1.719	0.515	1.18	0.163	10	16.3
	1 X 10	1.731	0.518	1.19	0.184	10	18.4
	1 X 10	1.752	0.524	1.20	0.225	10	22.5

	1 X 10	1.813	0.544	1.225	0.348	10	34.8
	1 X 10	1.880	0.564	1.25	0.524	10	52.4
	1 X 10	1.942	0.580	1.275	0.715	10	71.5
	1 X 10	2.005	0.600	1.30	0.870	10	87.0
	1 X 10	2.167	0.646	1.35	1.400	10	140.5
2	1 X 9	1.675	0.476	1.18	0.075	9	8.33
	1 X 9	1.687	0.480	1.19	0.091	9	10.11
	1 X 9	1.711	0.485	1.20	0.118	9	13.11
	1 X 9	1.745	0.495	1.225	0.167	9	18.55
	1 X 9	1.807	0.515	1.25	0.278	9	30.88
	1 X 9	1.863	0.527	1.275	0.410	9	45.55
	1 X 9	1.923	0.542	1.30	0.564	9	62.66
	1 X 9	2.066	0.574	1.35	0.990	9	110
3	1 X 8	1.671	0.478	1.18	0.063	8	7.87
	1 X 8	1.683	0.481	1.19	0.073	8	9.12
	1 X 8	1.705	0.487	1.20	0.096	8	12
	1 X 8	1.739	0.496	1.225	0.136	8	17
	1 X 8	1.783	0.507	1.25	0.209	8	26.12
	1 X 8	1.831	0.518	1.275	0.308	8	38.5
	1 X 8	1.894	0.537	1.30	0.466	8	58.25
	1 X 8	2.014	0.565	1.35	0.796	8	99.5
4	1 X 7	1.655	0.478	1.18	0.057	7	8.14
	1 X 7	1.681	0.482	1.19	0.067	7	9.57
	1 X 7	1.704	0.486	1.20	0.088	7	12.57
	1 X 7	1.736	0.493	1.225	0.124	7	17.71
	1 X 7	1.771	0.500	1.25	0.172	7	24.57
	1 X 7	1.812	0.507	1.275	0.240	7	34.28
	1 X 7	1.858	0.515	1.30	0.326	7	46.57
	1 X 7	1.939	0.527	1.35	0.508	7	72.71
5	1 X 6	1.691	0.488	1.18	0.066	6	11
	1 X 6	1.703	0.490	1.19	0.078	6	13
	1 X 6	1.710	0.493	1.20	0.090	6	15
	1 X 6	1.746	0.500	1.225	0.131	6	21.83
	1 X 6	1.784	0.508	1.25	0.182	6	30.33
	1 X 6	1.830	0.517	1.275	0.259	6	43.16
	1 X 6	1.879	0.528	1.30	0.356	6	59.33
	1 X 6	1.990	0.548	1.35	0.614	6	102.33
6	1 X 5	1.667	0.475	1.18	0.046	5	9.2
	1 X 5	1.677	0.478	1.19	0.053	5	10.6
	1 X 5	1.693	0.481	1.20	0.062	5	12.4
	1 X 5	1.735	0.490	1.225	0.098	5	19.6
	1 X 5	1.777	0.499	1.25	0.140	5	28
	1 X 5	1.818	0.507	1.275	0.200	5	40
	1 X 5	1.872	0.517	1.30	0.290	5	58
	1 X 5	1.977	0.532	1.35	0.494	5	98.8

7	1 X 4	1.663	0.476	1.18	0.038	4	9.5
	1 X 4	1.695	0.480	1.19	0.046	4	11.5
	1 X 4	1.795	0.484	1.20	0.057	4	14.25
	1 X 4	1.730	0.493	1.225	0.086	4	21.5
	1 X 4	1.776	0.504	1.25	0.136	4	34
	1 X 4	1.815	0.514	1.275	0.190	4	47.5
	1 X 4	1.868	0.526	1.30	0.276	4	69
	1 X 4	1.949	0.542	1.35	0.432	4	108
8	1 X 3	1.652	0.469	1.18	0.032	3	10.6
	1 X 3	1.669	0.473	1.19	0.039	3	13
	1 X 3	1.683	0.475	1.20	0.045	3	15
	1 X 3	1.723	0.484	1.225	0.070	3	23.3
	1 X 3	1.754	0.491	1.25	0.094	3	31.33
	1 X 3	1.797	0.502	1.275	0.140	3	46.66
	1 X 3	1.838	0.510	1.30	0.191	3	63.66
	1 X 3	1.917	0.523	1.35	0.310	3	103.33
9	1 X 2	1.642	0.460	1.18	0.023	2	11.5
	1 X 2	1.657	0.462	1.19	0.028	2	14
	1 X 2	1.669	0.464	1.20	0.032	2	16
	1 X 2	1.705	0.473	1.225	0.049	2	24.5
	1 X 2	1.777	0.506	1.25	0.125	2	62.5
	1 X 2	1.821	0.508	1.275	0.140	2	70
	1 X 2	1.841	0.514	1.30	0.162	2	81
	1 X 2	1.902	0.518	1.35	0.236	2	118
10	1 X 1	1.631	0.441	1.18	0.016	1	16
	1 X 1	1.642	0.449	1.19	0.018	1	18
	1 X 1	1.657	0.452	1.20	0.021	1	21
	1 X 1	1.689	0.459	1.225	0.030	1	30
	1 X 1	1.722	0.466	1.25	0.043	1	43
	1 X 1	1.758	0.472	1.275	0.060	1	60
	1 X 1	1.792	0.479	1.30	0.080	1	80
	1 X 1	1.858	0.490	1.35	0.128	1	128

The experiments were conducted for different electroplated porous nickel cathode areas varying from 1 to 10 cm^2 with respect to constant large platinum anode area of 356 cm^2. The effect of anodic over-potential is kept minimal by taking large stable platinum mesh anode. The large platinum anode area compared to small electroplated cathode area implies low anodic over-voltage (V_{ac}), so that the impact of cathodic over-voltage (V_{cc}) could be studied. Therefore small electroplated cathode area

compared to large areas has been specifically taken to study the cathode characteristics.

Current density variations are plotted against the different cathode sizes so that the performance of the cathode could be analyzed as shown in **Fig. 14**.

Graphical analysis of the experiments conducted keeping a constant set of cathode-electrolyte interface over-potentials (V_{cc}) with different cathode areas with respect to a large platinum mesh anode, showed that current density reaches a minimum value. The current density is also found to have a minimum value for particular constant cathode-electrolyte over-potential (V_{cc}) at different cathode areas.

The variation of current density with respect to dynamic cathodic over-potential between cathode and electrolytic interface with constant anode voltages as illustrated in the **Fig. 15**.

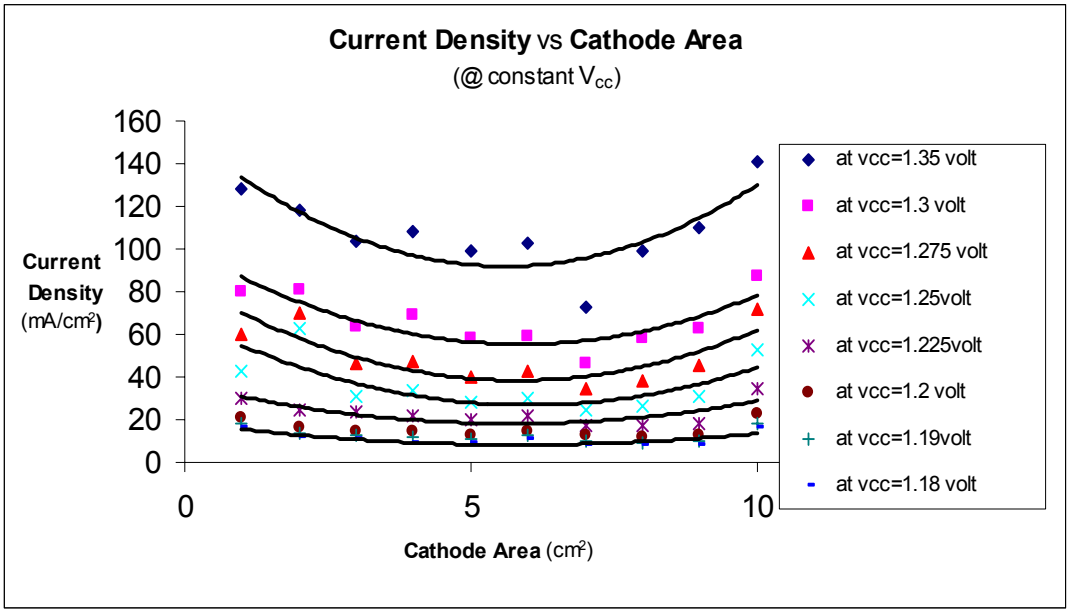

Fig. 14. Plot of the current density versus the area of the DC pulsed electroplated cathodes.

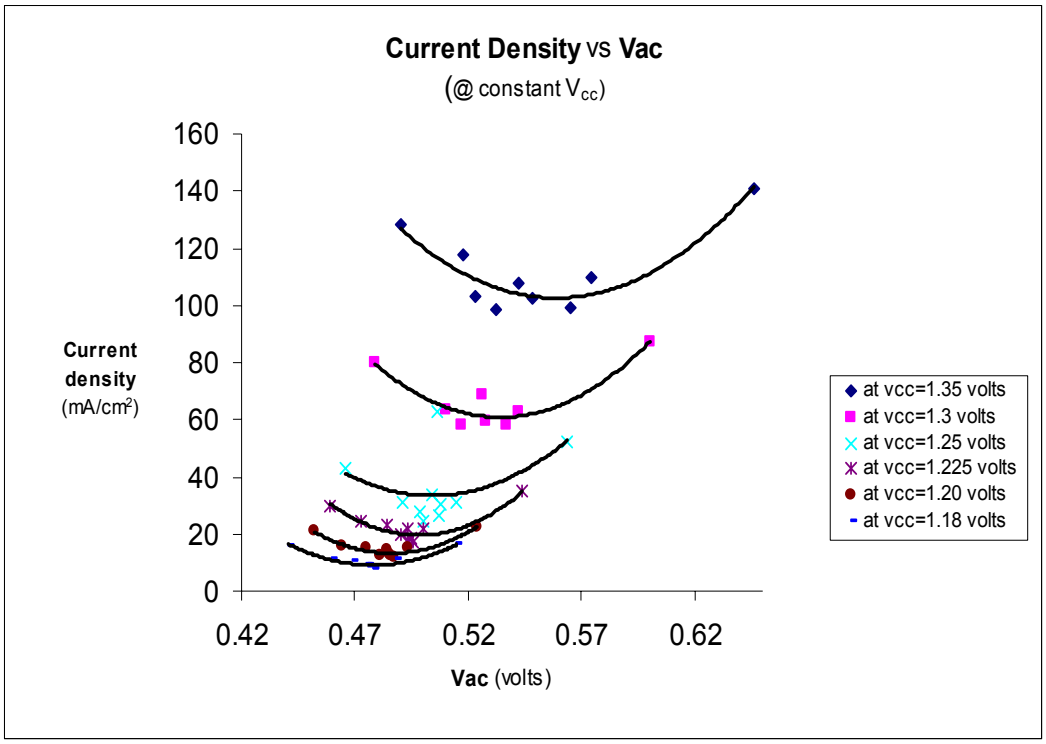

Fig. 15. Plot of current density with the voltage of the cathode (V_{ac}) with reference to saturated calomel electrode when the voltage at the anode with reference to saturated calomel as constant.

The current density and anodic over-potential (V_{ac}) were measured for different cathode areas keeping cathodic over-potential (V_{cc}) constant. The plot indicates that a minimum current density exists for different cathode areas measured at constant cathodic over-potential (V_{cc}). The minimum current densities for different cathode areas at constant V_{cc} were determined from the analysis of data from **Fig. 15**. The data obtained from the analysis were tabulated and presented as **Table 7**. The table shows the small variations in anodic over-potential (V_{ac}) of the large anode with respect to minimum current densities for fixed cathodic over-potentials (V_{cc}).

Table 7. The table shows the values of current density and minimum anodic over-potential (V_{ac}) at each constant set of cathodic over-potentials (V_{cc})

Sr. No	Constant V_{cc} (V)	Variable V_{ac} (V)	Minimum Current Density (mA/cm^2)
1	1.35	0.565	99.50
2	1.3	0.528	59.33
3	1.275	0.517	43.16
4	1.25	0.504	34.00
5	1.225	0.490	19.60
6	1.2	0.485	13.11
7	1.19	0.478	10.60
8	1.18	0.475	9.200

The variations of the current density and the minimum anodic over-potential (V_{ac}) for each set of constant cathodic over-potential values are plotted as shown in **Fig. 16 (a)** from **Table 7**.

Fig. 16 (b) is drawn from the minimum current density values determined from **Fig. 15** and data tabulated in **Table 7**. The main purpose of developing porous electrodes is to have minimum over-potentials so that a large current density is obtained for small sized electrodes.

From the above graphical analysis, it has been observed that the current density increases when the anodic over-potential (V_{ac}) is less as well as more around a central minimum for constant cathodic over-potential (V_{cc}). It is common knowledge that current density increases with an increase in anodic over-potential (V_{ac}) due to the fact that applied voltage is increased.

Fig. 16 (a) indicates anodic over-potential (V_{ac}) varies linearly with cathodic over-potential (V_{cc}). This implies that the increase in the anodic over-potential (V_{ac}), increases cathodic over-potential (V_{cc}), resulting in increased energy losses.

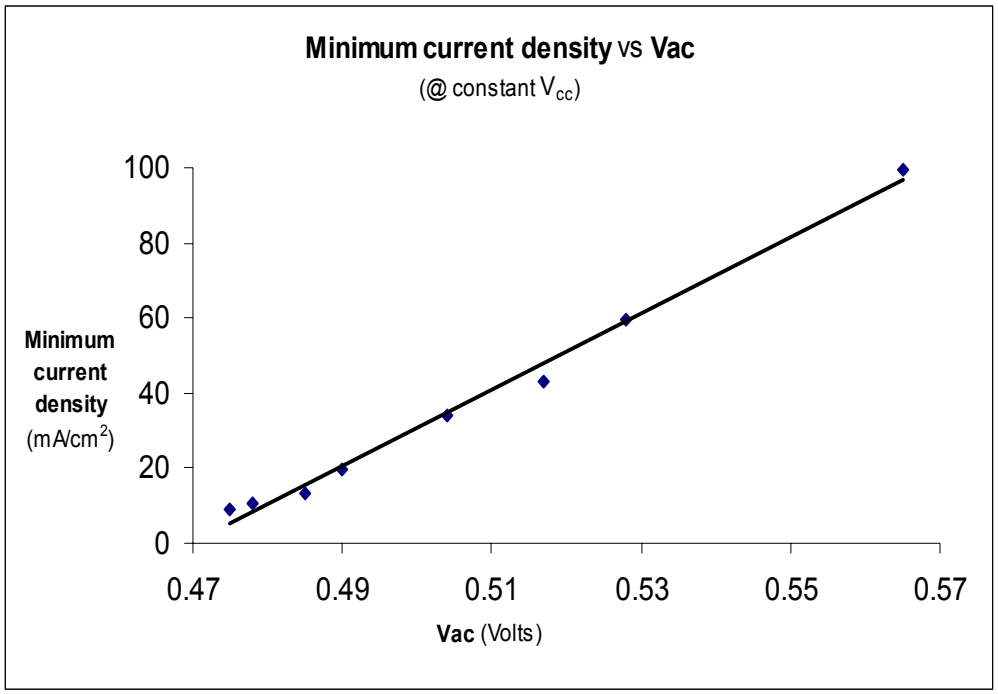

Fig. 16 (a). Plot of minimum current density versus anodic over-potential (V_{ac}) for a set of constant cathodic over-potentials as tabulated in **Table 7**.

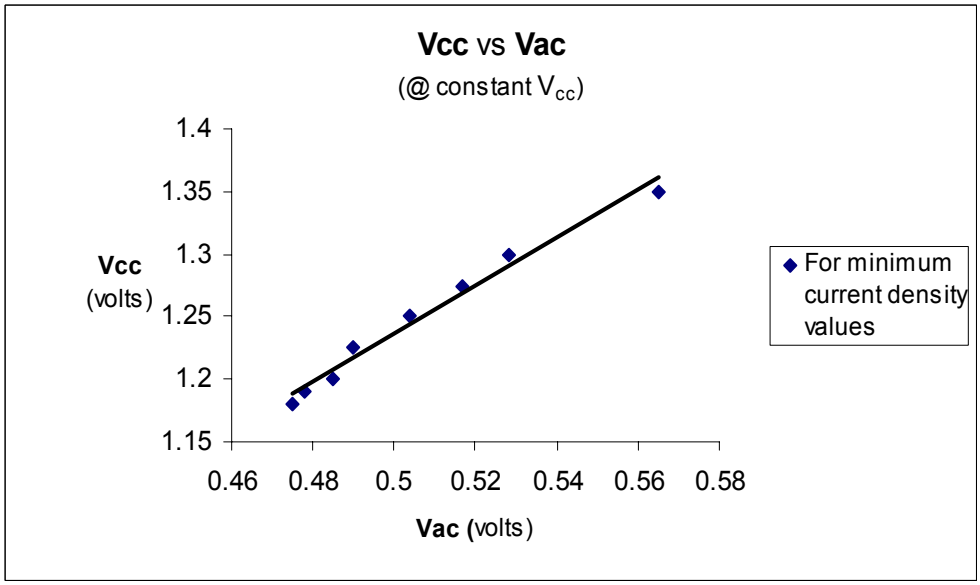

Fig 16 (b). Plot of dynamic cathodic over-potential (V_{cc}) versus anodic over-potential (V_{ac}) for a set of constant cathodic over-potentials as tabulated in **Table 7**.

Fig. 16 (b) indicates that for minimum current densities there exists a V_{ac} corresponding to a specific V_{cc} and the photoelectrochemical cells need to be operated below this value.

Current density has been found to be larger at lower V_{ac} values at constant V_{cc} values for small cathodic electrodes. Therefore it is preferable to operate the photoelectrochemical cell at lower anodic over-potential (V_{ac}) regions

6.3. Summary:

The DC power supply based electroplated porous nickel electrodes prepared during the previous work at the laboratory showed poor adherence to the nickel substrate. Therefore pulsed DC power has been used to produce porous electrodes for photoelectrochemical cells. After a series of experiments run on pulsed DC power for applied frequencies varying from 5 KHz to 200 KHz, optimization of electroplated samples was done on the basis of adhesion, current density, and reproducibility of results. Optimum electroplated electrodes were obtained at 20 kHz pulsed DC frequency, while higher frequencies produce poorly electrodeposited samples. Also a lowest cathodic over-potential of 88 mV was obtained.

The pulsed DC electroplated porous nickel electrodes are preferred to be used as cathodes due to the fact that their adherence to the nickel substrate is strong and there is no possibility of degradation due to anodic dissolution. Therefore the measurements are made using these fabricated porous electrodes as cathodes for substrate-type solar cells in the photoelectrochemical hydrogen generation.

Detailed experiments were focused on: (i) the effect of area at a constant set of applied voltages at 1.8, 1.9 and 2.0 V, (ii) effect of dynamic cathodic over-potential (V_{cc}) at constant dynamic anodic over-potential (V_{ca}), (iii) effect of anodic over-potential (V_{ac}) at constant dynamic cathodic over-potential (V_{cc}). These experiments were done for small area (1 to 10 cm^2 and 5 to 50 cm^2) porous electroplated cathodes with respect to large area platinum mesh anodes of area 356 cm^2.

The data and graphical analyses suggest that the current density increases with a decrease in the size of the cathode (area) for the same set of applied voltages. This may be attributed to the current distribution and potential drop across the porous electrode. The larger the length of passage of electrons in the electrode, the larger the potential drop and lower will be the current density. Increased current density increases the potential between cathode-electrolyte interface (V_{cc}) potential. Increased V_{cc} means increase in energy losses at the interface of cathode and electrolyte in the photoelectrochemical cell.

It has been observed that as the current density decreases there is an increase in the potential between anode-electrolyte interface (V_{ac}) when the total applied voltage is kept constant. This implies an increase in the cathode size (area). An increase in the V_{ac} means increased energy losses at the anode. In a photoelectrochemical cell, V_{ac} is more predominant compared to V_{cc}. The standard anodic over-potential, under zero ionic current conditions, lies in the range of 180 to 250 mV, while standard cathodic over-potential lies in the range of 70 to 150 mV which could be measured from Tafel plots. The dynamic over-potentials are under applied voltage with a three electrode configuration with saturated calomel electrode as the third electrode. These dynamic

over-potentials are higher than the standard electrode potentials and their values increase with an increase in the applied voltage.

A similar trend has been observed for experiments conducted in a configuration in which a constant set of anode-electrolyte voltages (V_{ac}), that is (i) current density increases with a decrease in the size of the porous electroplated cathode, and (ii) current density increases with an increase in cathode-electrolyte interface potential (V_{cc}).

A set of experiments conducted while keeping a constant set of cathode-electrolyte interface over-potentials (V_{cc}) with different cathode areas with respect to large platinum mesh anode, showed that the current density reaches a minimum value. Current density is also found to have a minimum value for a constant cathode-electrolyte over-potential (V_{cc}) at different cathode areas. These minima for different sets of constant V_{cc} were plotted against V_{ac}, this behavior was found to be linear. This indicates that for the chosen set of anode and cathode, there is a specific value of V_{ac} for the given V_{cc}. Also the plot drawn for minimum current density versus variable V_{ac} shows linear behavior. The increase current density was observed on both sides of the minima. The increase in current density after the minima with the increase in V_{ac}, at constant V_{cc} implies more energy losses at the electrode interface.

Therefore, it is preferable to operate the photoelectrochemical cell at lower values of V_{ac}, at which the current density has been found to increase for a particular set of V_{cc} values. This region represents smaller cathode sizes with respect to very large anodic surface areas. Therefore, it is more important to choose very large anodic surface areas to keep minimal voltage losses.

The use of porous catalysts as a cathode enables the operation of the electrolyzer in the range of 1.75 to 1.9 V in a triple-junction amorphous silicon based photoelectrochemical cell for efficient generation of solar hydrogen.

Task 3: Development of Advanced Materials for Immersion-type PEC Cells.

Iron (III) Oxide Films

Abstract:

This project focuses on using indium and iron oxide to make a protective thin film for amorphous silicon based solar cells. From the work completed, the results indicate that samples should be made at 228°C, with 30 W of indium and 100 W of iron oxide, and a sputter deposition time of two hours. At 0.6 V, the best sample displays a maximum photocurrent density of 50 μA/cm^2. Subsequently, an X-ray diffraction scan confirmed that it is indeed indium and iron oxide that is being produced.

Experiment:

As mentioned before, the object of this project was to produce an optimal, protective, thin film made of indium and iron oxide for amorphous silicon. These thin films were created using rf (radio frequency) sputter deposition. Two 2" sputter guns were used with respective targets of indium and iron oxide. The two main variables that were considered were the temperature of the depositions as well as the sputter powers of indium used. Samples were made at deposition temperatures of 200, 228, 250, and 275 °C. Furthermore, samples using 20, 25, 30, 35 and 40 W of indium were generated at each of these respective deposition temperatures. In general, non-varied deposition conditions of 100 W of iron oxide, 8 sccm of argon gas, 2.67 sccm of argon/oxygen gas, and a pressure of 6.0 mTorr were maintained.

After samples were generated, cyclic voltammetry tests were then run to test for stability. A standard run consisted of placing a sample in a three electrode cell with a

5.9M KOH solution serving as the electrolyte. Other than our working electrode, there was also a reference electrode (saturated calomel electrode) and a platinum mesh electrode. A potential ranging from -1.0 to 3.0 V (in the dark) was applied across the sample and its resulting current density was measured using a Voltalab PGZ301 Dynamic machine paired with VoltaMaster 4 software. This was done nine times per sample. In addition, the samples were also tested for their photocurrent ability using a xenon/mercury lamp that was paired with an Ignitor Movement by Oriel Instruments model 66900 series 126. However, for this test, a potential only ranging from -0.5 to 1.0 V was applied across the sample. And then the lamp was alternately directed on and off the sample at intervals of 5 s.

Film thickness was also measured for a select group of samples using a surface profiler (Dektak) and an interference method as run by a UV/VIS/NIR – Cary 5 Diode Array (HP8452A).

Last, X-ray diffraction was run on the sample that had the highest photocurrent density (ST 686). X-ray diffraction (XRD) spectra was collected on an X-ray powder difractometer (X'Pert Pro, PANalytical), which was connected to a Dell Optiplex PC with X'Pert Data Collector software. The scans were collected using a glazing angle of 25 to 75° (2θ) and copper Kα radiation with a wavelength of 0.15405 nm. Scans were analyzed using X'Pert High Score Plus software (PANalytical) and the results were matched against the International Center for Diffraction Data (ICDD) database.

Results:

In general, at each respective temperature of deposition, as the power of indium was increased, each respective sample's photocurrent density also increased. However, eventually the films became too thick and the charges recombined and the photocurrent would then decline.

From the array of preliminary samples, the sample (ST671) created at 228°C with 30 W of indium had the highest photocurrent density (**Figure 1**, middle line) (30 to 40 μA/cm^2.) Thus, two more samples were produced at the conditions of the preliminary, best sample to test for reproducibility and photoactivity. The first reproduction (ST686) had an even higher level of photocurrent than the first sample made at the best conditions. It is represented by **Figure 1** (top line) and its photocurrent density was approximately 50 μA/cm^2. Unfortunately, the third copy of the sample made at the best conditions had a very disappointing photocurrent of approximately 5 μA/cm^2 as represented by **Figure 1**, bottom line.

This abrupt change in the resulting photocurrent may have been due to the fact that this second reproduction was created using a new indium target, because the previous target had melted. Hence, the new indium target may have needed some seasoning before being able to generate a constant and relatively uniform plasma. Using the new indium target to reproduce another sample at the best conditions may be considered for future work.

The best sample (ST 686) was also tested for stability. In this regard, not only did it have the highest photocurrent, it also had the highest current density. It was the only sample that had current densities on the milliamp scale. However, stability-wise, the sample did not hold up so well. It became increasingly unstable over time. Thus,

bringing up the question of whether higher current density comes at the cost of a loss in stability. **Figure 2** shows ST 686's stability curves.

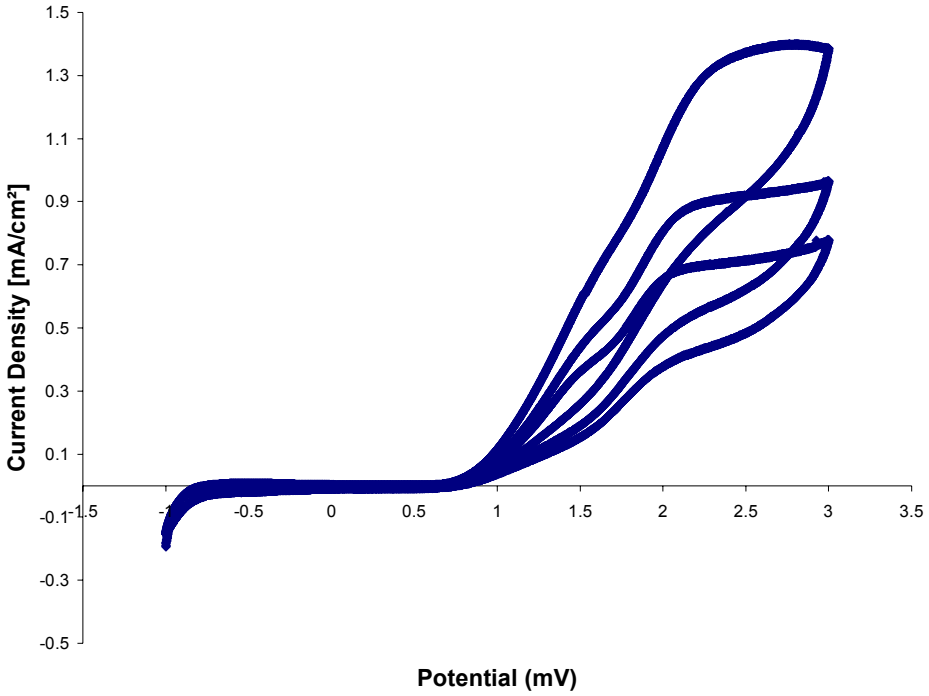

Figure 1. Graph displays photocurrent of all samples that were made at the best conditions of: 228°C, 30 W of indium, 100 W of iron oxide, 2 hour sputter deposition period.

The sample with the best photocurrent density (ST 686) was also run through an X-ray diffraction scan (**Figure 3**) to determine what kinds of compounds were actually being produced. Compared with the previous best sample (ST 191), ST 686 displays a greater intensity of indium iron oxide versus iron oxide peaks.

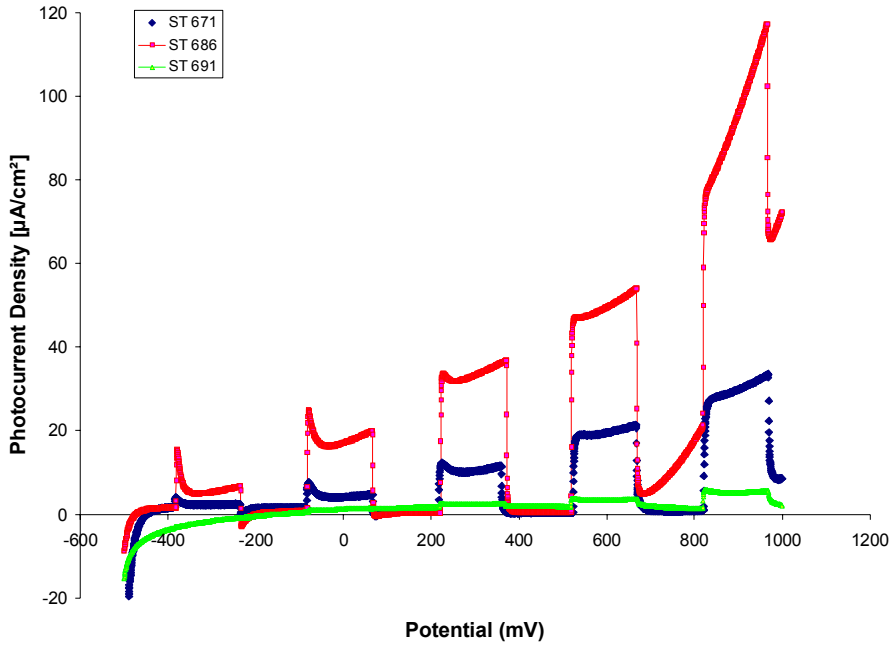

Figure 2. Stability curves for the best sample, ST 686. It was the only sample that had current densities on the milliamp scale. However, it can be noted that perhaps higher current density comes with a loss in stability as depicted by the drop in current density with each successive scan.

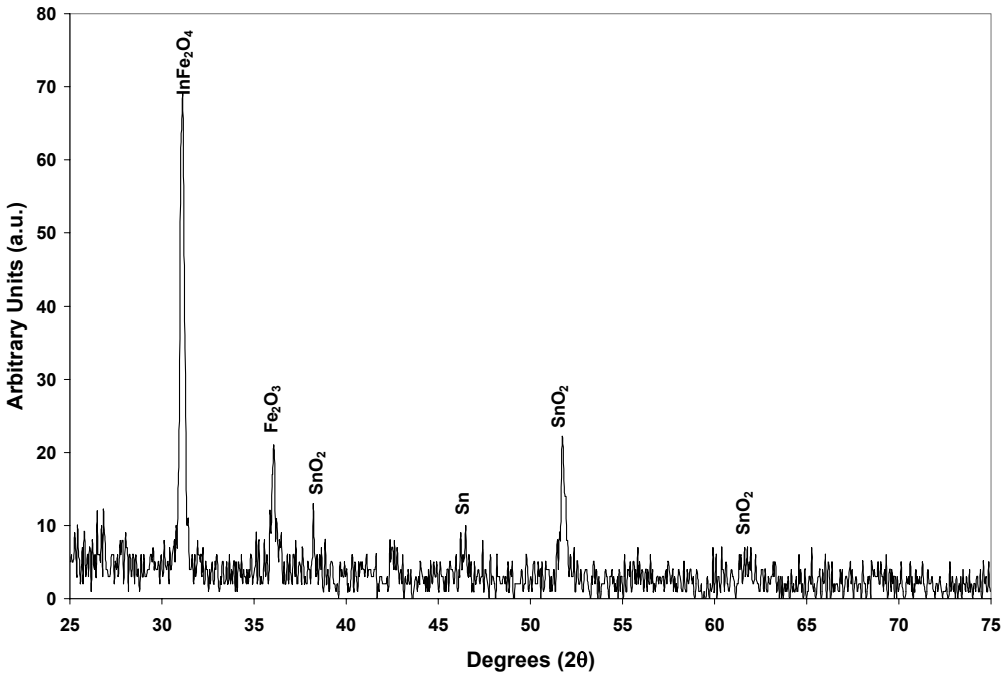

Figure 3. X-ray diffraction of ST686, the most photoactive sample.

In addition to testing the reproducibility and photoactivity of samples made at the best conditions, samples were also made at the best conditions where the normal sputter deposition time of 2 hours was varied by ±30 minutes in order to test for optimal film thickness. The sample made with a sputter deposition time of 90 min (ST 687) had a photocurrent that was within the same vicinity of that as the original sample (ST671) that was made at the best conditions. It is represented by the second curve down in **Figure 3**. However the sample made with a sputter deposition time of 150 min (ST688), represented by the lowest curve in **Figure 3**, and had a photocurrent that was approximately 5μA/cm^2.

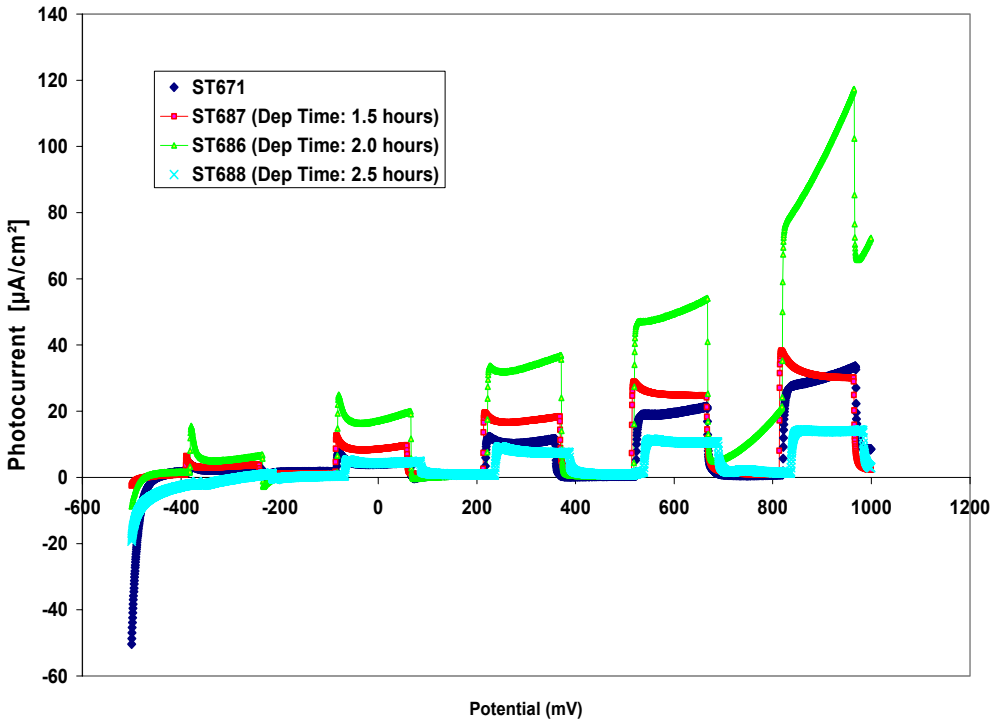

Figure 3. Samples made at best conditions of 228°C with 30 W of indium and 100 W of iron oxide. The graph shows the relationship between photocurrent and film thickness.

Based on these results, it is believed that the current film thickness that is generated by a 2 hour long sputter deposition period is relatively optimal, because the second sample made at the best conditions (ST686), had a photocurrent density within the 50 μA/cm^2 range as represented by the top curve in **Fig. 3**. It is also believed that the sample that only underwent 90 min of sputter deposition was too thin. Thus there was not enough band-bending to allow good electron flow. Whereas the sample that had 150 min of sputter deposition time was too thick and thus electrons did not have enough energy to reach the surface and instead dropped back down to the ground state halfway through the band.

Another interesting observation about film thickness was the discrepancies between thickness measurements that were obtained using Dektak as opposed to using UV-Vis. Generally, the measurements obtained using UV-Vis were very similar to the measurements obtained using Dektak **(Fig. 4).** However, the majority of the UV-Vis measurements were slightly higher than the Dektak measurements. Presently, without further analysis, the implications of this trend remain ambiguous.

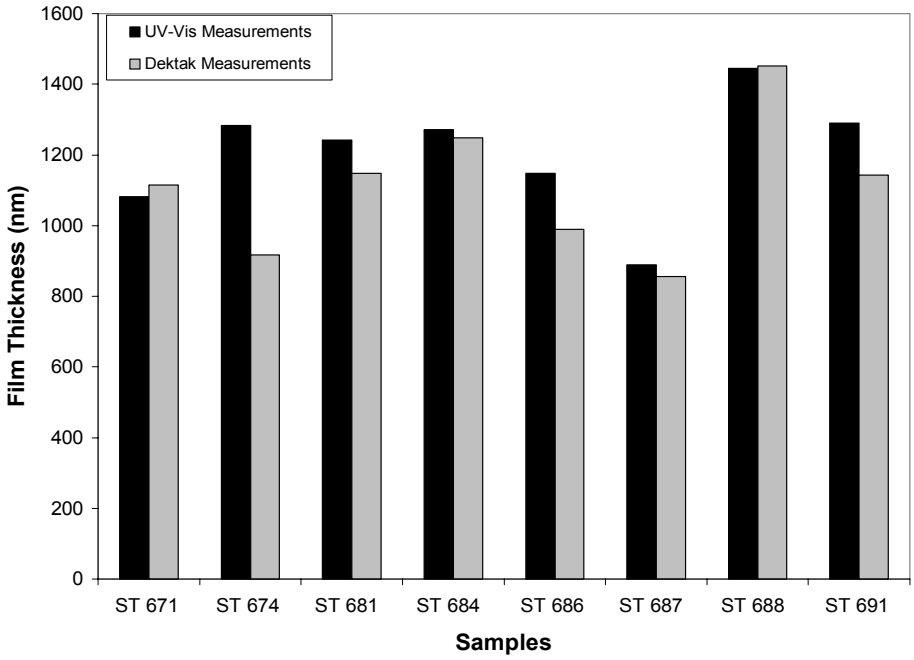

Figure 4. Dektak vs. UV-Vis measurements for film thickness measurements.

Last, the data obtained from the UV-Vis scans (**Fig. 5**) allowed for film thickness to be calculated.

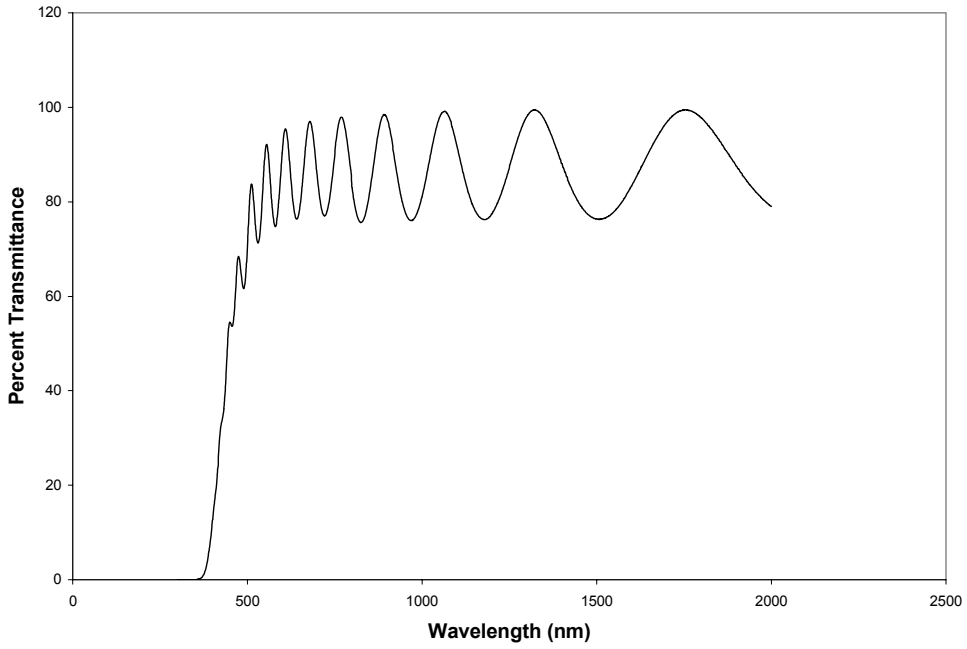

Figure 5. Visible/NIR spectrum of sample ST686 created at 228 ºC, 30 W indium and 100 W iron oxide.

Conclusion:

The best sample (ST686) was created at 228 °C with 100 W of iron oxide and 30 W of indium. Not only did it have the highest current density, it also had the highest photoactivity. However, it was relatively unstable, which might be a problem if it is mounted on a solar cell for an extended period of time. Thus, the stability and reproducibility of samples created at these best conditions may be considered for future evaluation. Taking the best sample created at these deposition conditions and placing it on a solar cell for follow-up purposes may also be another avenue of study.

Tables of Samples Studied Grouped by Oxygen Concentrations in the Chamber Atmosphere During Deposition Process.

10% Oxygen

	150ºC	**200ºC**	**250ºC**
5 Watts Indium			
10 Watts Indium			
15 Watts Indium		ST200	ST232
20 Watts Indium			

6% Oxygen

	150ºC	**200ºC**	**250ºC**
5 Watts Indium			
10 Watts Indium		ST221	ST220
15 Watts Indium			
20 Watts Indium			

5% Oxygen

	150ºC	**200ºC**	**228ºC**	**250ºC**	**279ºC**	**306ºC**
5 Watts Indium		*ST188*				
10 Watts Indium	*ST209*	*ST186*		*ST193*		
15 Watts Indium	*ST208*	*ST189*				
20 Watts Indium		*ST191* **ST677**	**ST668**		**ST669**	**ST676**
25 Watts Indium		**ST683**	**ST670**	**ST679*** **ST680**	**ST673**	
30 Watts Indium		**ST684**	**ST671, ST678* ST686 ST687** ST688** ST691*****	**ST681**	**ST674**	
35 Watts Indium		**ST685, ST690*****	**ST672**	**ST682**	**ST675**	
40 Watts Indium			ST689			

4% Oxygen

	150ºC	200ºC	250ºC
5 Watts Indium			
10 Watts Indium		ST234	ST216
15 Watts Indium			
20 Watts Indium			

3% Oxygen

	200ºC	250ºC	300ºC
5 Watts Indium			
10 Watts Indium		ST225	
15 Watts Indium			
20 Watts Indium			

2% Oxygen

	200ºC	250ºC	300ºC
5 Watts Indium			
10 Watts Indium			
15 Watts Indium		ST203	
20 Watts Indium			

1% Oxygen

	200ºC	250ºC	300ºC
5 Watts Indium			
10 Watts Indium			
15 Watts Indium	ST198		
20 Watts Indium			

Without Oxygen

	150ºC	200ºC	250ºC
5 Watts Indium		ST169	ST135
10 Watts Indium		ST157/ST147	ST130
15 Watts Indium		ST150	ST140
20 Watts Indium		ST160	ST155

Fluorine-Doped Tin Oxide Films

Past work on fluorine-doped tin oxide (F-SnO_2) films involved deposition by spray pyrolysis. F-SnO_2 deposited by rf sputtering has recently been investigated. Preliminary testing has found rf sputtered F-SnO_2 to be unstable in 5.9 M KOH, and the conductivity of the films is low. However, transparency is near 90 % and there is evidence of significant photocurrent response.

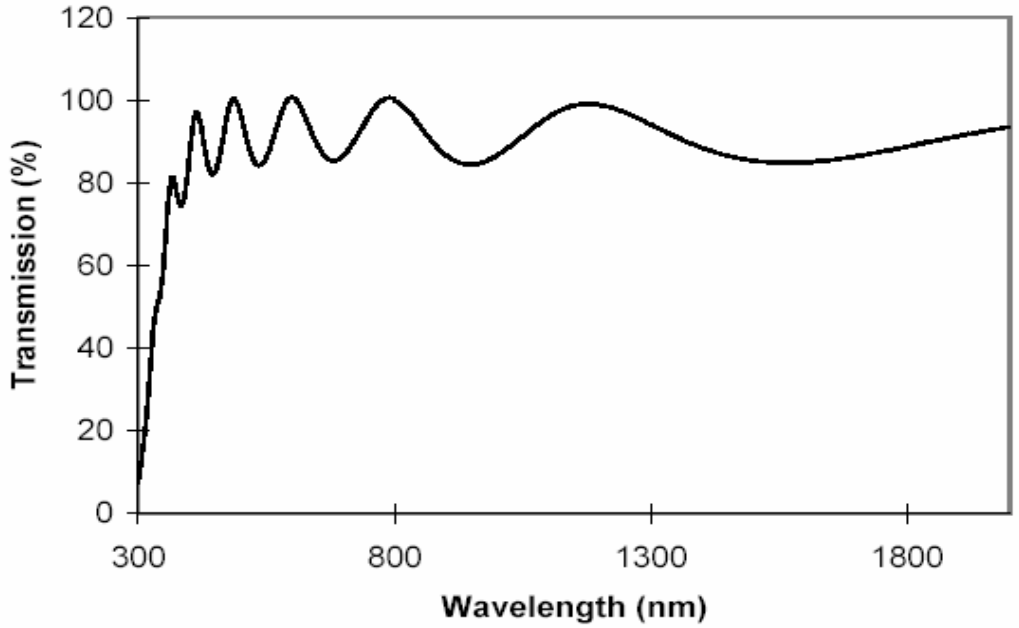

Figure 6. UV-vis transmission spectra for F-SnO_2 thin film deposited at 50 W for 135 min at 250 °C. The film transparency was found to be near 90% in the visible portion of the spectrum, and a band gap of 3.38 was determined from tauc plot calculations.

Research on sputtered F-SnO_2 has been put on hold because the fluorine in the target contributed to a reaction with the stainless steel components of the sputter gun, bonding the target to the cathode cap. Upon removal, the target shattered. Methods of sputtering F-SnO_2 without damaging the sputter chamber are being investigated.

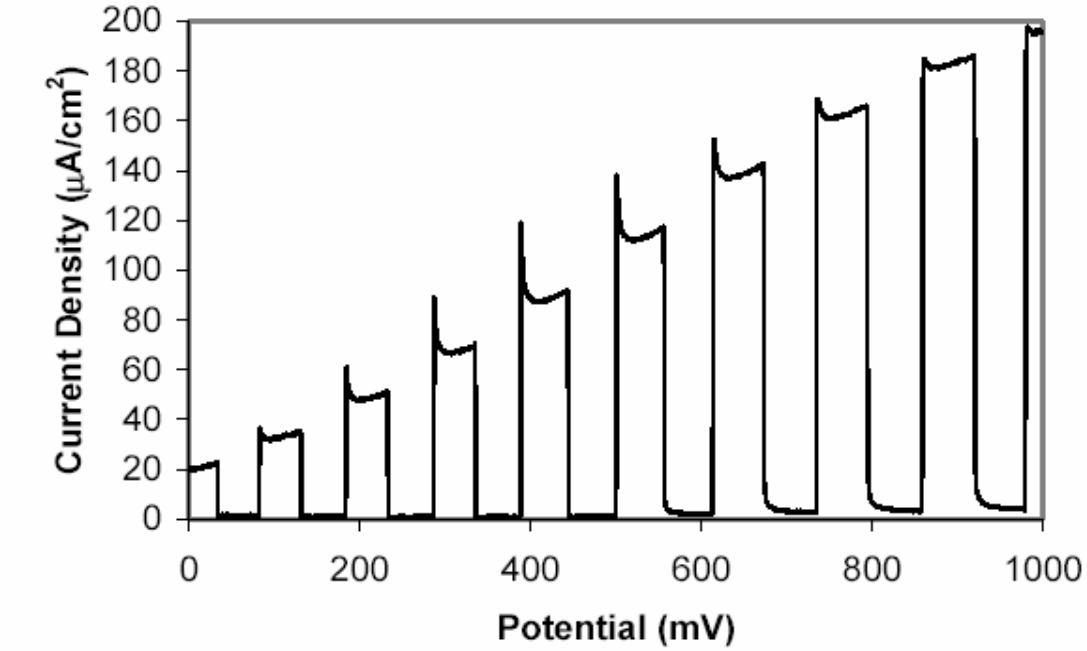

Figure 7. Chopped scan of F-SnO_2 thin film. A photocurrent of ~ 0.2 mA/cm^2 was observed under 0.56 sun illumination.

Figure 8. Picture of the shattered SnO_2/SnF_2 target used for sputter deposition of the F-SnO_2 thin films.

Tin Oxide (Antimony-doped and Fluorine-doped)

Tin oxide films were deposited at a temperature lower than 250°C to be used as a transparent conducting corrosion resistant (TCCR) layer on the amorphous silicon devices. Tin oxide films were deposited on various substrate materials, including Tec15, glass, and amorphous silicon devices. They were tested in an electrolysis cell and appeared to be resist corrosion by the electrolyte solution. Yet, the main problem encountered is the quick delamination around the edges of the tested samples. To overcome this problem, a protective sealant was applied along the edges to cover the TCCR /Tec15 interface. This solution was helped elongate the testing period; however after several months of continuous electrolysis the interface of the TCCR/sealant interface showed delamination.

Looking for a more permanent solution, the use of sol gel method to apply a resistive coating along the edges was investigated. A thin film of zirconium oxide can be deposited on the edges using a solution of zirconium n-propoxide, propanol, and acetylacetone. The mixture was applied on the edges using a fine paint brush and annealed at 250 – 400°C in air. In another attempt, a solution of zirconium propoxide dissolved in propanol and trichloroacetic acid was applied, and the samples were annealed at 250 - 400°C in air. Preliminary testing showed the coatings to be very porous. To overcome, such a problem, the samples usually are annealed at higher temperatures to densify the deposited layer. Yet, higher temperatures are not favored in this case, as these coatings are to be applied on amorphous silicon devices. Annealing

the samples in other atmospheres than air might be a solution to overcome the porosity of the samples.

Meanwhile, the use of an o-ring seal to seal the area where the electrolysis testing is taking place appears to be efficient. Thus, long term testing of the deposited TCCR layer on amorphous silicon device is being processed, in electrolysis cell using 5.9M KOH as our electrolyte.

Furthermore, the sol gel method will be investigated farther, to coat the TCCR – Tec15 interface at a low temperature to be then applied on the coated amorphous silicon devices.

Ruthenium oxide films have been deposited by different means and tested for the electrocatalytic oxidation of water. Ruthenium oxide was successfully deposited electrochemically and by thermal decomposition and tested in an electrolysis cell. The voltage needed to reach the desired current density was lower when ruthenium oxide was present. For example, the voltage needed to oxidize water on a fluorine doped tin oxide thin film is about 4.5 V at a current density of 8 mA/cm^2, yet the voltage needed to reach the same current density when ruthenium oxide was present is 2.7 V.

Figure 9. O-ring seal for electrolysis testing of tin oxide and ruthenium oxide films.

Work has progressed on developing an oxidation catalyst for the anode of an immersed PEC device of lower cost than ruthenium oxide. A catalyst consisting of a mixture of manganese oxide and ruthenium oxide (20 to 50 % Mn) provided a catalyst layer more stable than pure ruthenium oxide with a slight lowering of the voltage needed to reach the required current density (2.1 V versus 2.7 V to maintain 8 mA/cm^2). A similar lowering of potential was observed for coatings on stainless steel mesh, which measured 1.2 - 1.3 V compared to 1.7 - 1.9V for stainless steel alone. Our interest in manganese oxide is due to cost considerations: manganese oxide costs $100/1 kg while ruthenium oxide costs $100/4 g in the Aldrich Chemical Company catalog.

Work was also put into studying the addition of cobalt oxide to the ruthenium oxide and manganese oxide mixture to be used as a coating on the anode of PEC devices. Incorporating cobalt oxide and manganese oxide would lower the price of the catalyst layer due to the very large difference in price between the ruthenium oxide precursors and the manganese oxide and cobalt oxide precursors.

A sample of a solid mix of MnO, RuO_2, Co_2O_3 deposited on Tec15 glass ran for 3 days and it needed 2.9 V to reach 0.008mA/cm^2 compared to 2.3 - 2.7 V range needed to reach the same current density with the RuO_2, or MnO-RuO_2. These results are preliminary and more work needs to be done in order to conclude whether there are advantages to incorporating cobalt oxide in the catalyst layer. An observation about MnO-RuO_2-Co_2O_3 was that no coloration of the electrolyte solution occurred during running the electrolysis cell. Further studies of samples of RuO_2-Co_2O_3, MnO-Co_2O_3 mixes are to be studied for their behavior as an oxidation catalyst.

A protective layer on the photovoltaic device is required for the PV hydrogen system, particularly for applications where the photovoltaic device is immersed in the electrolyte solution. Previous work has shown the F doped tin oxide (SnO_2:F) to be a good candidate as a transparent conductive corrosion resistant layer (TCCR). In the process of testing different metal oxide thin films as a TCCR layer, SnO_2:F thin films were deposited on stainless steel and on Tec 15 (commercially available highly conductive SnO_2:F) at a low temperature between 200°C and 250°C by spray pyrolysis; this temperature range does not damage the triple junction silicon solar cell during the preparation of the PV hydrogen system.

When connected as an anode in the electrolysis cell, the low temp SnO_2:F thin films lasted for up to three months while maintaining a current density of 0.008 A/cm^2, using 3.5 V for coated Tec15 and around 2.2 V for those deposited on stainless steel. Samples coated with an undoped tin oxide thin film failed to last for even a few hours under the same conditions in a highly concentrated KOH electrolyte solution. The

undoped tin oxide films tested were deposited by spray pyrolysis on both glass and stainless steel substrate, and by sputtering on stainless steel substrates.

Conceivably, the doping in the tin oxide lattice is helping in forming a more chemically resistant protective layer. Spray pyrolysis deposition technology is a versatile method that provides a simpler way experimenting with different metal oxide thin films, in this case doping the tin oxide thin films. We needed to deposit a test doped tin oxide that can be later on deposited using sputtering, a deposition technique that can more easily be incorporated into the fabrication of triple junction solar cells possessing a TCCR protective coating.

Antimony doped tin oxide (SnO_2:Sb) thin films were deposited on Tec 15, where the solution was prepared from a solution of tin tetrachloride dissolved in a mixture of water and ethanol. Antimony chloride was used as the source of antimony doping. The deposition temperature was around 235°C in a nitrogen atmosphere. The resulting films, which exhibited a sheet resistance of circa 500 ohm, were connected to the electrolysis cell where they lasted for barely a few hours under the same conditions stated previously for the stability tests with SnO_2:F.

In conclusion, the SnO_2:F deposited by spray pyrolysis at temperatures less than 240 °C has proven to be a superior TCCR coating than undoped as well as antimony doped films and superior to ZnO and In_2O_3 based coatings.

Cobalt oxide films

These films were made by reactive sputtering in an oxygen partial pressure of 10 % and 20 % in argon. Previous studies done at UT have shown very good long term stability as the anode in 5.9 M KOH. The XRD studies have confirmed the film is Co_3O_4.

Several metal oxides were alloyed with Co_3O_4 to improve the conductivity of films. Nickel oxide was found to be the best which increases the conductivity keeping the electrochemical stability of Co_3O_4 films.

The downside of Co_3O_4/NiO films is that they are below the accepted level of visible light transmission to be used as a TCCR. Furthermore, the magnetic nature of the Co and Ni make the film deposition rate very low as well as the reproducibility being poor.

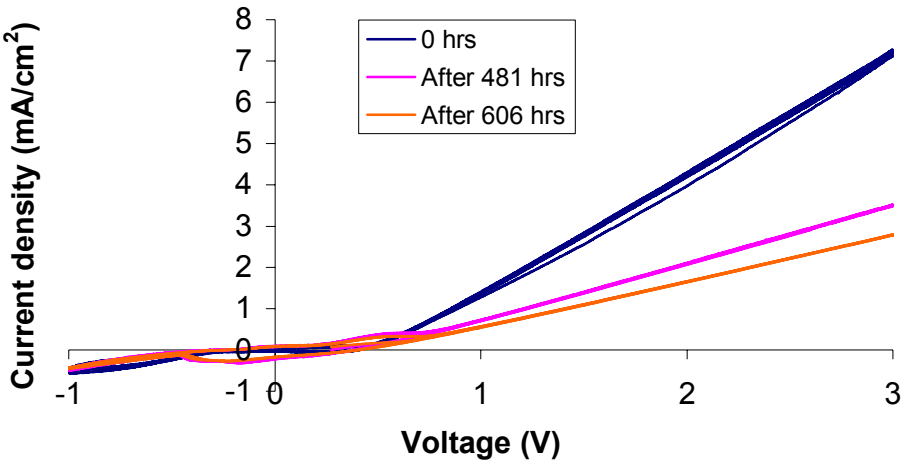

Figure 10. Current density (mA/cm^2) versus voltage (V) for cobalt oxide films at 0, 481, and 606 hours of continuous testing.

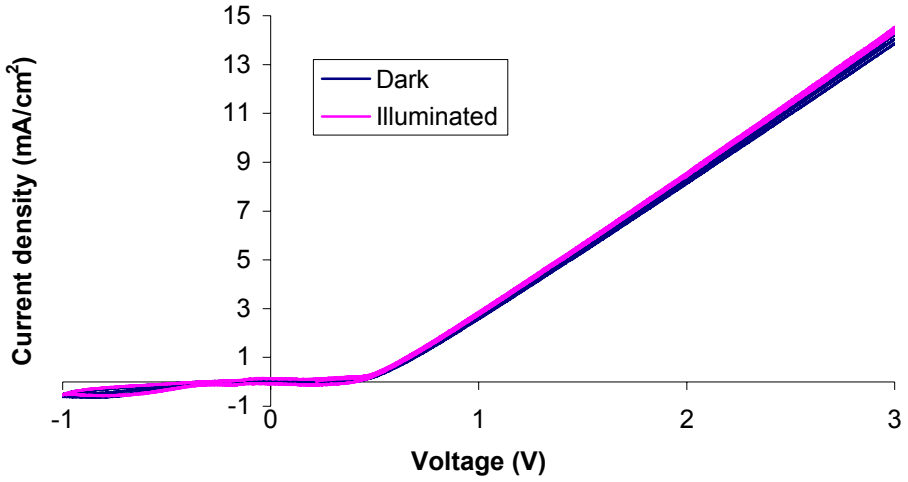

Figure 11. Current density (mA/cm^2) versus voltage (V) for cobalt oxide (Co_3O_4)/nickel oxide (NiO). Dark and light illumination initial results are shown. (Co-sputtered Co:100 W, Ni: 40 W on 20 % O2/Ar).

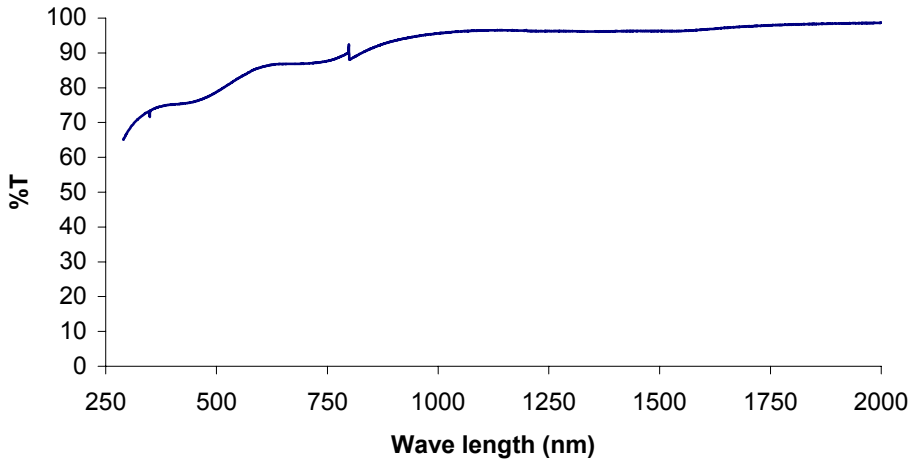

Figure 12. UV-vis plot for cobalt oxide / nickel oxide co-sputtered film.

Titanium Oxide Films

Anatase TiO_2 has been well known as a photocatalyst for many years. The good chemical stability and high optical band gap make it a very good TCCR. But using

existing techniques, anatase TiO_2 cannot be made at low temperature (< 250 °C). However using an appropriate seed layer having the correct lattice parameters we expect to see a growth of polycrystalline anatase TiO_2. According to literature ZrO_2 monoclinic is supposed to act as a good seed layer for growth of anatase TiO_2. A thin film of ZrO_2 is deposited using reactive sputtering of Zr in 20 % O2/Ar gas mixture. TiO_2 film is deposited on the ZrO_2 seed layer. This technique has shown promising results. The optical band gap of ZrO_2 (> 4 eV) minimizes the loss due to photon absorption by the seed layer.

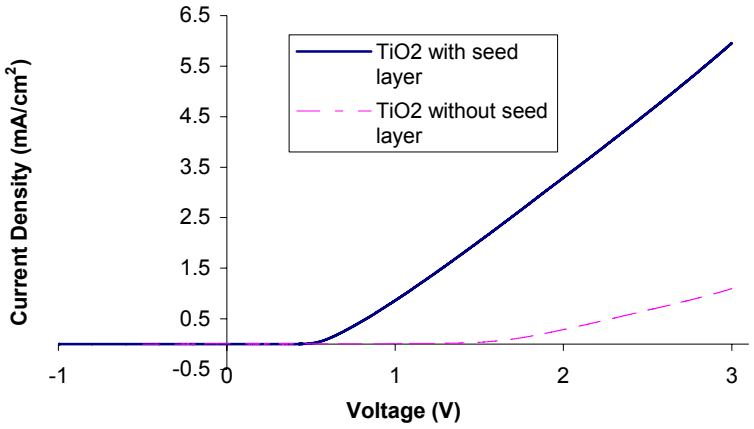

Figure 13. Current density (mA/cm^2) versus voltage (V) of TiO_2 with and without seed layer.

The Raman scattering studies have confirmed the formation of anatase TiO_2 as well as the ZrO_2 monoclinic.

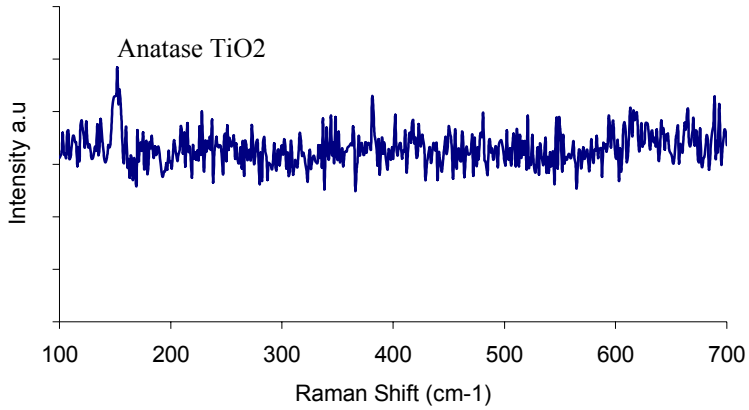

Figure 14. Raman spectroscopy of TiO_2 75 W for 60 min on ZrO_2 50 W at 30 min seed layer.

However the deposition conditions of two layers need to be optimized as they are not fully crystallized.

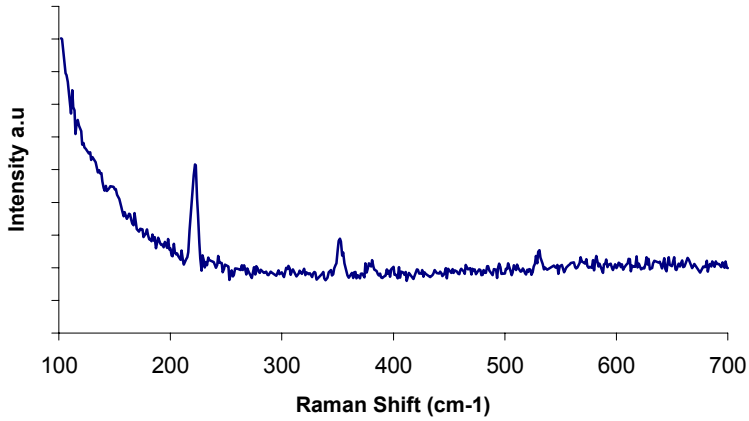

Figure 15. Raman Spectroscopy of ZrO_2 on glass.

Fluorine-doped tin oxide

The PV-Hydrogen system consists of a solar cell placed in electrolyte, where a transparent conductive and corrosion resistant layer (TCCR) is deposited on the solar cell to protect it from corrosion. Besides being a corrosion resistant layer, the TCCR needs to be transparent and conductive. So far tin oxide thin films appear to be corrosion resistant in the basic electrolyte when deposited on the anode side of an a-Si PV-device. The tin oxide thin films were fluorine doped to produce conductive films that can carry the charge to the surface where electrolysis occurs. The films were deposited at a temperature lower than 250 °C by spray pyrolysis, and they had a sheet resistance in the range of 500 and 1.4 kΩ.

The transparency of the TCCR layer is very important; a more transparent TCCR layer will allow more photons to pass through to the photovoltaic materials thus increasing the solar cell efficiency in the PV-hydrogen system.

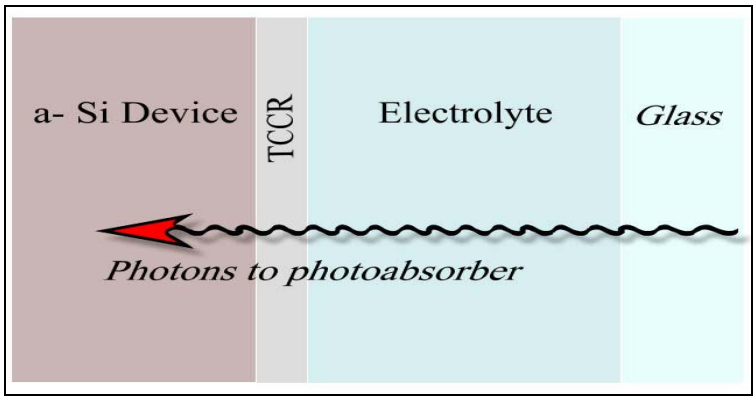

Figure 16. Schematic of photon movement through immersion-type solar cell.

In order to study the transparency of the TCCR layer with respect to visible light, fluorine doped tin oxide thin films were deposited on glass and on TEC15 (commercial fluorine-doped tin oxide glass, Pilkington).

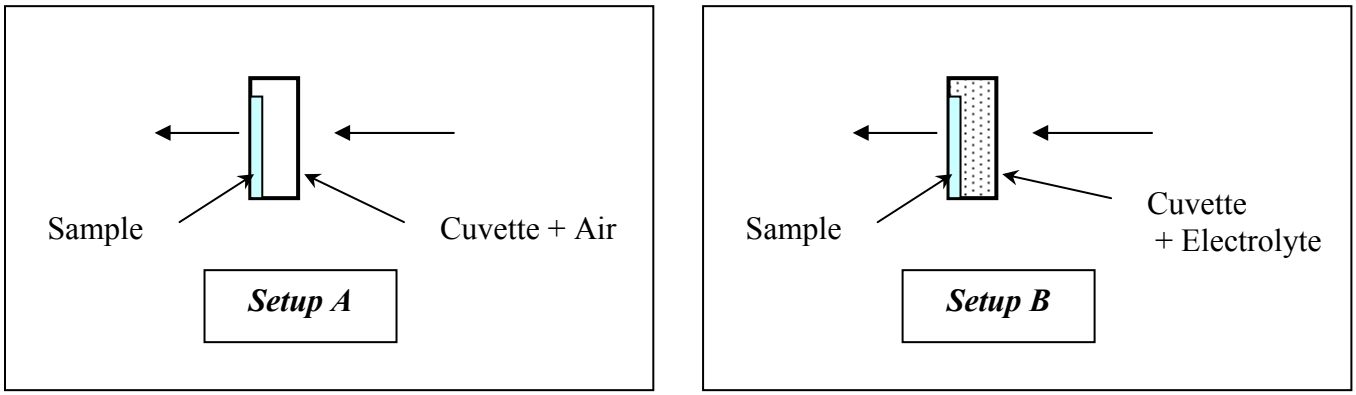

Figure 17. Test set-up for TCCR layers.

The spectra were obtained in two arrangements:

A. Setup A: the samples were placed in a cuvette filled with air

B. Setup B: the samples were placed in a cuvette filled with electrolyte which consists of a 5.9 M KOH aqueous solution.

Setup B attempts to duplicate the setup of the PV-hydrogen system, and should provide an estimate of the amount of light reaching the photoabsorber after passing through the electrolyte and the TCCR layer.

The samples that were studied included tin oxide films sprayed on glass (**glass/TCCR**), tin oxide sprayed on TEC15 (**TEC15/TCCR**), and TEC15. As a result, we can compare the % transmittance spectra of the samples with a TCCR/air interface to those with a TCCR/electrolyte interface, as shown in **Figures 18 and 19**.

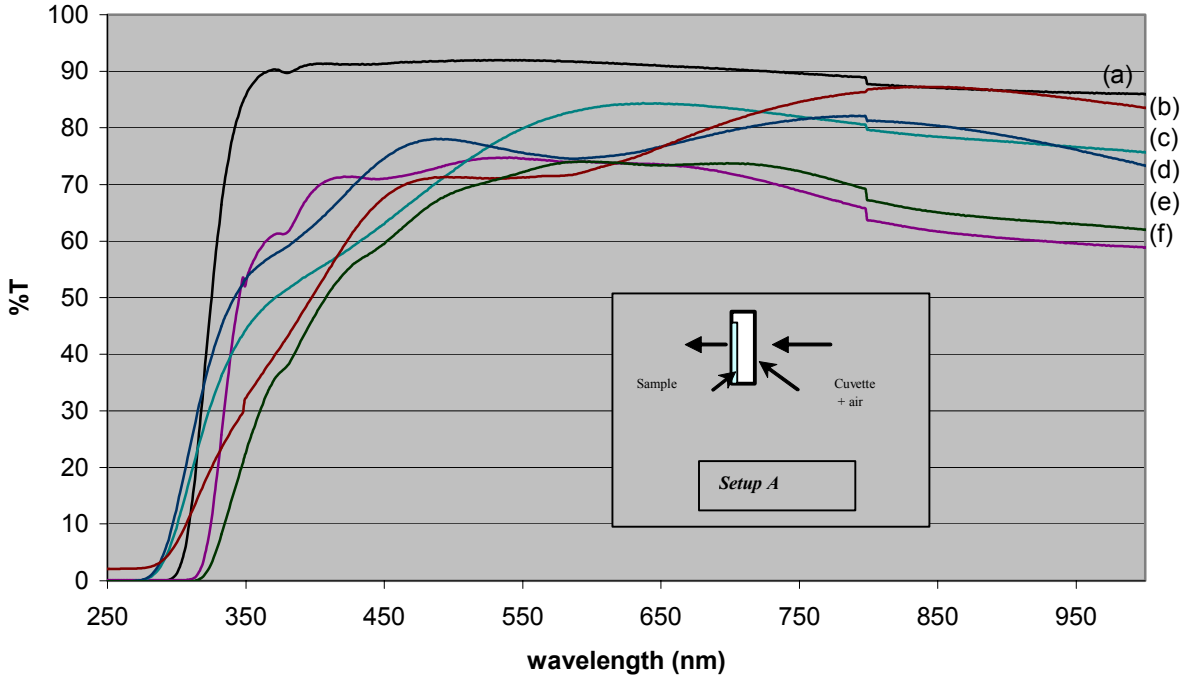

Figure 18: % Transmittance of all samples in setup A. (a) glass, (b), (c), (d) glass/TCCR, (e) TEC15/TCCR, (f) TEC15.

In **Figure 20**, % transmittance spectra of glass/TCCR and TEC15/TCCR are plotted. The TCCR layer was deposited on glass and on TEC15 at the same time. The % transmittance of the glass/TCCR and TEC15/TCCR appear to be higher when the samples are placed in the electrolyte. The TCCR/electrolyte interface allows more light to pass through than the TCCR/air interface. In other words, the electrolyte can be acting as an antireflection layer.

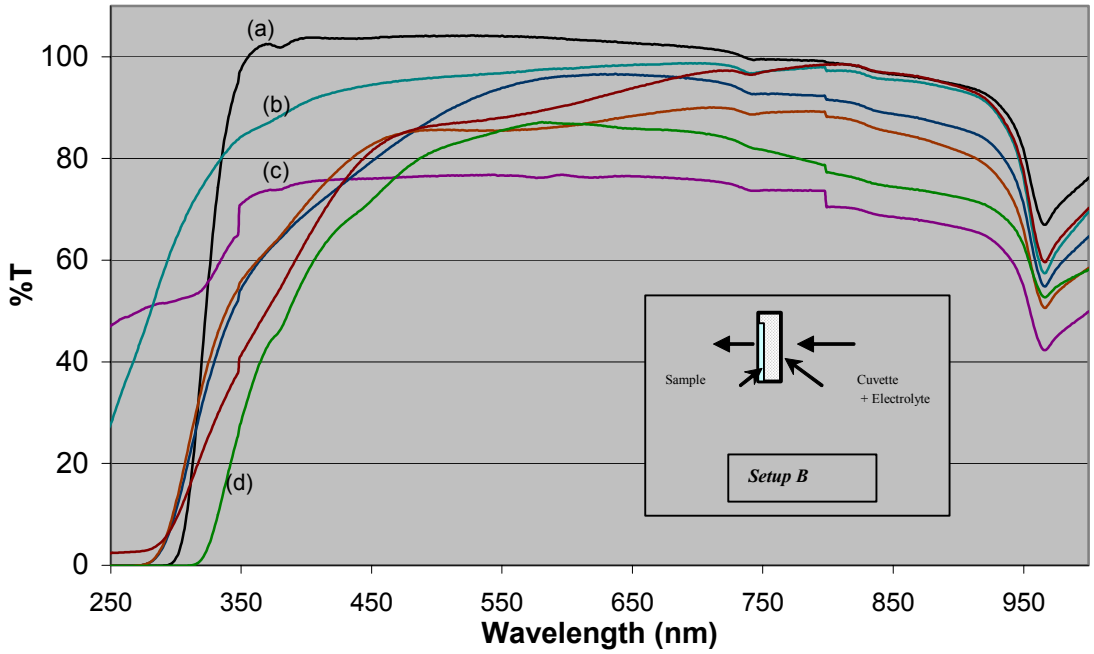

Figure 19: % Transmittance of all samples from setup B. (a) glass, (b) 5.9 M KOH solution, (c) TEC15, (d) TEC15/TCCR, and the rest of spectra are for glass/TCCR.

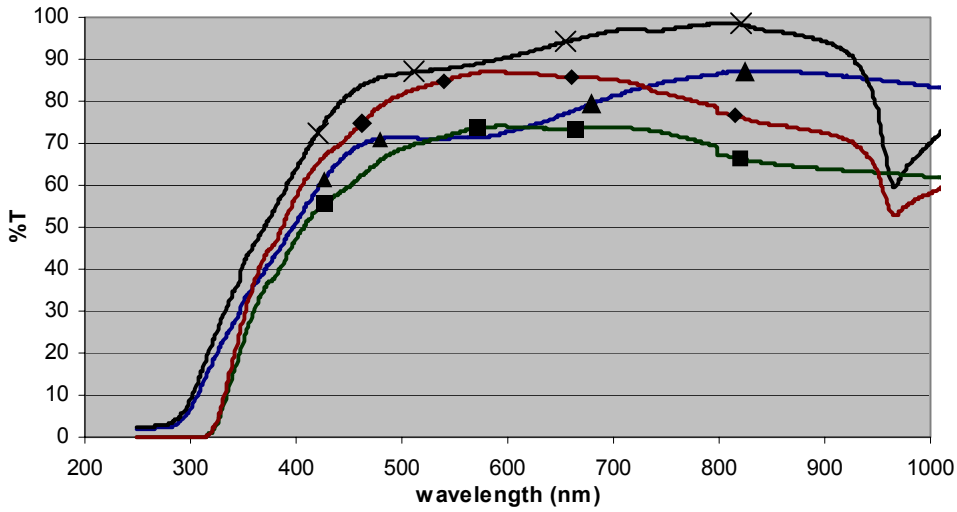

Figure 20: % Transmittance of TCCR deposited on glass and on TEC15; (▲) glass/TCCR, (■) TEC15/TCCR, (X) glass/TCCR studied in electrolyte, and (◆) TEC15/TCCR studied in electrolyte.

The same observation was drawn when comparing other glass/TCCR samples. As shown in **Figure 21**, the % transmittance appears to be higher through the TCCR/electrolyte interface.

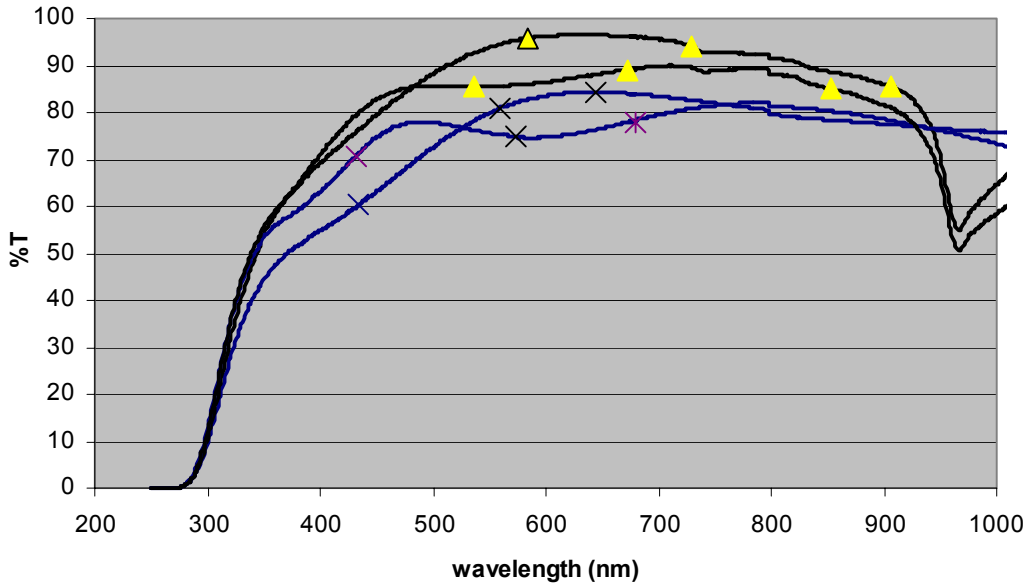

Figure 21: % Transmittance of TCCR layer deposited on glass, (X) glass/TCCR and (▲) glass/TCCR in electrolyte.

In addition, the % transmittance of different glass/TCCR samples appears to be higher at several wavelengths for some samples as shown in **Figure 22**. All samples had a % transmittance above 85% at the TCCR/electrolyte interface. Yet, sample (a) had a higher % transmittance than (b) and (c) between 700 and 850 nm, while sample (b) had a higher % transmittance between 550 and 650 nm than (a) and (c). The TCCR layer can be reproduced to fit with the % transmittance that is needed to better improve the efficiency of the PV-hydrogen system. In this case further studying on the samples is needed to draw a better conclusion.

Moreover, when comparing glass/TCCR layer behavior to that of TEC15, in **Figure 23**, it is evident that the % transmittance of the glass/TCCR is higher than that of

TEC15 where the glass/TCCR layer is less conductive than TEC15 (i.e. a glass/TCCR is better being less conductive in order to allow more light through to the photovoltaic materials.)

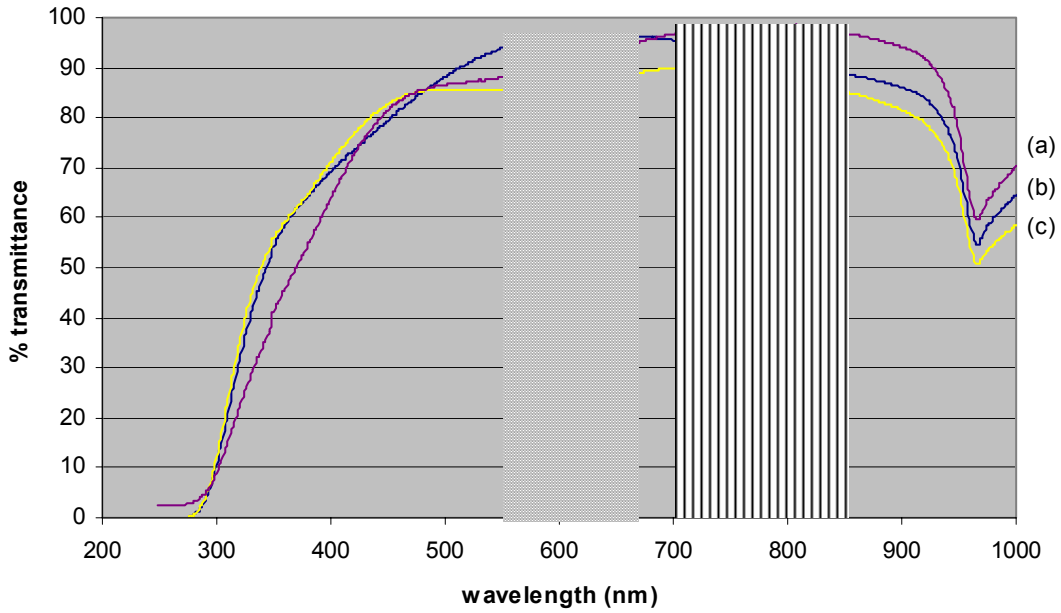

Figure 22: % Transmittance of three glass/TCCR samples.

The TEC15 is more conductive than the TCCR layer used in these samples, and the TCCR layer needed to be conductive in order to serve its purpose in moving the holes from the a-Si device to the surface in order for the electrolysis of water to occur. However, the more conductive the TCCR layer, the less transparent it is, preventing a considerable amount of photons from reaching the a-Si device.

Thus it may be undesirable to use a highly conductive TCCR layer, as what matters is the conductivity of the layer from the a-Si surface to the TCCR surface and not the sheet resistance of the TCCR layer; i.e. a resistive TCCR layer can still serve in

moving the holes to the surface, and be transparent enough to allow more photons to reach the a-Si device.

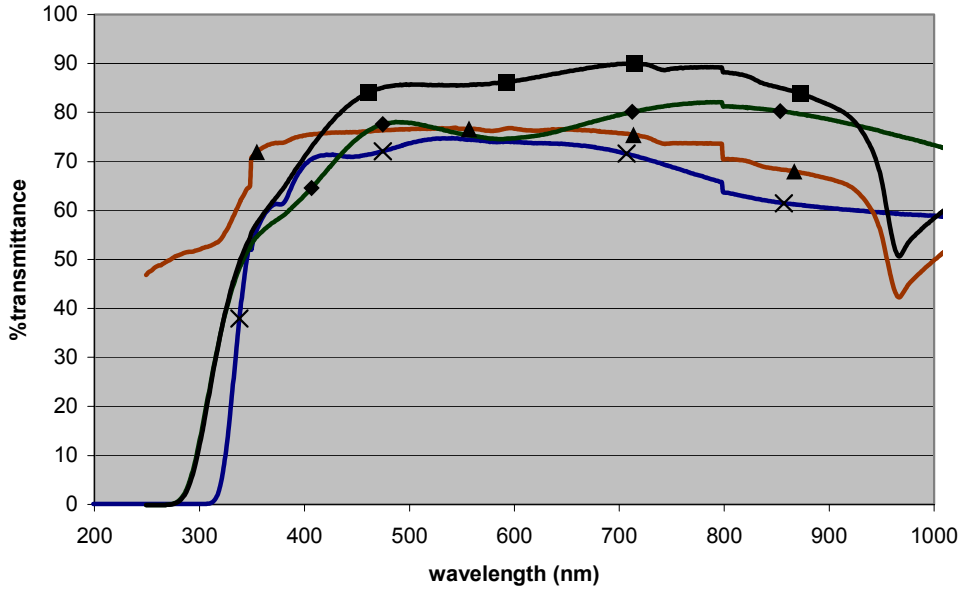

Figure 23: % Transmittance of glass/TCCR and of TEC15; (◆) glass/TCCR, (X) TEC15, (■) glass/TCCR in electrolyte, and (▲) TEC15 in electrolyte.

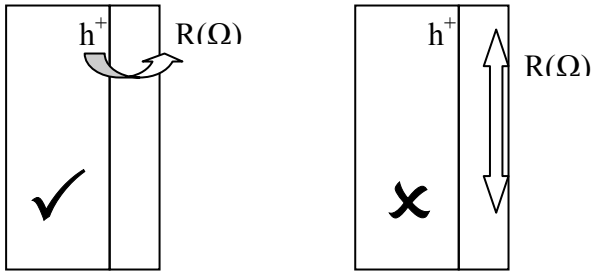

Figure 24. Favorable versus unfavorable hole transfer.

Development of transparent, conductive and corrosion resistant polymer nanocomposite coating to protect triple junction solar cell

The optimum casting condition

It was found that Flexbond-ATO composite films with 30 by percent volume of ATO was stable in KOH solution but the conductivity was not high enough. Therefore, in order to increase conductivity of the Flexbond-ATO film, the concentration of ATO was increased to 40 by percent volume and several films were cast on glass slides by spin coating at different speeds. To seek the optimum casting speed, transmittance and conductivity measurements were carried out on each film. Transmittance measurements were done using a silica detector. To allow for direct comparison of conductivity, two silver paint lines with distance of 2 mm gap between them were coated on each of film and conductivity measurements were performed on the coated films using a digital multimeter. The obtained results are shown in **Table 1**.

Table 1. List of the Flexbond-ATO (40 by percent volume of ATO) films cast by spin coating.

Sample	Speed (rpm)	Time (s)	Resistance (KΩ)	Transmittance (%)
# 1	206	300	91.5	94.7
# 2	250	300	206.2	94.4
# 3	225	300	118	93.9
# 4	170	300	154.4	93.5

Of the four films, film #1 exhibited the lowest resistance with 94.7% transmittance. However, all four films showed similar resistances. Therefore, a spin speed of 206 rpm was the optimum casting speed. Later on, the polymer Flexbond emulsion with ATO by percent volume (V%) concentration of 40 %, 206 rpm was chosen as spin speed to cast films by spin coating.

Stability Test

The ATO-Flexbond composite film with 30 V% ATO showed good stability in KOH on anode side when the applied voltage is ≤ 2.0 V. Therefore, two Flexbond-ATO-40V composite films were cast on commercial ITO glass. One was cast by spin coating at speed of 206 rpm (ATO-Flexond-40V-ITO-Spin), and one by airbrush (ATO-Flexond-40V-ITO-Airbrush). In order to perform stability measurements, these two films were used as anode electrodes and nickel was used as the cathode, and 1.0 N NaOH was used as electrolyte.

Table 2. Stability of the ATO-Flexbond-40V-ITO film cast by spin coating in 1.0 N NaOH on anode side.

Sample	notes	Time	Cumulative Time (min)	Voltage (V)	Current (mA)
ATO-Flexond-40V-ITO-Spin	12/26/2005	10:25 AM	0	1.601	0.4
				1.707	0.48
	day 1			1.807	0.56
				1.904	0.65
	12/26/2005	10:45 AM	20	1.599	0.46
				1.704	0.53
	day 1			1.8	0.6
				1.901	0.67
	12/26/2005	11:15 AM	50	1.6	0.49
				1.705	0.57
	day 1			1.8	0.63
				1.902	0.69
	12/26/2005	11:30 AM	65	1.6	0.46
				1.702	0.54
	day 1			1.799	0.62
				1.901	0.69
	12/26/2005	12:05 AM	100	1.605	0.46
				1.703	0.54
	day 1			1.807	0.61
				1.9	0.67
	12/26/2005	4:45 PM	380	1.605	0.6
				1.7	0.69
	day 1(very small amount of film peeled off)			1.805	0.82
				1.907	1.18
	12/26/2005	5:55 PM	450	1.608	0.43
				1.708	0.54
	day 1			1.8	0.69
				1.902	1.05
	12/27/2005	11:35 AM	90460	1.6	0.56
	day 2			1.702	0.66
				1.803	0.82
				1.905	1.36
	12/29/2005 day 4 multimeter didn't work		the film was still on the ITO just as of two days ago.		
	1/3/2006	12:20pm		1.609	0.33
	day 9			1.7	0.4
				1.803	0.64
				1.905	1.3

As shown in **Table 2**, when the ATO-Flexond-40V-ITO-Spin film was used as anode electrode in 1.0 N NaOH, when electrolysis time was smaller than 380 min, the measured I-V curves at different times were very similar. This means the film was very stable when the electrolysis time was lower than 308 min. When the electrolysis time was greater than 308 min, a very small amount of the film was observed to peel off from the ITO, which resulted in change in the I-V curve. Also, after 9 days of electrolysis, there was little difference between I-V curve measured at 2 and 9 days, and also most of film was observed to be coated on ITO.

Table 3. Stability of the ATO-Flexbond-40V-ITO film cast by airbrush in 1.0 N NaOH on anode side.

Sample	notes	Time	Cumulative Time (min)	Voltage (V)	Current (mA)
ATO-Flexond-40V-ITO-Airbrush	12/21/2005	4:20pm	0	1.609	0.17
				1.703	0.24
	day 1			1.809	0.29
				1.911	0.36
	12/21/2005	4:40pm	20	1.604	0.19
				1.702	0.27
	day 1			1.799	0.29
				1.919	0.37
	12/21/2005	5:10pm	50	1.607	0.19
				1.7	0.24
	day 1			1.801	0.32
				1.901	0.38
	12/22/2005	1:40 PM	75620	1.608	0.62
				1.702	0.7
	day 2			1.799	0.95
	some of film peeled off			1.9	1.71

As shown in **Table 3**, the ATO-Flexond-40V-ITO-Airbrush film showed good stability when the electrolysis time is less than 1 hour. However, when electrolysis time is about 21 hours, some of film was observed to peel off from ITO, which resulted in a relatively large change in the I-V curve.

Introduction

The PV-Hydrogen system consists of a solar cell placed in electrolyte, where a transparent conductive and corrosion resistant layer (TCCR) should be deposited on the solar cell to protect it from corrosion since solar cell is very sensitive to basic electrolyte. Besides being a corrosion resistant layer, the TCCR must be transparent and conductive. Therefore, polymer nanocomposite would be one good candidate TCCR. To obtain a highly transparent and conductive polymer composite films two important factors should be considered: (1) the average diameter of the conductive filler should be much smaller than wavelength of visible light which would minimize scattering at the interface between the filler and polymer matrix, and (2) ultra thin networks of conductive fillers should be formed in the transparent matrix. To meet the first criterion, the nano-sized conductive filler should be used. However, since poor dispersion of conductive nanofiller into polymer matrix tends to result in aggregation of the conductive nanofillers into polymer matrix so that the ultra thin networks fail to be formed in polymer matrix, the polymer composite film would not be transparent even at very low loading and conductive. Therefore, the chosen nano conductive filler should be required to have good compatibility with polymer matrix.

There are two approaches to fabrication of transparent conductive polymer nanocomposite film. One approach is to fabricate transparent conductive polymer thin film from suspension of conductive nano particle (such as $SbSnO_2$, ITO) in polymer emulsion (such as poly (vinyl acetate-acrylic) (PVAc-co-acrylic) copolymer lattices. Since all chemicals used for this approach are very easy to obtain, this experiment was performed initially. Another approach is to synthesize conducting polymer-nanofillers composites using in-situ polymerization, followed by casting transparent and conductive polymer composite film on a solar cell. Since single carbon nanotubes have a high aspect ratio and conductivity, it will be used as nano conductive filler. Polyimide will be used as the polymer matrix. This approach will be done shortly.

Previous Results

Previous studies showed that Flexbond-ATO (40 v %) polymer composite film exhibited reasonable conductivity with high transmittance up to 90 %. Long-term testing was performed on the polymer composite film coated on ITO in 1.0 N KOH electrolyte at the applied voltage of 2.0 V. The results showed that the polymer composite film cast on ITO by spin-coating exhibited much better stability than the film cast on ITO by air-brush. After 9 days of continuous electrolysis, the I-V curve of the composite film coated on ITO by spin-coating had little change. However, as for the composite film coated on ITO by air-brush, when electrolysis time was ~ 21 hours, some of film was observed to peel off from ITO, which resulted in a relatively large change in I-V curve. Therefore, spin-coating might be used as a good technique to cast the composite film.

Current experiments and results

Optimum casting condition to coat the composite film on ITO.

Flexbond-ATO (40 v %) composite film exhibited good conductivity with relatively high transmittance. However, the loading of ATO was relatively high, which made the film fragile. Therefore, in order to increase the mechanical strength of the composite film, the loading of ATO was dropped to 30 v %, which thus would result in decrease in conductivity of the composite film. To fabricate the composite Flexbond-ATO (30 v %) film with good conductivity and transmittance, several spin-casting conditions were used, and the results is shown in **Table 4**. To make better comparison, the results of the composite Flexbond-ATO (20 v %) is also shown in **Table 5**.

Table 4. List of the Flexbond-ATO (30V% ATO)-Carbon Nanofiber (0.01wt %) films cast by spin coating

Sample	Speed (rpm)	Time interval between casting and spin (min)	Resistance (kΩ between 2 mm)	Transmittance (%)
Jan.11-06-1	167	5	30.84	83
Jan.11-06-2	167	1	31.66	90
Jan.11-06-3	167	0	36.1	91
Jan.11-06-4	200	1	70.52	91

Table 5. List of the Flexbond-ATO (20V% ATO)-carbon nanofiber (0.02 wt %) films cast by spin coating

Sample	Speed (rpm)	Time interval between casting and spin (min)	Resistance (MΩ between 2 mm)	Transmittance (%)
Feb.08-1	167	1		
Feb.08-2	135	1	0.6	
Feb.08-3	100	1	0.33	
Feb.08-4	172	1	0.44	

In comparison, Flexbond–ATO (30 V %) composite film exhibited much higher conductivity than the Flexbond-ATO (20 V %) composite film. As for the Flexbond-ATO (30 v %) composite films, as shown in **Table 4**, the spin-casting condition had large effect on the conductivity and transmittance of the composite film. Higher spin speed would result in lower conductivity but higher transmittance. Also at the same spin speed, the time interval between casting and spin is a key factor to the conductivity and transmittance, i.e. longer time, which allowed the casting solution to contact the ITO surface longer, led to the higher conductivity but lower transmittance. As shown in **Table 4**, spin-speed of 167 rpm and 1 min of time interval are the optimum spin-casting conditions for the Flexbond-ATO (30 V %) composite films.

Silane treatment method

Specifically, the adhesion between polymer and inorganic material is very poor. Therefore, in order to improve the adhesion between the Flexbond-ATO (30 v %) and solar cell (ITO is on the top of solar cell), the solar cell was treated with silane coupling

agent. In this project, three types of silane coupling agents, i.e., 3-aminopropyl-trimethoxysilane (silane-NH_2), 3-glycidoxypropyl-trimethoxysilane (silane-epoxy), and 3-(trimethoxysil)propylmethacrylate (silane-vinyl), were used. The chemistry for the treatment is shown in **Figure 25**.

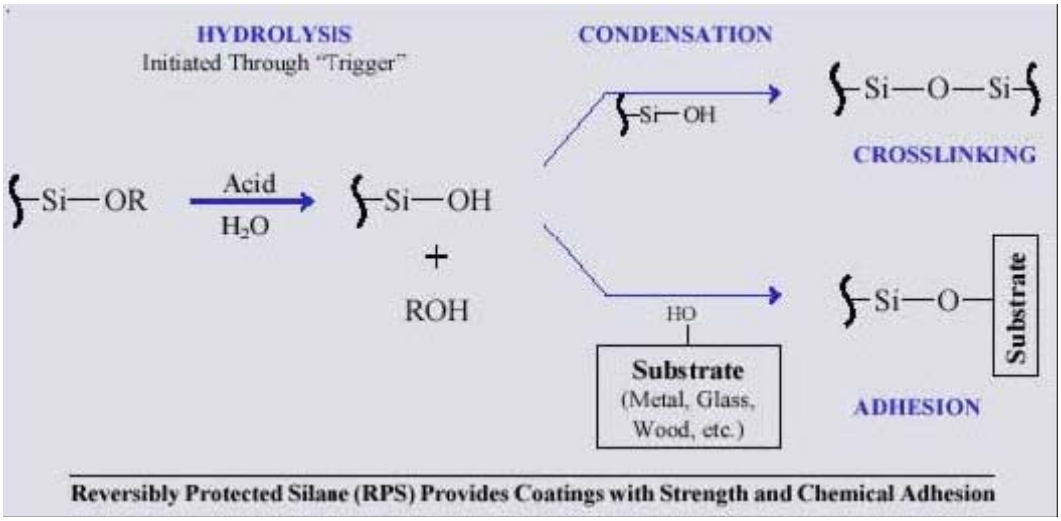

Figure 25. Schematic of silane treatment.

Preparation of silane treatment solution:

A couple of drops of acetic acid was added into 250 mL of deionized water and stirred completely for 10 min. 1 mL of silane coupling agent was added drop-wise to the mixture and stirred for 30 min.

Silane Treatment:

Before being treated with silane coupling agent, the solar cell was washed with deionized water completely and dried at 80 °C for one hour. The dried solar cell was

placed into the as-prepared silane solution and kept for 2 hours, and dried at 80 °C overnight. The treated solar cell was cut into four pieces for chemical resistance test in different concentration of KOH, and the results are shown in **Table 6**.

Table 6. Chemical resistance of the treated solar cell in KOH

	1N KOH	2 N KOH	3 N KOH	4 N KOH
Observation	Very few bubbles 1 h after being immersed	Very few bubbles 1h after being immersed	A lot of bubbles 1h after being immersed	A lot of bubbles 1h after being immersed

As shown in **Table 5**, the treated solar cell was relatively stable in 1 N or 2 N KOH solutions. As a result, only 1 N and 2 N KOH solutions were used to do H_2 generation experiments.

Gas generation experiment

The objective of this project is to develop the transparent, conductive, and corrosion-resistant coating to protect triple junction solar cell. In this project, the triple junction solar cell was treated first using 3-aminopropyl-trimethoxysilane coupling agent as described above, and coated with Flexbond-ATO (30 v %) composite film as described in below. Finally the solar cells were coated with Flexbond-ATO (30 v %) were placed in two separate beakers which contain 1 N and 2 N KOH solutions, respectively, followed by removing the two beakers under halogen light to observe gas generation of the solar cells. For the two coated solar cells, 3 min after they were in KOH electrolytes,

small bubbles started being generated only around the good ITO contacts. The coating of Flexbond-ATO (30 V %) composite film resulted in 8 ~ 20 % decrease in the voltage. **Figure 2** shows gas generation of one of the coated solar cells in 1 N KOH. However, the film started peeling off after the electrolysis had been running for 2 hours in 1 N KOH and 1 hour in 2 N KOH, which means the adhesion between polymer film and ITO is poor.

Figure 26. Gas generation of the triple junction solar cell coated with Flexbond-ATO (30 v %) composite film under a halogen light.

Improvement of the adhesion between polymer film and solar cell

The adhesion between the polymer film and the solar cell is poor. In order to enhance the adhesion between polymer film and solar cell, the condition of the silane treatment should be adjusted. The mixture of 3.5 mL of silane coupling agent, 0.2 mL of acetic acid and 60 mL of deionized water was added into a 100 mL of beaker and stirred for 1 hour. The solar cell was washed with deionized water completely and dried at 80 °C for 3 hours. The washed solar cell was placed into the as-prepared silane solution and kept for 24 hours. The treated solar cell was coated with Flexbond-ATO (30 V %) just as described in section above and dried at 80 °C overnight. Three coated solar cells, which were silane treated with three different kinds of silane coupling agents

(silane-NH_2, silane-epoxy, and silane-vinyl), were placed into 2 N KOH solutions, respectively. Any of the three solar cells exhibited much better stability in 2 N KOH than the coated solar cell which was silane treated as described previously. However, after being immersed in 2 N KOH for 5 days, most of the coated solar cell treated with silane-epoxy degraded, but no degradation was observed for either coated solar cell treated with silane-NH_2 or silane-vinyl. Therefore, both silane-NH_2 and silane-vinyl treatments which are described here would be good methods to improve the adhesion between polymer and solar cell.

Single carbon nanotube film

Purification of single carbon nanotube:

Single wall carbon nanotubes are added into polymer nanocomposite to enhance its conductivity. 0.2 g of single wall carbon nanotube was added into the mixture of 50 mL of deionized water and 10 mL of concentrate nitric acid, and sonicated for 1 hour. The suspension was refluxed for 48 hours, and filtered by centrifuge. The solid was washed with excess of deionized water and filtered by centrifuge until the solution became neutral. The as-obtained solid was dried at 120 °C under vacuum for 24 hours. The purified single wall carbon nanotube will be used in the future to synthesize polyimide-single carbon nanotube composite or fabricate very thin single carbon nanotube films on solar cells.

As reported in last report, both silane-NH_2 and silane-vinyl treatments under the appropriate condition improved the adhesion between polymer nanocomposite and solar cell so that no degradation of polymer nanocomposite coating was observed after the solar coated with polymer nanocomposite Flexbond-ATO had been immersed in 2 N KOH for 5 days at room temperature. However, the polymer nanocomposite film was still observed to peel off from the solar cell that was treated with either silane-NH_2 or silane-vinyl first and coated with Flexbond-ATO polymer nanocomposite after the coated solar cell had been immersed in 2N KOH to generate gases under halogen light for about 3 hours. This might be because polymer nanocomposite film has larger thermal expansion coefficient than the solar cell. Under halogen light, the temperature of the electrolyte is relatively higher than room temperature so that polymer nanocomposite film tended to expand much more than the solar cell in 2 N KOH electrolyte, which resulted in peeling-off of the Flexbond-ATO film. Therefore, in order to minimize the difference in the thermal expansion coefficient between coating and solar cell, the following two approaches might be used and will be carried out in the future:

(1) One approach is to add negative thermal expansion (NTP) nanomaterial into the Flexbond-ATO mixture to fabricate the Flexbond-ATO-NTP composite coating, which involves selection of NTP, modification of NTP to improve its dispersion in the Flexbond-ATO, and fabrication of the Flexbond-ATO-NTP composite film. The resulting Flexbond-ATO-NTP composite film would have smaller thermal expansion coefficient in KOH electrolyte under halogen light

than the Flexbond-ATO composite film since NTP material tends to contract when the temperature of electrolyte increases.

(2) One approach is to choose the ceramic conducting as coating. Single nanotube thin film would be one of candidates.

Additionally, we can fabricate a free-standing conducting polymer nanocomposite film, which can be directly used to wrap the solar cell. Polyimide-single carbon nanotube composites of very low loading would be potential candidate, and will be the focus of the later research.

Task 4: Hydrogen production from bio-derived materials using Aqueous Phase Reforming (APR).

Production of hydrogen from biomass for its use in fuel cells for transportation and stationary applications.

Tasks

Following is the list of tasks conducted in order to accomplish the above target.

4.1. Choice of appropriate method for biomass conversion to hydrogen

4.2. Demonstrate the feasibility of proposed process

4.3. Optimization of the process parameters in order to enhance the hydrogen productivity

Task 4.1: Choice of appropriate method for biomass conversion to hydrogen.

The conversion of biomass to hydrogen is difficult due to its very unstable nature to the thermal treatment. Conventionally, steam and autothermal reforming processes were studied to obtain hydrogen from biomass. In earlier stages of this project, we have followed the same conventional approach. We used glucose as biomass surrogate and tried steam and autothermal reforming processes. However, glucose was very unstable in nature and produced significant amount of char and tar. Although we have seen hydrogen yields in the range of 50-60 %, the process was not feasible due to the problems of char and tar formation.

In order to avoid these problems, we have proposed an integrated process for conversion of biomass to hydrogen. In this process, complex biomass is first converted to relatively simple molecules in the biological process (fermentation process) followed by the reforming of the fermentation broth to obtain hydrogen. We have chosen Aqueous Phase Reforming (APR) as an alternative to steam and autothermal reforming. This is low temperature process (~ 250 °C) and moderate pressure (~ 600 psig). The advantage of this process is that the final product hydrogen is obtained at higher pressure which can be easily used in fuel cells without additional compressors. Also since the reforming temperature is low, water gas shift reaction is favored at this temperature. Therefore, CO concentration in the product gases is very low (in ppm range) as opposed to 5-10 % observed in steam and autothermal reforming. One more advantage of the APR is that it is a liquid phase process. Therefore, there is saving in energy required for the evaporation of excess water.

Task 4.2: Demonstrate the feasibility of proposed process.

In order to demonstrate the proposed integrated method of hydrogen production, we have built a high pressure, high temperature reactor system with detailed instrumentation, process control, and HAZOP analysis. Glucose was used as a biomass surrogate in all the experiment. Glucose was first converted to ethanol and other oxygenated hydrocarbons present in small amounts as fermentation byproducts. The fermentation experiments were conducted using *Saccharomyces cerevisiae.* The fermentation was done at 30 °C for 24 h. At the end of the fermentation the broth was

centrifuged at 2000 rpm for 20 min to remove the cell biomass. Then this fermentation broth was used in the aqueous phase reformer. **Figure 1** shows the performance of the 5 %Pt/Al_2O_3 catalyst at 250 °C and 600 psig. The concentration of the ethanol in fermentation broth was found to be close to 5 %. When experiments were carried out using a simulated mixture containing 5 % ethanol (200 proof) mixed with DI water, the catalyst performance was stable. However, when the feed was switched to the actual fermentation broth, there was rapid catalyst deactivation and hydrogen yield dropped to almost zero.

However, it was important to understand the causes of the catalyst deactivation for the successful integration of these two processes. We proposed that the catalyst deactivation is due to sulfur or phosphorous impurities found in cell culture or the biomass itself. We have conducted the experiments using cysteine as the S surrogate and disodium adenosine triphosphate as the P surrogate. We analyzed the fermentation broth and found that S and P were present in the range of 10 and 13 ppm respectively. However, when we conducted the experiment by adding S and P surrogate in 5 % ethanol (200 proof) - DI water solution, it was observed that P does not cause any catalyst deactivation. However, the catalyst was found to deactivate when there was S present in the feed. The results of these experiments are summarized in **Figure 2**. The rate at which catalyst deactivated in the case of the fermentation broth was similar to rate of the catalyst deactivation when it is exposed to 10 ppm S in the form of cysteine in 5 % ethanol solution. Therefore, it was concluded that the catalyst deactivation observed in the case of fermentation broth was due to S impurities. In order to eliminate these impurities and produce hydrogen form fermentation broth at stable rate, we tried

nanofiltration process. Once the fermentation process was complete, we tried to further clean the fermentation broth using nanofiltration membrane and found that the hydrogen productivity was stable.

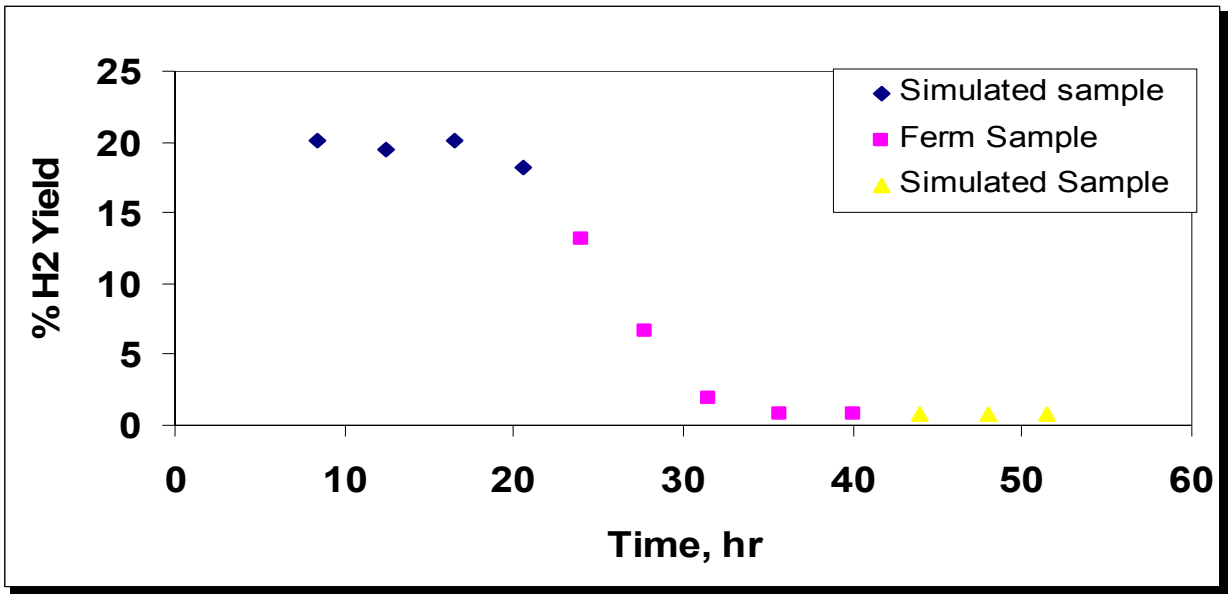

Figure 14. The stability of the catalyst in the case of fermentation sample and simulated sample under the APR conditions.

Task 4.3: Optimization of the process parameters in order to enhance the hydrogen productivity

The productivity of the hydrogen was dependent on different process parameters including temperature, pressure, type of catalyst used, residence time, and concentration of the reactant. The catalysts used in the earlier stages of the project were supported on the alumina powder. However, the post run analysis of the catalyst samples revealed the phase transition of the alumina to the new phase (boehmite). This transition of phase was possible since alumina was present in contact with hot water at high pressure. This phase transition resulted in the significant loss of the total surface

area. Therefore, it was important to find the alternative catalyst supports which were stable under APR environment without compromising the catalyst activity towards the hydrogen production.

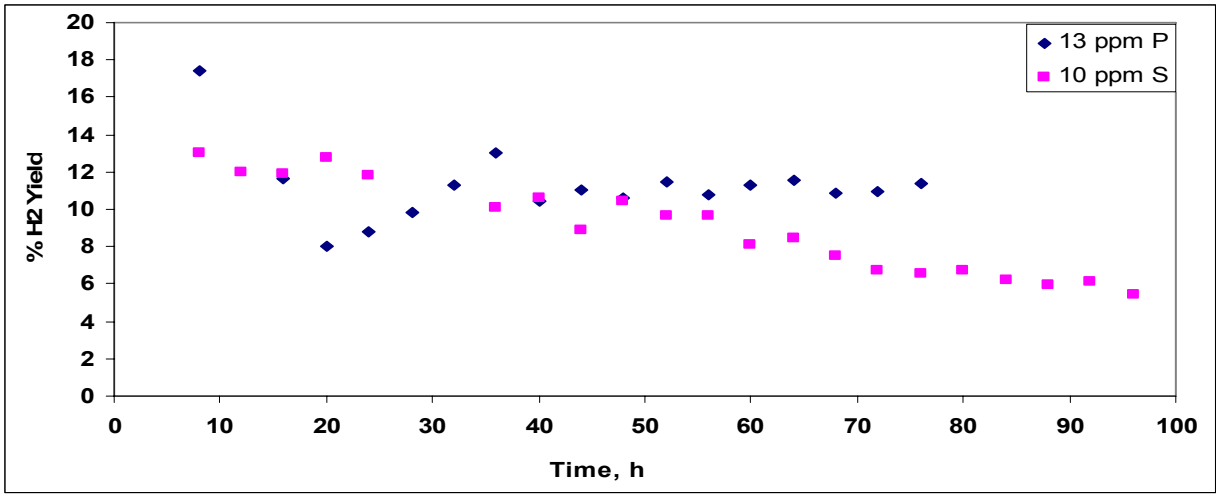

Figure 15. The performance of the Pt-Co catalyst supported on activated carbon when exposed to different impurities.

We have tested various combinations of active metals and the support. All these tests were performed using 5 % ethanol - DI water solution. The results of these experiments are summarized in **Figure 3**. The activity of the catalyst was measured in terms of the hydrogen yield which was defined as moles of hydrogen produced per mole of ethanol relative to the maximum theoretical possible based on the stiochiometry of the following reforming reaction,

$$C_2H_5OH + 3\,H_2O \longrightarrow 2CO_2 + 6\,H_2 \qquad (1)$$

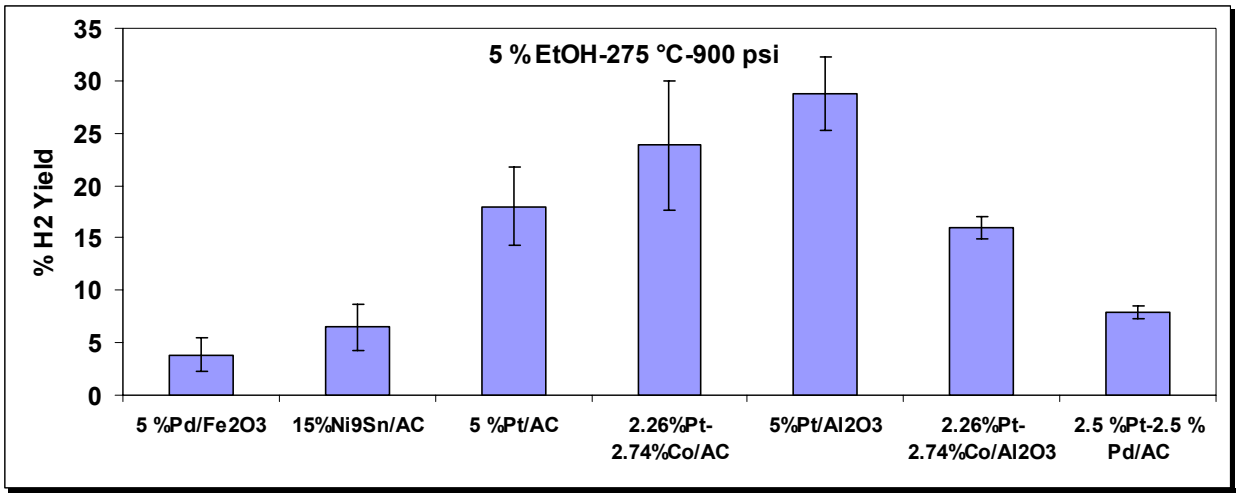

Figure 16. Activity of the different catalysts for hydrogen production in APR of ethanol.

It was observed that the Pt supported on the Al_2O_3 has the highest activity for the hydrogen production However, the support was found to be unstable under the reforming condition. Therefore, Pt supported on activated carbon was tested as an alternative catalyst. However, the performance of the Pt supported on activated carbon was found to be almost half of the Pt supported on alumina. Addition of Co was found to enhance the performance of the catalyst. 2.26 % Pt-2.74 % Co supported on activated carbon was found to perform better than the 5 % Pt supported on the activated carbon. Therefore, Pt-Co combination supported on the activated carbon was used for the APR of the fermentation broth due to its stability and comparable activity.

Conclusions:

We have successfully demonstrated the feasibility of the integrated biological and thermo chemical process. APR reforming was found to have many advantages over the conventional steam and autothermal reforming. Since the reforming temperature is low,

we need highly active noble metal catalyst to obtain hydrogen in APR. However, the catalytic activity can be enhanced by adding different active metals and substantially reducing the cost associated with the expensive noble metals. The catalyst stability is very important for the continuous production of hydrogen. However, impurities in the form of sulfur coming form cell culture and biomass itself, tend to cause catalyst deactivation. We have proposed and demonstrated the use of nanofiltration process to eliminate these impurities from fermentation broth that will produce the hydrogen at constant rate without deactivation.

Publications:

- Swami, S. M.; Vaibhav C.; Kim Dong-Shik; Sim S. J.; Abraham, M. A., Production of Hydrogen from Glucose as Biomass Simulant: Integrated Biological and Thermochemical Approach, ***Ind. & Eng. Chem. Res.*** (In Press).
- Swami, S. M.; Ayyappan, P.; Abraham, M. A. Preprints of symposia-American Chemical Society, ***Division of Fuel Chemistry***, 2007, 52 (2), 360-361.
- Swami, S. M.; Abraham, M. A., Integrated Catalytic Process for Conversion of Biomass to Hydrogen, ***Energy & Fuels***, 2006, 2616-2622.
- Ingler Jr., W.B.; Sporar, D.; Deng, X. "Sputter Deposition of In-Fe_2O_3 Films for Photoelectrochemical Hydrogen Production" *ECS Trans.* Vol. 3 (State-of-the-Art Program on Compound Semiconductors 45 (SOTAPOCS 45) -and- Wide Bandgap Semiconductor Materials and Devices 7), **2006**, 253.
- Ingler Jr., W.B.; Attygalle, D.; Deng, X. "Properties of Rf Magnetron Sputter Deposited Cobalt Oxide Thin Films as Anode for Hydrogen Generation by Electrochemical Water Splitting" *ECS Trans.* Vol. 3 (State-of-the-Art Program on Compound Semiconductors 45 (SOTAPOCS 45) -and- Wide Bandgap Semiconductor Materials and Devices 7), **2006**, 261.

Presentations:

- Liwei Xu, "Development of Improved Materials for Integrated Photovoltaic-Electrolysis Hydrogen Generation Systems", presentation at "Hydrogen Program Review", Bergamo Center, Dayton, OH, February 8, 2006.
- X .Deng, Presentation, at National Hydrogen Finance Forum, Long Beach Convention Center, Long Beach, California. March 16, 2006
- X. Deng, "Nano Materials in Photovoltaics", Presentation and Panel Discussion in "Nanotechnolgoy in Energy: Impact on Business, Technology and Research", a panel discussion in 2006 Ohio NanoSummit, Greater Columbus Convention Center, Columbus, OH, April 4-5, 2006.
- X. Yang, W. Du, X. Cao, C. Das, and X. Deng, "Solar Cell Back Reflector with Nanoscale Roughness for Light Trapping", presentation at 2006 Ohio NanoSummit, Greater Columbus Convention Center, Columbus, OH, April 4-5, 2006.
- Wenhui Du, Xianbo Liao, Xiesen Yang, Xianbi Xiang, Xunming Deng, Kai Sun, "Nanostructure in the p-layer and its impacts on amorphous silicon solar cells", presentation at 2006 Ohio NanoSummit, Greater Columbus Convention Center, Columbus, OH, April 4-5, 2006.
- Xinmin Cao, Wenhui Du, Xunming Deng, "Fabrication and Optimization of Amorphous Silicon Based Triple-junction Solar Cell with Nanocrystalline Silicon Bottom Cell", presentation at 2006 Ohio NanoSummit, Greater Columbus Convention Center, Columbus, OH, April 4-5, 2006.
- Xinmin Cao and Xunming Deng, Fabrication and Optimization of nc-Si:H, a-Si:H and a-SiGe:H n-i-p solar cells using VHF PECVD at High Deposition Rates", presentation at NREL Amorphous Silicon Team Meeting, San Francisco Marriott, San Francisco, CA, April 17, 2006.
- Wenhui Du and Xunming Deng, "High-Rate VHF PECVD Fabrication of a-SiGe:H Bottom Cells Using SiH4", presentation at NREL Amorphous Silicon Team Meeting, San Francisco Marriott, San Francisco, CA, April 17, 2006.

- Yasuaki Ishikawa and Xunming Deng, “DC bias voltage effect on nc-Si:H film deposition and its solar cells”, presentation at NREL Amorphous Silicon Team Meeting, San Francisco Marriott, San Francisco, CA, April 17, 2006.
- Xunming Deng, Xinmin Cao, Yasuaki Ishikawa, Wenhui Du, Xiesen Yang, Chandan Das, Aarohi Vijh, “Fabrication and Characterization of Triple-junction Amorphous Silicon Based Solar Cell with Nanocrystalline Silicon Bottom Cell”, presentation at 2006 IEEE 4th World Conference on Photovoltaic Energy Conversion, Hilton Waikoloa Village, Waikoloa, Hawaii, May 7-12, 2006.
- Xinmin Cao, Wenhui Du, Xiesen Yang, Xunming Deng, “ Fabrication of nc-Si:H n-i-p single-junction solar cells using VHF PECVD at a deposition rate of 10 Å/s”, presentation at 2006 IEEE 4th World Conference on Photovoltaic Energy Conversion, Hilton Waikoloa Village, Waikoloa, Hawaii, May 7-12, 2006.
- Yasuaki Ishikawa, Xinmin Cao, Wenhui Du, Chandan Das, Xunming Deng, “DC Bias Effect on Nanocrystalline Silicon Solar Cells Deposited under a High Power High Pressure Regime”, presentation at 2006 IEEE 4th World Conference on Photovoltaic Energy Conversion, Hilton Waikoloa Village, Waikoloa, Hawaii, May 7-12, 2006.
- Chandan Das, Xinmin Cao, Wenhui Du, Xiesen Yang, Yasuaki Ishikawa, Xunming Deng, “Effects of hydrogen dilution grading in active layer on performance of nanocrystalline single junction bottom component and corresponding a-Si:H based triple junction solar cells”, presentation at 2006 IEEE 4th World Conference on Photovoltaic Energy Conversion, Hilton Waikoloa Village, Waikoloa, Hawaii, May 7-12, 2006.
- Deepak Sainju, P. J. van den Oever, N. J. Podraza1, Jie Chen, J. A. Stoke, Xiesen Yang, Maarij Syed, R. W. Collins, Xunming Deng, “Origin of Optical Losses in Ag/Zno Back-Reflectors for Thin Film Si Photovoltaics”, presentation at 2006 IEEE 4th World Conference on Photovoltaic Energy Conversion, Hilton Waikoloa Village, Waikoloa, Hawaii, May 7-12, 2006.
- Liwei Xu, “Critical Research for Cost-effective Photoelectrochemical Production of Hydrogen”, presentation at DOE Hydrogen Program 2006 Annual Merit Review, Arlington, VA, May 16-19, 2006.
- Xunming Deng, “Production of Hydrogen for Clean and Renewable Sources of Energy for Fuel Cell Vehicles”, presentation at DOE Hydrogen Program 2006 Annual Merit Review, Arlington, VA, May 16-19, 2006.
- William Ingler, Jr., “Critical Research for Cost-effective Photoelectrochemical Production of Hydrogen”, presentation at DOE Photoelectrochemical Working Group Meeting, Lee Suite, Crystal Gateway Marriott, Arlington VA, May 18, 2006.
- William Ingler, Jr., “Production of Hydrogen for Clean and Renewable Sources of Energy for Fuel Cell Vehicles”, presentation at DOE Photoelectrochemical Working Group Meeting, Lee Suite, Crystal Gateway Marriott, Arlington VA, May 18, 2006.
- X. Deng, “Lightweight and Flexible a-Si Based Solar Cells”, Advanced Solar Energy Solutions for the Warfighter Workshop, Panama City, FL, May 18-19, 2006.
- Poster, Hunley, D.P.; Ingler, W.B.; Price, K.; Deng, X. “Sputter Deposition on Indium-doped Iron Oxide Films for Photoelectrochemical Hydrogen Production” *5th Annual Posters-at-the-Capitol*, Frankfort, KY, February 2, 2006.
- Ingler Jr., W.B., Attygalle, D., Deng, X. “Properties of Rf Magnetron Sputter Deposited Cobalt Oxide Thin Films as Anode for Hydrogen Generation by

Electrochemical Water Splitting" Abstracts of Papers, *210th Meeting of the Electrochemical Society*, *Inc.*, Cancun, MX, October 29-November 3, **2006**. (Poster)

- Ingler Jr., W.B., Sporar, D., Deng, X. "Sputter Deposition of In-Fe_2O_3 Films for Photoelectrochemical Hydrogen Production" Abstracts of Papers, *210th Meeting of the Electrochemical Society*, *Inc.*, Cancun, MX, October 29-November 3, **2006**. (Poster)
- Swami, S. M.; Abraham, M. A. "Investigation of catalyst deactivation mechanism for hydrogen production from fermentation broth", **2007 AIChE Annual Meeting,** Salt Lake City, UT, Nov, 4-9, 2007
- Swami, S. M; Ayyappan, P.; Abraham, M. A. "Production of hydrogen from biomass: Integrated biological and thermo-chemical approach", **ACS 234th national meeting and Exposition,** Boston, MA, Aug, 19-23, 2007
- Swami, S. M.; Ayyappan, P.; Abraham, M. A. "An integrated approach for production of hydrogen from biomass", **3rd International Conference on Green and Sustainable Chemistry, Delft, The Netherlands**, July, 1-5, 2007
- Swami, S. M.; Abraham, M. A. "Production of hydrogen from biomass: Integrated biological and thermo-chemical approach", **North American Catalysis Society, 20th North American Meeting,** Houston, TX, June, 17-22, 2007
- Swami, S. M.; Abraham, M. A. "Aqueous phase reforming of bio-derived organic compounds", **AIChE 2006 Annual Meeting**, San Francisco, CA, Nov., 2006
- Swami, S. M.; Abraham, M. A. "An Integrated catalytic process for conversion of biomass to hydrogen", **AIChE Annual Meeting**, Cincinnati, OH, Nov., 2005
- Swami, S. M.; Abraham, M. A. "Hydrogen production from biomass", 19th North American Catalysis Society Meeting, Philadelphia, PA, May 24, 2005.

Patents:

March 9, 2006
Japan Domestic Announcement
Title of Patent: Integrated Photoelectrochemical Cell and System having a Liquid Electrolyte
Inventors: Xunming Deng and Liwei Xu
Ser. No. PCT2004/557269 filed November 24, 2003
Japan Patent Application. No. 2004-557269
Japan Domestic Announcement [Kohyo] No: 2006-508253
Japan Domestic Announcement Date: March 9, 2006

April 10, 2006
PCT Patent Application
Title of Patent: Integrated Photovoltaic-electrolysis cell
Inventors: Malabala Adiga, Xunming Deng, Aarohi Vijh, and Liwei Xu
Filing No: PCT/2006/013222
Corresp. to Ser. No. 60/670,177 filed April 11, 2005.

May 16, 2006
The following PCT patent application has entered into National Phase.
Country selected: US
Title of Patent: Interconnected Photoelectrochemical Cells
PCT No. US2005/005121
Priority based on US Ser. No. 60/545,892
Inventors: X. Deng and L. Xu

Task Schedule

Task Number	Project Milestones	Task Completion Date				Progress Notes
		Original Planned	Revised Planned	Actual	Percent Complete	
1	Integrated PV-H_2-Fuel-Cell Facility	6/2007	1/2008	1/2008	100%	On-Track.
2	Adv'd Materials for Substrate type PEC	6/2007	1/2008	1/2008	100%	On-Track.
3	Adv'd Materials for Immersion-Type PEC	6/2007	1/2008	1/2008	100%	On-Track.
4	H_2 Production Biomass-Wastes	6/2007	1/2008	1/2008	100%	On-Track.

Quarter	From	To	Estimated Federal Share of Outlays*	Actual Federal Share of Outlays	Estimated Recipient Share of Outlays*	Actual Recipient Share of Outlays	Cumulative
	Start	5/1/05	Note 1				
2Q05	5/1/05	6/30/05		0		0	0
3Q05	7/31/05	9/30/05		500		0	500
4Q05	10/1/05	12/31/05		38,076		0	38,576
1Q06	1/1/06	3/31/06		35,014		140,449	214,038
2Q06	4/1/06	6/30/06		102,451		62,470	378,959
3Q06	7/31/06	9/30/06		150,773		61,357	591,089
4Q06	10/1/06	12/31/06		122,460		1,550	715,100
1Q07	1/1/07	3/31/07		208,575		92,594	1,016,269
2Q07	4/1/07	6/30/07		142,810		57,928	1,217,007
3Q07	7/1/07	9/30/07		138,984		40,262	1,396,253
4Q07	10/1/07	12/31/07		52,357		(119,059)	1,330,551
Totals			0	992,000	0	337,551	1,329,551